Title
Processing of Silver-Implanted Aluminum Nitride for Energy Harvesting Devices

Permalink
https://escholarship.org/uc/item/7x49964m

Author
Alleyne, Fatima

Publication Date
2013

Peer reviewed|Thesis/dissertation

Processing of Silver-Implanted Aluminum Nitride for Energy Harvesting Devices

By

Fatima Sierre Alleyne

A dissertation submitted in partial satisfaction of the
requirements for the degree of
Doctor of Philosophy
in
Engineering – Materials Science and Engineering
in the
Graduate Division
of the
University of California, Berkeley

Committee in Charge:
Professor Ronald Gronsky, Chair
Professor Oscar Dubon
Professor Alice Agogino

Spring 2013

Processing of Silver-Implanted Aluminum Nitride for Energy Harvesting Devices

By

Fatima Sierre Alleyne

Abstract

Processing of Silver-Implanted Aluminum Nitride for Energy Harvesting Devices

by

Fatima Sierre Alleyne

Doctor of Philosophy in Engineering – Materials Science and Engineering

University of California, Berkeley

Professor Ronald Gronsky, Chair

One of the more attractive sources of green energy has roots in the popular recycling theme of other green technologies, now known by the term "energy scavenging." In its most promising conformation, energy scavenging converts cyclic mechanical vibrations in the environment or random mechanical pressure pulses, caused by sources ranging from operating machinery to human footfalls, into electrical energy via piezoelectric transducers. While commercial piezoelectrics have evolved to favor lead zirconate titanate (PZT) for its combination of superior properties, the presence of lead in these ceramic compounds raises resistance to their application in anything "green" due to potential health implications during their manufacturing, recycling, or in-service application, if leaching occurs. Therefore in this study we have pursued the application of aluminum nitride (AlN) as a non-toxic alternative to PZT, seeking processing pathways to augment the modest piezoelectric performance of AlN and exploit its compatibility with complementary-metal-oxide semiconductor (CMOS) manufacturing.

Such piezoelectric transducers have been categorized as microelectromechanical systems (MEMS), which despite more than a decade of research in this field, is plagued by delamination at the electrode/piezoelectric interface. Consequently the electric field essential to generate and sustain the piezoelectric response of these devices is lost, resulting in device failure. Working on the hypothesis that buried conducting layers can both mitigate the delamination problem and generate sufficient electric field to engage the operation of resonator devices, we have undertaken a study of silver ion implantation to experimentally assess its feasibility. As with most ion implantation procedures employed in semiconductor fabrication, the implanted sample is subjected to a thermal treatment, encouraging diffusion-assisted precipitation of the implanted species at high enough concentrations. The objective of this study is to understand the resulting phase transformation behavior during Ag precipitation with the intent to ultimately control the electrical operation of AlN piezoelectric resonators in energy scavenging applications.

In this work, multiple source reactive ion sputtering was employed to deposit a thin film of AlN on a 525 μm thick Si substrate, followed by ion implantation (Ag cathode) into the aluminum nitride, and subsequent thermal annealing. Computer simulations were conducted to

elucidate the projected range of the silver in the AlN epilayer as a result of the ion implantation process. A myriad of characterization methods including Rutherford Backscattering Spectrometry (RBS), x-ray diffraction (XRD), rocking curve, electron microscopy was employed to quantify the concentration of silver, morphology of silver precipitates, as well as the composition, crystallinity and degree of damage in the ion-implanted AlN samples with respect to thermal annealing conditions. The presence, or lack of precipitates in the samples was utilized to draw conclusions about the feasibility of developing a buried conductive layer in a ceramic matrix *via* ion implantation.

Computer simulations results obtained *via* TRIM and TRIDYN confirmed that the maximum concentration of silver lied within 30 – 47 nm from the surface. The RBS data verified the presence of Si, Al, N, Ag, and O_2, whose concentration varied with temperature. X-ray diffraction and electron microscopy corroborated the crystallinity of the AlN epilayer. Electron diffraction confirmed both the epitaxy of the AlN film on the (001) Si substrate and the crystalline quality of the epilayer prior to and after the thermal annealing treatment. Electron microscopy revealed that the sputtered AlN film grew epitaxially in a columnar morphology and silver precipitates did form in some of the aluminum nitride samples implanted but only in those implanted with a higher concentration of Ag under high-energy implantation conditions.

It is concluded that the Ag implanted region does indeed have potential as a buried contact layer for piezoelectric activation and sensing if the critical concentration and appropriate thermal conditions can be attained.

Dedicated to the memory of the virtuous women in my life:

my grandmother Mamie Johnson and mentor Duella Smith

and

to my children:

for their sacrifice, devotion, patience, guidance,

unconditional love and innumerable teaching moments.

TABLE OF CONTENTS

CHAPTER 1. INTRODUCTION

CHAPTER 2. BACKGROUND

CHAPTER 3. EXPERIMENTAL PROCEDURES

CHAPTER 4: RESULTS

CHAPTER 5: DISCUSSION

CHAPTER 6: CONCLUSIONS

CHAPTER 6: Future Work

REFERENCES

APPENDIX

List of Tables

List of Figures

ACKNOWLEDGEMENTS

With sincere gratitude, I would like to thank several individuals who have contributed to my success. First and foremost, my Lord and Savior for the strength, patience, wisdom, perseverance, and tenacity to complete a job that only He can provide the strength to bring to fruition. Lionel Alleyne, my husband and my rock, for his love, support, patience, advice, commitment, financial support, and dedication to allow me to achieve my goal. A goal that become our goal. My children, Brianna, Ari, Micah, and Joshua, who are invaluable blessings in my life and true gifts from God. Thank you for allowing me to be your teacher and for being my teacher. My parents, Kenneth and Connie Waluyn, and grandparents, Leonard and Mamie Johnson, for their guidance, support, dedication and for instilling values such as education and self-pride that I am proud to instill in my own children. I would like to thank my in-laws, Adelbert and Phyllis Alleyne for their support, encouragement, assistance, and love for more than 16 years.

I would like to thank my committee members, Professors Ronald Gronsky, Oscar Dubon and Alice Agogino for their guidance and support throughout the duration of this project, as well as the number of other projects I've worked on while as a graduate student at UC Berkeley. Thank you for supporting me in both aspects of my life, as a researcher as well as a parent and wife. My advisor, Professor Gronsky, for his mentorship, leadership, guidance, support, and friendship throughout my graduate education. I thank my collaborator Professor Al Pisano (ME Dept.) and his former students Dr. Debbie Senesky (now at Stanford University) and Dr. T.-T. Yen (now at Texas Instruments) for providing me with the AlN thin film samples utilized for this work; without their generous support this work would not be possible. This research would not have been possible without the assistance of Dr. Andre Anders, Dr. Kin-Man Yu and Dr. Sunnie Lim of the Lawrence Berkeley National Lab (LBNL), who taught me about ion implantation and RBS and shared their training and expertise with me. I would like to acknowledge the support of Professor Andrew Minor for allowing me to utilize his research facility to complete this project. For his dedication and tenacity in the development and completion of this project, I would like to acknowledge my former undergraduate student Mr. Matthew Ford (currently Ph.D. student at Northwestern University). Elizabeth Boatman and Maria Ghandman for not only their countless hours with me in the dark TEM room but also making graduate school enjoyable. Melissa Santala for her insight and support. For invaluable discussions, support and advice throughout my graduate education I would like to thank Wanda Capece, Catalina Estrada, and Chris Kumai, and the rest of the Materials Science & Engineering Department staff.

My family: Johnson Family, Alleyne Family, Rebecca Fabiano, Danielle Rush, Rita Pollak, Cindy and Roy Hill-Ford, Falomi Ivery, Ruby Bates, Jonelle Campbell, Gwen Smith, Craig and Colleen Gentry, Edwin and Regina Johnson, and Tim and Theresa Richardon, as well as all my extended family and friends for their thoughts, inspiration, prayers and support. I would also like to acknowledge all the early-childhood education and primary school teachers for helping me to educate and prepare my children during my years of study.

I am very grateful for financial support provided by the University of California, Berkeley Dissertation-Year Fellowship, Founder Region Soroptimist Fellowship, Dean's Office California Legislative Grant Fellowship, and National Science Foundation (NSF). Additional funding provided by my advisor through the Arthur C. and Phyllis G. Oppenheimer Chair in Advanced Materials Analysis is also gratefully acknowledged.

CHAPTER 1. INTRODUCTION

1.1 Motivation

My interest in alternative materials for applications as micro-electro-mechanical systems (MEMS) and nano-electro-mechanical systems (NEMS) developed as a result of my participation in a collaborative and multidisciplinary group based project organized by Professors Alice Agogino from the University of California, Berkeley, and Leslie Speer from the California College of Arts and Design (currently a faculty member at San Jose State University). The goals of the project were to generate and develop solutions to issues of concern for an underserved community. Through preliminary investigations and research the team identified the migrant community as the target market with emphasis placed on those individuals who "resided" in California's Central Valley. An area of grave concern for this community is pesticide poisoning and exposure. Consequently a study was undertaken to mitigate the harmful effects of pesticides in the farmworker community — including men, women and children. This project was later branded *Seguro* — which means "safety" in Spanish.

As a result of on-site, in-depth cultural and user research, *e.g.* workshops co-facilitated by the Anita-Borg Institute, focus groups and interviews with customers in the target market, several areas of technological development were identified in our brain-storming sessions. These opportunities included:

(1) water purification in the home and field to combat pesticide and chemical pollution;
(2) air purification in the home and at schools;
(3) laundry detergents;
(4) protective gear for workers at home and work for example masks and work apparel;
(5) methods of keeping pesticides out of the home and schools;
(6) information dissemination that educates the migrant community about pesticides and infant mortality;
(7) food cleansers; and
(8) sensors to monitor pesticide toxicity levels in the home and fields.

As a group we focused our attention on (4) while (6) and (8) were developed as independent projects by several members of the team. My interest in (8) led to further investigations of current and future sensor applications including the "μChem Lab on a Chip" developed by Sandia National Laboratory for military applications.[1,2]

Based on an intensive literature review, several sensors were identified.[1,3-17] In addition, other technologies with similar architectures were found to include magnetic read heads, magnetic random-access memory (MRAM), resonators, actuators, and smart grid electrical systems. All of these technologies employed a metal bonded to a ceramic and thus relied on the integrity of the bond between two dissimilar materials. In fact, failure at the metal-ceramic interface would result in serious engineering issues.

Despite more than a decade of experience in manufacturing of MEMS incorporating metallic and ceramic elements, modern devices are still plagued by delamination at their metal/

ceramic interfaces. To understand the delamination problems observed in these devices, it is essential to pursue one of the following pathways:

I. Conduct fundamental studies identifying the causes of delamination and/or
II. Explore alternative manufacturing processes and assess their feasibility.

Fundamental studies of delamination would be useful to discern the failure mechanisms in service when compared with intact original interfacial structures. Studies of alternative processing methodologies would be useful for extending manufacturing of MEMS/ NEMS devices that require a metal/ceramic contact. Under the appropriate experimental conditions, qualitative and quantitative data could be extracted to elucidate the stability of the metal/ceramic interface over a range of in-service conditions. For this project, we chose to explore an alternative manufacturing process and assess its feasibility.

1.2 Methodology

This study investigates a number of new approaches to materials processing in MEMS/NEMS devices. One is the implementation of buried contact layers generated by ion implantation of silver (Ag) and its subsequent precipitation. Another is the choice of aluminum nitride (AlN) as a candidate piezoelectric due to its compatibility with complementary-metal-oxide semiconductor (CMOS) manufacturing and its attractiveness as a lead (Pb)-free alternative to lead zirconate titanate (PZT). Not only does Ag have appropriate electrical properties, its melting temperature is low enough to employ annealing temperatures needed to induce Ag diffusion in the AlN matrix within experimentally accessible times. For commercial applications, this would be a factor as post-CMOS processing conditions are limited to temperatures below 450°C.

Many methods for generation of buried contact layers were considered, including

(1) conventional ceramic powder processing techniques,[18,19]
(2) internal oxidation of metal alloys,[20,21]
(3) internal reduction of a metallic species in a multi-metal oxide,[22,23]
(4) microfabrication techniques combined with diffusion bonding,[24,25] and
(5) ion implantation followed by a thermal annealing treatment.[26-42]

We chose (5) to attain a high concentration of Ag nanoparticles in AlN while risking significant damage to the matrix that is known to result,[43,44] especially under high ion energy conditions, because crystallinity can be recovered *via* post-implantation annealing.[45]

Computer simulations by Transport of Ions in Matter (TRIM)[46,47] and TRIDYN,[48,49] coupled to Rutherford backscattering spectrometry (RBS), x-ray diffraction (XRD), scanning electron microscopy, and transmission electron microscopy have been employed to characterize the depth-profile and microstructure after implantation and post-annealing. Quantitative and qualitative data including depth, dose, Ag distribution, and orientation relationships are reported in this work.

1.3 Objectives

The goals of this study are to:

- evaluate the structural evolution of Ag nanoparticles in an AlN matrix as a function of ion implantation and thermal annealing conditions;
- understand the resulting phase transformation behavior during Ag precipitation in a ceramic matrix; and
- evaluate the distribution of Ag nanoparticles in an AlN matrix.

The identification of Ag nanoprecipitates, their distribution and orientation within the AlN matrix will determine the feasibility of using ion implantation as a means to form metal particles in a ceramic matrix at a concentration adequate to generate a sub-surface conducting layer. The scientific understanding obtained from this study will support future work on interfacial phenomena at the metal/ceramic interface in general, and control of the electrical operation of AlN in MEMS/NEMS applications in particular.

CHAPTER 2. BACKGROUND

Piezoelectric materials are ubiquitous in micro-electro-mechanical systems (MEMS), and more recently nano-electro-mechanical systems (NEMS). They can be found in such commodities as mobile phones and watches as well as more technologically advanced products including gyroscopes and sensors. Due to their versatility, these materials can also be utilized in optoelectronic applications as transducers to trigger light emitting diodes (LEDs), laser diodes, and photo-detectors. With advancements in technology and the demand for miniaturized devices, there is a greater demand for more precise fabrication processes and smaller and more efficiently integrated systems. In this section an overview of piezoelectric materials as well as current and potential fabrication processes and challenges are discussed. Research in this field is also presented to provide the framework for my doctoral work.

2.1. Piezoelectricity

There is a certain class of materials that exhibit a phenomenon called "piezoelectricity." The term *piezoelectricity* is derived from the Greek word *piezo* meaning "to squeeze." Piezoelectricity is the ability of certain crystalline materials to develop an electric dipole when "squeezed," or to exhibit an induced mechanical strain when subjected to an applied voltage. Such materials have a non-centrosymmetric crystal structure as needed to respond to an application of a mechanical stress or voltage.[50-52] Twenty-one of the thirty-two crystallographic point groups exhibit this symmetry but only eighteen of these show piezoelectric behavior. In contrast, crystals with centrosymmetric structures do not exhibit this behavior. When a voltage is applied across a centrosymmetric material the material becomes strained but the center of mass of both charges (negative and positive) preserves zero net polarization in the unit cell. In essence, piezoelectric materials provide a transduction mechanism between electrical and mechanical energies.

2.1.1. Piezoelectric Effect

Piezoelectricity is commonly described in terms of the piezoelectric effect. In 1880 the Curie brothers, Jacques and Pierre, discovered the piezoelectric effect in Rochelle salts.[53] Further research revealed that this effect could be further categorized into the direct and converse piezoelectric effects.[53] To fully understand this phenomenon it is instructive to first consider Hooke's Law.

Hooke's Law

Piezoelectricity is the combined effect of Hooke's Law and the inherent electrical behavior of the material. Hooke's Law is used to describe the relation of stress (T) and strain (S) in linearly elastic media. It is governed by the following equation:[54]

$$S = sT \text{ or } T = cS \tag{2.1}$$

where s is the elastic compliance constant and c is the elastic stiffness constants. Similarly, the correlation between electrical charge density displacement (D) and electric field (E) can be expressed by Equation 2.2.[54]

$$D = \varepsilon E \text{ or } E = \beta D \tag{2.2}$$

where ε = dielectric permittivity constant and β = dielectric impermittivity constant. In this treatment the stress and strain terms are defined by tensors and electric field and electric charge density displacement are defined as vectors. The constitutive equations for piezoelectricity are governed by[50,55]

$$\begin{array}{ll}
\begin{cases} S = s^E T + dE \\ D = \varepsilon^T E + dT \end{cases} & d\text{-form} \\
\begin{cases} S = s^D T + gD \\ E = \beta^T D - gT \end{cases} & g\text{-form} \\
\begin{cases} T = c^E S - eE \\ D = \varepsilon^S E + eS \end{cases} & e\text{-form} \\
\begin{cases} T = c^D S - hD \\ E = \beta^S D - hS \end{cases} & h\text{-form}
\end{array} \tag{2.3}$$

where forms d, g, e, and h represent the piezoelectric coefficients coupling the electrical and mechanical domains. Additional information on piezoelectric coupling coefficients can be found in the literature.[50,52,55]

Direct Piezoelectric Effect

The direct piezoelectric effect occurs when a crystal experiences a mechanical force such that an electrical polarization is produced. The magnitude of polarization is governed by the following equation:[50,56]

$$D = d_{ij} T + \varepsilon^T E \tag{2.4}$$

where the superscript T indicates a zero or constant stress field. The piezoelectric coefficient has units of Coulomb/Newton (C/N).

Converse Piezoelectric Effect

The converse piezoelectric effect occurs when a crystal is electrically polarized to generate mechanical deformation, with the latter proportional to the polarizing field. The magnitude of induced strain is governed by the following equation:[50,56]

$$S = s^E T + d_{ij} E \tag{2.5}$$

where the superscript E indicates a zero or constant electric field. The piezoelectric coefficient has units of meters/Volts (m/V).

High piezoelectric coefficient values are desirable for materials intended to develop motion or vibration. As Equations 2.4 and 2.5 illustrate, materials that experience a low stress and/or low electric field produce a large d_{ij}, thus a measurable response can be produced with little pressure and/or applied field. It is important to note that under these conditions the structural integrity of the material is retained. Materials that exhibit these characteristics are ideal for energy-scavenging applications, which will be the subject of further discussion in §2.3.

2.1.2. Electromechanical Coupling Coefficient

A property of particular interest is the electromechanical coupling coefficient, k. The electromechanical coupling coefficient is used to describe the coupling response between the electrical and mechanical energies. It is determined using the following equations:[50]

$$k^2 = \frac{\text{Mechanical energy converted to electrical energy}}{\text{Electrical energy converted to mechanical energy}}$$

$$k^2 = \frac{\text{Electrical energy converted to mechanical energy}}{\text{Mechanical energy converted to electrical energy}} \qquad (2.6)$$

The electromechanical coupling coefficient represents the efficiency during conversion of electrical to mechanical energy (and vice versa) and is the best measure of strength of the piezoelectric coupling coefficient. Several factors play a role: composition of solid solution, average grain size, polycrystallinity, and device geometry. Materials with high k-values are ideal for energy-scavenging, transducer, gyroscope and sensor devices.[57]

2.2. Piezoelectric Materials

Since the discovery of piezoelectricity in Rochelle salts, a number of other materials have been observed to exhibit such effects: tourmaline, zinc blende, quartz and even wood.[58] The feasibility of polycrystalline piezoelectric ceramics including barium titanate ($BaTiO_3$), zinc oxide (ZnO), lithium niobate ($LiNbO_3$), and lead zirconate titanate (PZT) have also been explored.[15,59,60] To date commercial applications have evolved to favor PZT[61] for its combination of superior properties. Nevertheless the presence of lead in these ceramic compounds raises objections to their application in anything "green" due to potential health implications during their manufacturing, recycling, or in-service applications, if leaching occurs. Fortunately the search for alternative piezoelectrics has been underway for several years,[62] generating renewed interest in the materials engineering community of such old standbys as silica (SiO_2) and more recently, aluminum nitride (AlN). An abbreviated list of materials, their properties and applications are presented in Table 2.1. We have pursued the application of AlN as a non-toxic alternative to PZT in this study, seeking processing pathways to augment the modest piezoelectric performance of AlN[63-65] and exploit its compatibility with complementary metal-oxide semiconductor (CMOS) manufacturing.

2.3. Applications

Piezoelectric materials have found utility in a myriad of applications including sensors, transducers and more recently in energy-scavenging and gyroscope devices. Further consideration will be given to sensors and energy-scavenging applications, as these provided the foundation of this work.

2.3.1. Micro-electro-mechanical Systems (MEMS)/ Nano-electro-mechanical Systems (NEMS)

Micro-electro-mechanical systems (MEMS) are small mechanical devices powered by or used to generate electricity.[66] They are often fabricated using conventional microelectronic manufacturing methods. Since the integration of such devices their sizes have continued to decrease, leading to the development of nano-electro-mechanical systems (NEMS).[66]With the increasing demand for clean and renewable energy sources, there is an even greater urgency to develop more efficient, cost-effective NEMS-based devices using alternative materials. Such materials include ceramics (AlN, ZnO),[67] semiconductors (Ge, GaN, SiC),[67] and polymers (polydimethylsiloxane (PDMS), polycaprolactone (PCL), and polyesters).[68] Strict requirements for chemical, mechanical, and thermal stability place constraints on the materials that can be employed in MEMS/NEMS devices. An abbreviated list of materials is presented in Table 2.2.

To date, MEMS/NEMS-based systems have been incorporated in various devices and applications in industrial, military and consumer markets. They have been utilized in sensors, actuators, accelerometers and even such household electronics as refrigerators and cell phones.[69] In the biomedical field they have influenced the design of microactuators, microfluidic systems, microneedles, micropumps, microfilters, and microsensors.[70,71] More recently NEMS have found utility in the energy-scavenging realm, and in particular applications as gyroscopes.[72-74] To fully understand the design challenges in MEMS-based devices with respect to the piezoelectric/metal interface, further discussion of surface acoustic wave sensors (SAWs)[50,75,76] and energy-scavenging devices[77,78] is fruitful. Additional information on MEMS-processing is provided in Appendix 1.

2.3.2. Surface Acoustic Wave (SAW) Sensors

In an effort to develop solutions to pesticide poisoning in farmworker communities, intensive research was conducted on current sensors. Based on my search, I identified the surface acoustic wave (SAW) sensor as one of the most promising technologies. In addition to chemical sensing, acoustic wave sensors have been utilized to detect changes in pressure, torque, and mass.[50,75,76,79,80] Over the years, SAW devices have grown in popularity, especially in the telecommunications industry where over 3 billion SAW devices are manufactured annually for applications as bandpass filters in cellular phones and base stations.[81-85]

The typical SAW design consists of a metal deposited onto a piezoelectric substrate and patterned into input and output interdigitated transducers (IDTs).[15] The transducers can be deposited through either physical or chemical means including radiofrequency (rf), direct current (dc) or magnetron sputtering,[86-89] chemical vapor deposition (CVD),[90,91] and molecular beam epitaxy (MBE).[91] Deposition can also be simple, such as the evaporation methodologies used for the μChem Lab device.[1,2,] Candidate metal/piezoelectric systems for use in surface acoustic wave devices include gold/chromium/quartz/platinum (Au/Cr/SiO_2/Pt), aluminum/quartz (Al/ SiO_2), Au/Cr/$LiNbO_3$, and Al/$LiNbO_3$, among others.[1,2,76,91-94] The metal/piezoelectric bonding configuration provides the necessary connections essential for the generation and detection of acoustic waves in piezoelectrics.

After deposition onto the piezoelectric substrate, the metallic overlayer is patterned *via* conventional lithographic techniques to establish the morphology of interdigitated electrodes.[15,95] Activating these electrodes stimulates the piezoelectric crystal on the input side, generating both bulk and surface acoustic waves. The surface wave is detectable by another set of electrodes on the output side of the device.[15,60] Consequently, the performance of the surface acoustic wave sensor is dependent on the electrical-mechanical coupling between the piezoelectric substrate and the metal interdigitated transducers and the nature of the metal/ceramic interface is a critical component in the design and operation of these devices.

2.3.3. MEMS-based Energy Scavenging Devices

"Smart grid" electrical systems incorporate a variety of energy sources and energy storage protocols, many of which are entering the design phase for commercial and metropolitan applications. One of the more attractive sources of green energy has roots in the popular recycling theme of other green technologies, now known by the term "energy scavenging."[96] Energy scavenging is a process whereby energy derived from an external source is captured and stored for future use. Due to an increasing trend in energy consumption as illustrated in Figure 2.1,[96] there is an imperative need to identify and develop alternative energy sources.

Alternative energy sources under current investigation include chemical and biological reactivity, as well as ambient (solar, wind, water, mechanical) and nuclear energies. However, for energy harvesting applications, the energy must be in a form that is suitable for storage and conversion for further utilization. In addition it must be economically feasible. Research has shown that scavenging energy from heat, wind, light, and vibrational forces could be utilized to power low-power consumption electronic devices and smart sensors.[15,97] Scavenging *via* vibrational forces is of particular interest to this work although a brief review of other methods can be found in the literature.[97]

In its most promising conformation, energy scavenging converts cyclic mechanical vibrations in the environment or random mechanical pressure pulses, caused by sources ranging from operating machinery to human footfalls, into electrical energy *via* piezoelectric transducers. Such systems are manufactured in a similar fashion to SAWs and therefore exhibit similar design characteristics and pose similar challenges.[77,78,98] We have applied our knowledge of SAWs to NEMS-based scavenging devices to address the design limitations found in such systems.

2.4. Design Challenges

Despite more than a decade of research in MEMS systems incorporating piezoelectric elements, modern devices are still not meeting the optimal standards of performance.[99-105] Several investigators cite reasons for performance deficiencies found when comparing theoretical to experimental performances of surface acoustic wave devices. Included in the list are the selection of the piezoelectric substrate and its orientation or "cut" in the electrical engineering vernacular, the selection, patterning and thickness of the metallic contact layers used as interdigitated transducers to create and detect SAW motion, and the presence of spurious adsorbates on the detector surface.[76,106-120] In this work we add the nature of the metal/piezoelectric interface as a potential avenue for optimization.

Delamination is of grave concern to device performance,[117] as the electric field essential to generate and sustain the piezoelectric response of these devices is lost, resulting in device failure. Technological advancements in surface modification and embedded layer techniques have potential use to mitigate such effects. Experimental methods to form embedded metal nanoparticles, particularly in ceramics, include conventional ceramic powder processing,[18,19] internal reduction of metallic species in multi-metal oxides,[22,23] internal oxidation of metal alloys,[20,21] microfabrication techniques combined with diffusion bonding,[24,25,121] and ion implantation.[36,37,40,122] Based on current device design specifications and the ability to form a variety of metallic nanoparticles in dielectric media, we have undertaken an investigation of metal nanoparticle formation *via* ion implantation to form buried contact layers. For the purposes of this work, research investigations that employed ion implantation to form nanoparticles in ceramic materials are presented below.

2.5. Literature Review

For over 30 years, ion implantation has been the method of choice in the semiconductor processing industry to introduce controlled dopant concentrations in semiconductor materials.[123,124] It is a method employed to exceed impurity equilibrium solid solubility limits and thus can be used to modify the structural and electrical properties of materials. This method was initially employed to fabricate p-n junctions in silicon devices however more recently it has been utilized to modify the structural, mechanical and electrical properties of metals,[125] semiconductors,[126] insulators,[31,42,121,127-131] and even polymers[132] for a multitude of applications. The term "insulator" is used to denote any material that has a large band gap of at least 2.0 eV. Such applications include magnetic storage devices,[133,134] diluted magnetic semiconductors (DMS) for spintropics,[30,41,128,135-138] resonators,[128,139] light emitting diodes (LEDs),[44,63,129,140] optics,[29,121,130,141-143] acoustic wave devices,[63,131] and biomedical devices.[144] In this section we present an overview of the structural effects of ion implantation in AlN.

Manganese (Mn) in AlN

The desire to enhance the performance of DMS materials has led to an increase in interest of ion implanted III-V compounds such as manganese (Mn)-implanted AlN. This element was selected because it shows great promise for the development of ferromagnetism in AlN. Research conducted by Frazier *et. al.*[128] and Li *et. al.*[145] have provided much insight on the effects of post-thermal annealing treatments on structure and phase formation in such materials.

Frazier and co-authors[128] investigated the structural characteristics of Mn-implanted AlN at 250 keV at 573 K (300^{o}C) followed by a post-annealing treatment at 1223 K (950^{o}C) for 2 minutes in nitrogen to acquire a dose of 3×10^{16} cm^{-2}. Methods employed include photoluminescence (PL), magnetometry using the superconducting quantum interference device (SQUID), x-ray diffraction (XRD), and two-terminal resistivity. Results of particular interest are those acquired using XRD.

The XRD results indicated that there were several orientations of AlN present in the sample. Peaks for both AlN (epilayers) and Al_2O_3 (substrates) were identified and indexed: 0002 0004 and 0002, 0006, and 0012, respectively. No peaks were detected for Mn. Additionally, a broad peak was visible at $2\theta = 20^o$ due to damage induced by the implantation process. However, from this study, the preferential sites for Mn in AlN cannot be clarified.

The preferential sites for Mn implanted in AlN were later revealed by the research conducted by Li and co-authors.[145] Implantation was conducted at 200 keV such that a dose of 5×10^{16} ions/cm^2 was obtained. Subsequently, a post-annealing treatment at temperatures that ranged from 573 K (300^{o}C) to 773 K (500^{o}C) was conducted to monitor the effects of annealing. Cathodoluminescence results confirmed that Mn substituted for Al at a concentration that increased with annealing temperature. This was primarily due to higher solubility of Mn at higher temperatures. In addition, the samples were highly damaged with a significant concentration of defects. Similar results were acquired for indium (In)- and strontium (Sr)-implanted AlN and gallium nitride (GaN),[121] In-implanted GaN,[121] In- and hafnium (Hf)-implanted AlN,[122] rare-earth (RE) metals (europium (Eu), erbium (Er), thulium (Tm))-implanted AlN,[146] and Mn-implanted ZnO.[42] No secondary phases were detected. It is important to note that the valency for Mn (as well as cobalt (Co) and chromium (Cr)) differs from that of Al — Mn has a $^+2$ charge while Al has a $^+3$ charge state. These results confirmed that the preferred sites for ion implanted Mn were substitutional sites; no secondary phases formed.

Based on the work by Frazier *et. al.*[128] and Li *et. al.*[145] it was concluded that short-range disorder developed during implantation and the preferred sites for Mn implanted in AlN were substitutional sites with the concentration of sites occupied determined by post-thermal annealing conditions.

Copper (Cu) in AlN

Based on earlier work on ion implantation in AlN with transition metals, it was anticipated that ion implantation might be a feasible method to form nanoprecipitates. Traverse *et. al.*[147] demonstrated the formation of copper (Cu) nanoprecipitates in an AlN matrix using ion implantation to identify the local atomic environment of the nanoprecipitates. The purpose of this work was to identify the preferred site for Cu in the AlN matrix and therefore its local atomic environment. Polycrystalline AlN was implanted with Cu^+ ions at an implantation energy of 100 keV, at temperatures of 80 K (–193^{o}C) and 300 K (27^{o}C), and a fluence of 10^{17} ions/cm^2. To understand the correlation between thermal annealing and precipitate size, implanted AlN samples were annealed at 1073 K (800^{o}C) for 1 and 5 hours. Pre-annealed samples formed nanoprecipitates that averaged 1.1 nm in size while 4.0 nm-sized nanoprecipitates were identified in the annealed samples. The shape of the Cu signal, as acquired *via* extended x–ray absorption fine structure spectroscopy (EXAFS), was similar to pure Cu. Therefore it was concluded that the Cu atoms were not dispersed in the matrix but had Cu neighbors in the face-centered cubic (FCC) configuration. Similar results were found for Cu-Cu interactions in AlN as conducted by Borowski and co-authors.[127]

Borowski *et. al.*[127] also illustrated that ion profiles varied with implanted species as distinct variations in the profiles of Cu, iron (Fe) and titanium (Ti) were observed. Sintered AlN samples were implanted at room temperature (RT) at 100 keV with a secondary implantation energy of 30 keV (Cu), 80 keV with secondary implantation energy of 20 keV (Fe), and 80 and 70 keV (Ti), respectively. The purpose of the secondary implantation step was to produce a more homogeneous implantation profile near the surface. Ion doses ranged from 0.6 × 10^{16} ions/cm^2 to 2.4 × 10^{17} ions/cm^2. A post-annealing treatment was performed for the Fe and Cu implanted samples at 1073 K (800^{o}C) for 1 hour in vacuum. A comparative analysis of the experimental and theoretical data was conducted.

The RBS data confirmed the presence of a homogeneous Cu profile for doses of 1 × 10^{17} cm^{-2}; however, for higher doses (2.4 × 10^{17} cm^{-2}) the distribution was no longer homogeneous — less Cu was visible at larger depth and an increase in concentration was observed near the surface. For samples annealed at 1073 K there was a 25% and 50% reduction in Cu concentration for samples implanted with a dose of 1.6 and 1.8 × 10^{17} ions/cm^2, respectively. Similarly, homogenous profiles were observed in the Fe and Ti implanted samples. However, no ion loss was observed in post-annealed Fe and Ti samples. This behavior was hypothesized to result from secondary compound formation. To test this hypothesis, extended x-ray absorption fine structure (EXAFS) was employed.

The EXAFS results revealed that samples implanted with Ti, Fe and Cu formed all Ti-N bonds, Fe-N bonds and Fe clusters, and Cu clusters, respectively. These newly formed compounds were highly stable, even with annealing at 800^{o}C, due to their high bond dissociation energies. Profile results for as-implanted Fe samples were similar to those acquired for Cu implanted samples. However, in contrast to the results obtained for Cu annealed samples, the number of Fe atoms detected was unchanged in the annealed samples. Similar results were acquired for Ti-implanted AlN. However EXAFS was unable to distinguish between elements in different states and therefore could not validate the presence of precipitates that formed out of solution. In summary, the work of Borowski[127] and Traverse[147] revealed that changes in ion concentration, as a result of annealing, depended on fluence, implanted ion species and formation of stable precipitates.

As reported in the work of Traverse *et. al.*[147] deviations in the theoretical and experimental data were also observed in Cu-implanted AlN samples. Modeling using Transport Ions in Matter (TRIM) indicated that the distribution profile for Cu in AlN was centered at 54 nm from the surface with a full-width half-maximum (FWHM) of 44 nm while the maximum defect concentration would be located at 35 nm. Experimental results from RBS revealed that the Cu profile was centered at 39 nm with a FWHM of 64 nm. Thus the experimental data matched well with the defect profile. This was attributed to heterogeneous precipitation of Cu at defect sites, particularly dislocation loops. In addition, the Cu concentration for the annealed samples with respect to the unannealed samples decreased from 14% to 11% while the shape of the curve was consistent for both samples. Similar results — discrepancies between experimental and theoretical ion distribution profiles and changes in concentration with annealing — were found in the literature for Cu implanted in bulk AlN at 100 and then 30 keV and annealed at 1073 K (800^{o}C) for 1 hour in vacuum, as reported by Borowski and Traverse.[127]

The RBS data indicated that the Cu profile is closer to the surface and wider than that predicted using TRIM91.[147] However, the vacancy distribution matched well. The deviations in profiles were attributed to the diffusion of Cu such that Cu ions occupy sites much closer to the surface than predicted. However, this could also be attributed to deviations in the sputtering rate at the surface, threshold displacement energy at the surface with respect to the bulk and dynamic annealing that can occur during implantation, as the latter was not accounted for using TRIM. Similar deviations — experimental data inconsistent with projected ion profile as predicted *via* TRIM — were observed in the literature for Au, rare earth metals (Eu, Er, Tm), Fe, and hydrogen (H) in ZnO,[39] AlN,[44,127,146,148,149] and other III-V compounds.[150] It is also important to note that no amorphization was observed in the latter samples.

Oxidation effects of Cu implanted in AlN have also been reported. Yamada *et. al.*[151] implanted Cu in polycrystalline AlN at an implantation energy of 150 keV at RT to a dose of 1 × 10^{16} to 1 × 10^{17} ions/cm^2. Auger electron spectrometry (AES) results indicated that an oxide layer (AlO, AlON), approximately 20 nm thick, formed at the surface. Oxygen was also found in layers deeper below the surface as a result of diffusion. Later work on unimplanted AlN samples by Lee and co-authors[152] confirmed that oxidation commenced in the 800 – 900^{o}C temperature range and the surface was completely covered with an Al_2O_3 oxide layer by 1100^{o}C.

Based on the work of Traverse,[147] Borowski,[127] and Yamada,[151] the following results would be expected for ion implantation of Cu in AlN: no formation of secondary phases (Cu-Al, Cu-N), formation of Cu nanoprecipitates with an average size of 4.0 nm, minor statistical errors between experimental and theoretical results (TRIM *vs.* RBS) and a reduction in ion concentration with annealing.

Gold (Au) in AlN

It has been documented that structural damage of crystalline materials can occur as a result of ion implantation. This has been observed in Au-implanted AlN at energies of 300 keV and 1 MeV. The purpose of these works was to further develop processing technologies of AlN for optoelectronic applications.

Kucheyev *et. al.*[148] investigated the structural damage developed in AlN as a result of bombardment with 300 keV Au$^+$ ions with the intent to study the behavior of damage buildup and the microstructure of ion-beam induced defects. Implantation was conducted with an implantation energy of 300 keV at liquid N_2 (LN_2) and RT to achieve a dose of 8 × 10^{13} to 4 × 10^{16} ions/cm^2. Samples were subsequently annealed *via* rapid thermal annealing (RTA) for 1 minute. Rutherford backscattering/channeling (RBS/C) results revealed that implantation-produced lattice disorder in the bulk was dependent on ion dose and independent of implantation temperature. As the ion dose increased in samples prepared at both LN_2 and RT there was an increase in implantation-produced lattice disorder in the bulk. Once a dose of 4 × 10^{16} ions/cm^2 was reached, an amorphous layer formed. It was further revealed that implantation generated disorder was stable up to 1273 K in both samples to doses ≥ 1 × 10^{16} ions/cm^2. This was consistent with the literature as temperatures between ⅓ and ½ of the melting temperature (T_m) were most effective in removing defects in materials. Therefore, based on the melting temperature for AlN, annealing temperatures ≥ 2173 K (1900^{o}C) would be required to anneal out induced damage. These results were consistent with data acquired *via* transmission electron microscopy.[148]

To elucidate the extent of structural damage in ion implanted AlN imaging analysis was performed. Transmission electron microscopy results revealed that samples prepared at RT were highly damaged but not amorphous.[148] Images collected for samples implanted at a dose of 5×10^{15} ions/cm^2 at LN$_2$ revealed low density defects in the near-surface region up to ~ 500 Å (50 nm) from the surface and a dense band of defects at larger depths. However micrographs collected for samples implanted with a higher dose of 3×10^{16} ions/cm^2, under the same conditions, exhibited a dense band of defects extending all the way to the surface. There was no evidence of amorphization. Strong dynamic annealing of ion beam defects occurred such that no lattice amorphization occurred even for larger doses.

In contrast to the results published by Kucheyev *et. al.*[148] research conducted by Jiang and co-authors[44] revealed that amorphization does occur in ion implanted AlN at higher fluence. Aluminum nitride films were implanted with 1 MeV Au$^+$ ions at a temperature of 145 K to achieve fluences of 2.3 to 424 ions/cm^2. A post-thermal annealing treatment was conducted at RT for 72 hours. Using RBS/C, researchers found that the Au peak shifts closer to the surface with increases in ion fluence. For example, the Au peak maximum for samples implanted with a fluence of 5.4 ions/cm^2 (or less) was located 107 nm from the surface while for a fluence of 424 ions/cm^2 the peak maximum was located at 81 nm from the surface. This could be attributed to ion sputtering of the surface during the implantation process, however this could not be confirmed with the methods employed by these investigators. They also found that full amorphization could not be detected in samples even at the highest fluence of 424 ions/cm^2.

Transmission electron microscopy images however confirmed the presence of an amorphous surface layer, approximately 20 nm thick, in samples implanted with a fluence of 366 ions/cm^2. A nanoscale crystalline structure, well aligned with the substrate, as well as amorphous domains were evident. It was speculated that the amorphization of AlN occurred due to the generation of point defects and small defect clusters during implantation as a result of a high density of energy deposition from the heavy-ion irradiation (1 MeV). Since implantation was conducted at low temperature these defects were stable and therefore unlikely to anneal out during irradiation. Thus, the local amorphization presented in these samples was the result of defect interaction and defect-stimulated processes. Similar results were reported in GaN.[43] Thus, it was once again confirmed that the degree of amorphization was dependent on implantation energy, implanted species and dose, as prior studies repeatedly demonstrated. The work conducted by Kucheyev *et. al.*[149] and Jiang *et. al.*[44] again reinforced the need for microscopy at high spatial resolution to confirm the degree of damage and amorphization during ion implantation.

Summary

Based on the intended applications of AlN as a functional piezoelectric agent in energy-scavenging devices, requiring metallic contacts to fabricate interdigitated electrodes essential to generate and detect acoustic waves, and in recognition of the potential for delamination of surface-deposited electrical contacts, this dissertation intends to explore the use of buried contact layers generated by ion implantation. Metallic Ag has been selected for implantation in AlN due to its low electrical resistivity of 1.6 × 10^{-8} Ω·m[153] and CMOS compatibility. The depth profile and microstructural evolution of implanted AlN (many different ionic species) has been documented in prior work to depend on implanted species, implantation energy, and dose. However, to the author's knowledge, no investigations on the influence of annealing on microstructural evolution in Ag-implanted AlN have been reported. This is the objective of the current study.

2.6. The Ag/AlN System

The Ag/ AlN system was selected because the two materials have suitable material properties for the intended applications, can form strong interfacial bonds, and can remain chemically stable at temperatures (T) below 1000 K. In addition, aluminum nitride is compatible with CMOS technology. The latter is essential as it facilitates an easy adoption with current manufacturing processes for commercialization.

Aluminum Nitride (AlN)

Aluminum nitride is an intrinsically poled, non-ferroelectric (no Curie point) synthetic (does not occur in nature) piezoelectric material. It was initially synthesized by F. Briegleb and A. Geuther in 1862 when aluminum was heated in a nitrogen atmosphere at 700°C.[154,155] It was further discovered that crystallization can occur in two forms, zinc-blende (cubic) and wurtzite (hexagonal close packed (HCP)), as illustrated in Figure 2.2. Experiments have also shown that a structural transformation to a semiconducting rocksalt (cubic) structure is possible at high temperatures and pressures.[156-158]

The wurtzite phase of AlN has lattice parameters of a = 3.112 Å and c = 4.978 Å.[159] It has a melting temperature (T_m) exceeding 2000°C and is stable up to very high temperatures in an inert atmosphere. However, in air, surface oxidation occurs above 700°C and accelerates at $T \geq 1000$°C. The phase diagrams for Al-N and Al-N-O are shown in Figures 2.3 – 2.5. The thin oxide film protects the material up to 1370°C, the point when bulk oxidation occurs. Additionally, it is a good thermal conductor with a thermal conductivity of 320 W/m·K.[160] It has an acoustic wave velocity almost twice that of other piezoelectrics (PZT, $LiNbO_3$, ZnO, and quartz).[80,160] A summary of material properties of interest is presented in Table 2.3. Due to its good chemical stability and compatibility with CMOS technologies, AlN is well-suited for integration of MEMS devices into silicon-based electronics.

Silver (Ag)

Silver has a face-centered cubic (FCC) crystal structure and a lattice parameter of 4.086 Å. It has a high thermal conductivity at 300 K, low electrical resistivity, and a thermal expansion coefficient of 18.9 × 10^{6}/K.[153] Figure 2.6 – 2.7 also illustrates that Ag under certain conditions is also prone to oxidation and secondary phase formation.

2.7. Proposal

Working on the hypothesis that buried conducting layers can both mitigate the delamination problem and generate sufficient electric field to engage the operation of resonator devices, I have undertaken a study of silver ion implantation to experimentally assess feasibility. My goal is to understand the interfacial phenomena at the metal/ceramic interfaces in a model system in order to enhance the efficiency of NEMS-based energy scavenging devices. The model system used here is Ag in AlN, for reasons described in §2.6, with results applicable to other metal/ piezoelectric systems used as actuators,[50,56] resonators,[50,140] "electronic noses,"[95] bulk acoustic wave sensors[54,162] and other MEMS devices.[50,121,163] The lack of information addressing the microstructure of the metal/oxide interface and its relation to the performance of SAWs motivates the current research.

2.8. Tables for Chapter 2

Table 2.1. Selected list of piezoelectric materials.[50,51,58,139,153,160,163]

Properties / *Material*	*d (pC/N)*	*k (%)*	*Applications*	*References*
Aluminum Nitride (AlN)	5.4	3	Transducers, Optoelectronics	[139]
Barium titanate ($BaTiO_3$)	190	0.49	Accelerometer, Thermistor	[50], [58]
Lead Zirconate Titanate ($PbTi_{1-x}Zr_xO_3$) (PZT)	289	0.72	Microphones, Transducer	[50]
Lithium Niobate ($LiNbO_3$)	6	2.3	Sensor, Optoelectronics	[50]
Quartz (SiO_2)	2.3	0.1	Ultrasonic Transducers, Filters	[50]
Rochelle Salt ($NaKC_4H_4O_6{\bullet}4H_2O$)	2300	0.78		[153]
Zinc Oxide (ZnO)	12.4	2.9	Ultrasonic Transducer	[50], [139]

Table 2.2. Material properties of piezoelectric materials.[51,68,80,131,139,153,160-167]

Material / *Properties*	*GaN*	*PCL*	*ZnO*	*AlN*	*References*
Young's Modulus (10^{11} N/m^2)	N/A	150	2.11	3.94	[68],[153],[162]
Thermal Conductivity (W/m·K)	130	N/A	60	320	[131],[157],[161]
Thermal Expansion in *a* (10^{-6}/K)	5.6	30	2.9	4.2	[68],[131],[153]
Dielectric Constant (F/m)	9.5	2.8	11	8.2 – 8.9	[131], [139]
Longitudinal Acoustic Velocity (m/s)	N/A	N/A	6300	~11000	[157], [164]
Piezoelectric Coefficient (10^{-12} C/N)	N/A	N/A	12.4	5.4	[139], [163]
Piezoelectric Coupling Coefficient (%)	N/A	N/A	7.5	6.5	[80], [162]
CMOS Compatibility	Yes	No	Ok	Yes	

Table 2.3. Material properties of AlN. [63,80,131,139,153,157,160-166,168]

Property	*Symbol*	*Value*	*References*
Density (kg/m^3)	ρ	3260	[153], [163]
Melting Temperature (^{o}C)	T_m	>2200	[139], [157]
Young's Modulus (bulk) (GPa)	E	315	[139]
Young's Modulus (10^{11} N/m^2)	E	3.94	[162]
Band Gap (eV)	E_g	6.2	[153], [157]
Electrical Resistivity (Ω·cm)	ρ_e	10^{13}	[157]
Thermal Expansion Coefficient (10^6/K) (in *a*-, in *c*-)	α_T	4.2, 5.3	[131]
Thermal conductivity (W/m·K)	σ_T	180 – 320	[131]
Temperature Coefficient of Frequency (longitudinal) (ppm/^{o}C)	TCF	–25	[161]
Acoustic Wave Velocity (longitudinal) (m/s)	v_l	~11000	[80], [161]
Acoustic Wave Velocity (shear) (m/s)	v_s	~5600	[163]
Electromechanical Coupling Coefficient	k^2	6.5	[80], [161]

2.9. Figures for Chapter 2

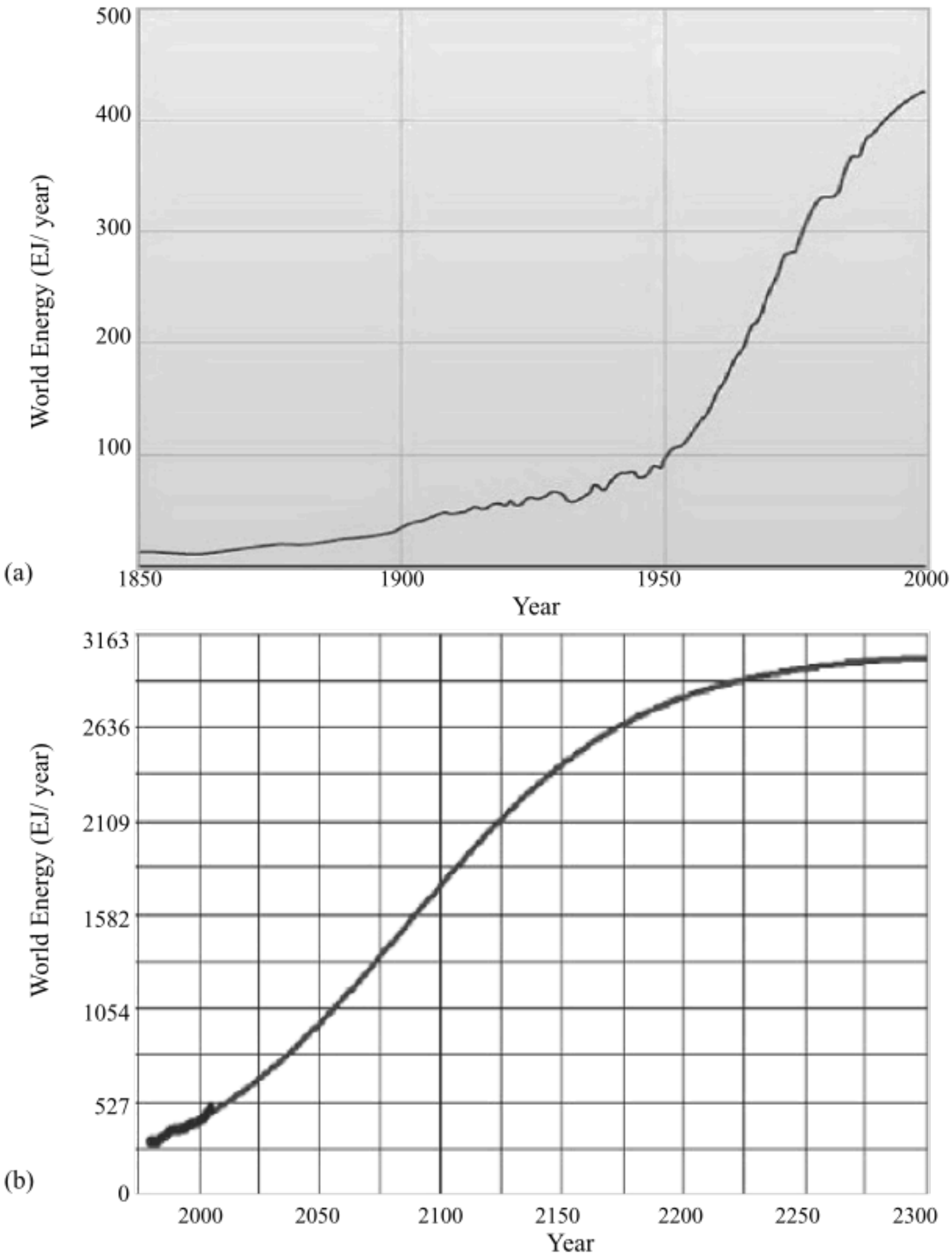

Figure 2.1. The global energy consumption as (a) calculated from 1850 to 2000 and (b) projected for 2020 to 2300. The projections were calculated based on previous usage trends as illustrated in (a).[169]

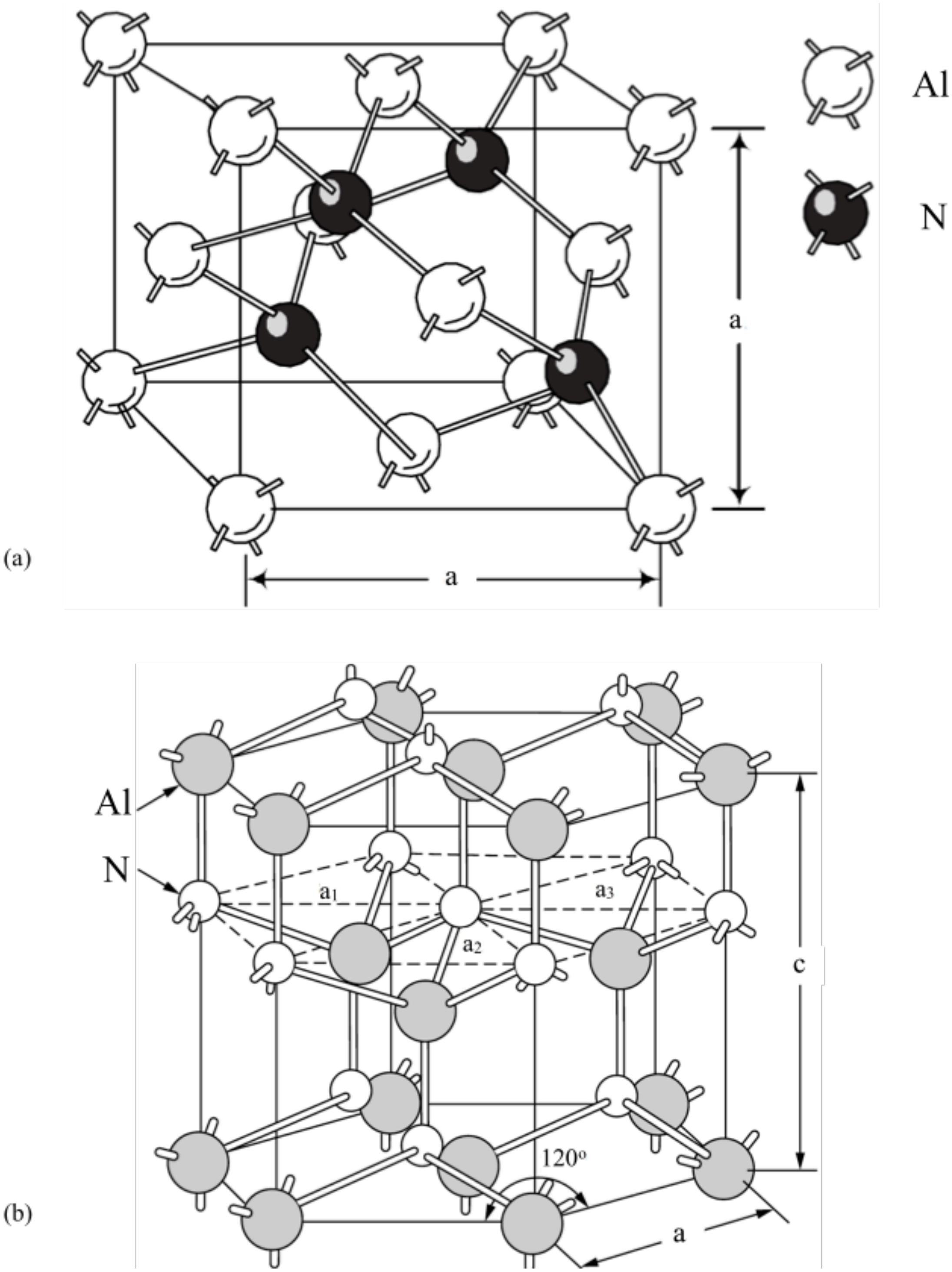

Figure 2.2. The crystal structure of AlN in (a) zinc-blende and (b) wurtzite forms.[170]

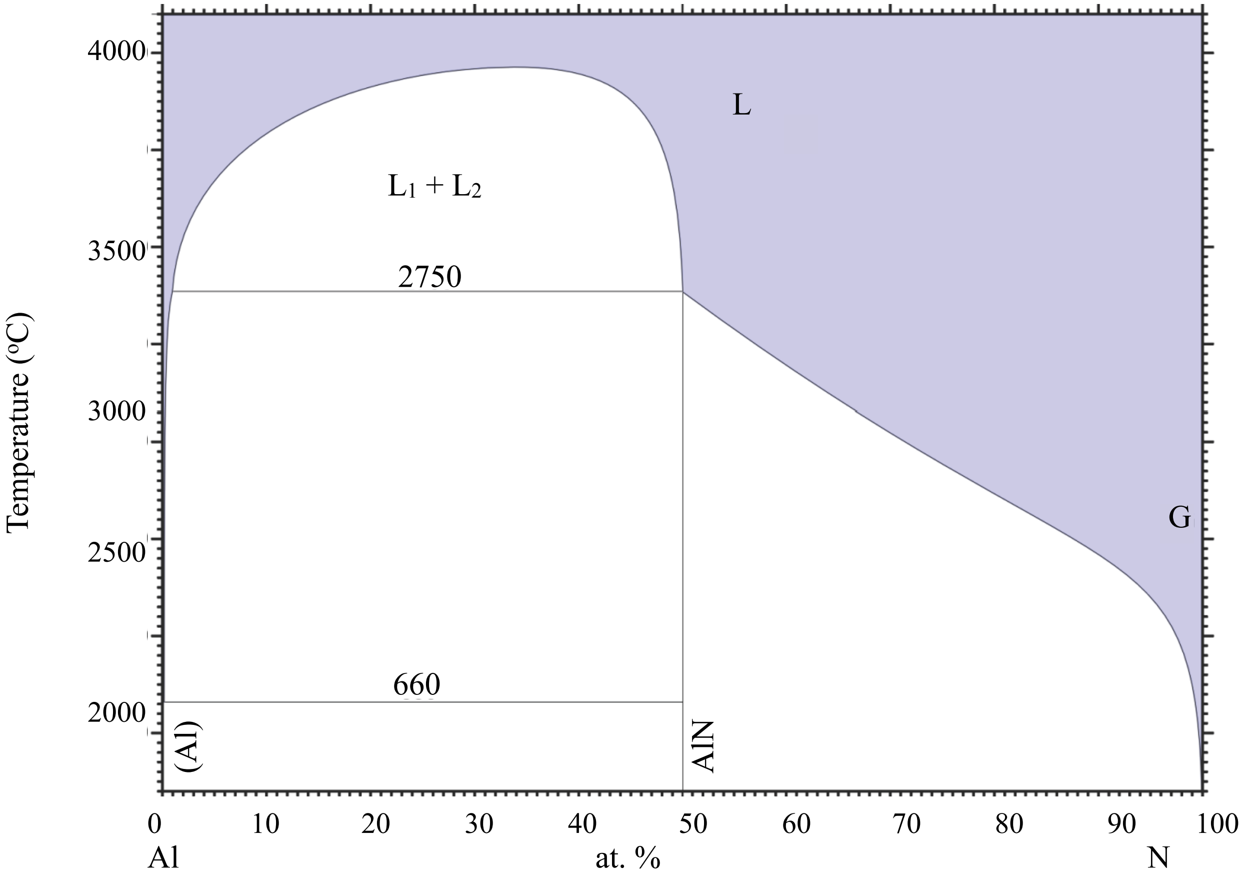

Figure 2.3. Binary phase diagram for Al-N.[171] Reprinted with permission of ASM International. All rights reserved. www.asminternational.org

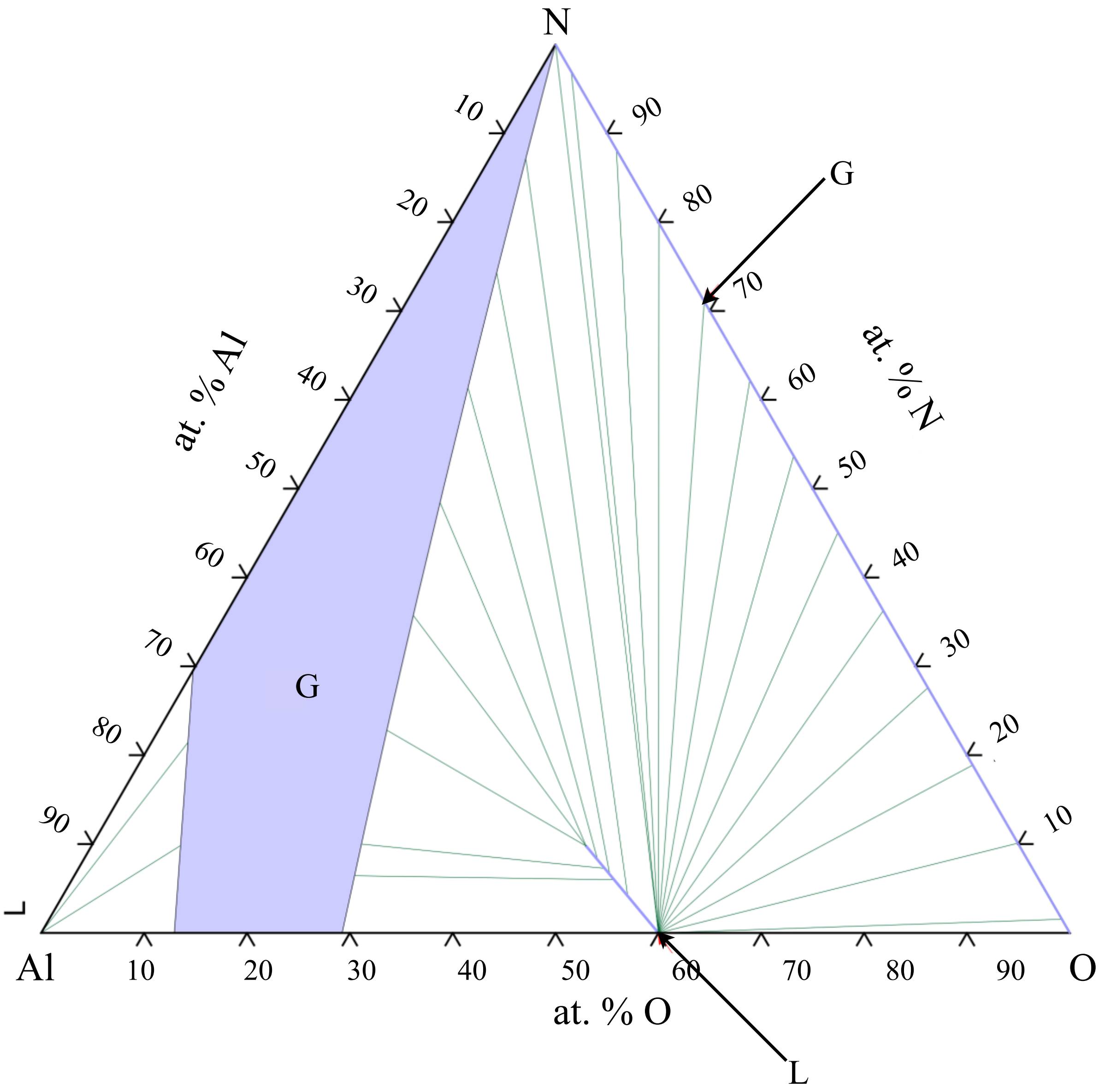

Figure 2.4. Ternary phase diagram for Al-N-O at 2450°C (2723 K).[172] Reprinted with permission of ASM International. All rights reserved. www.asminternational.org

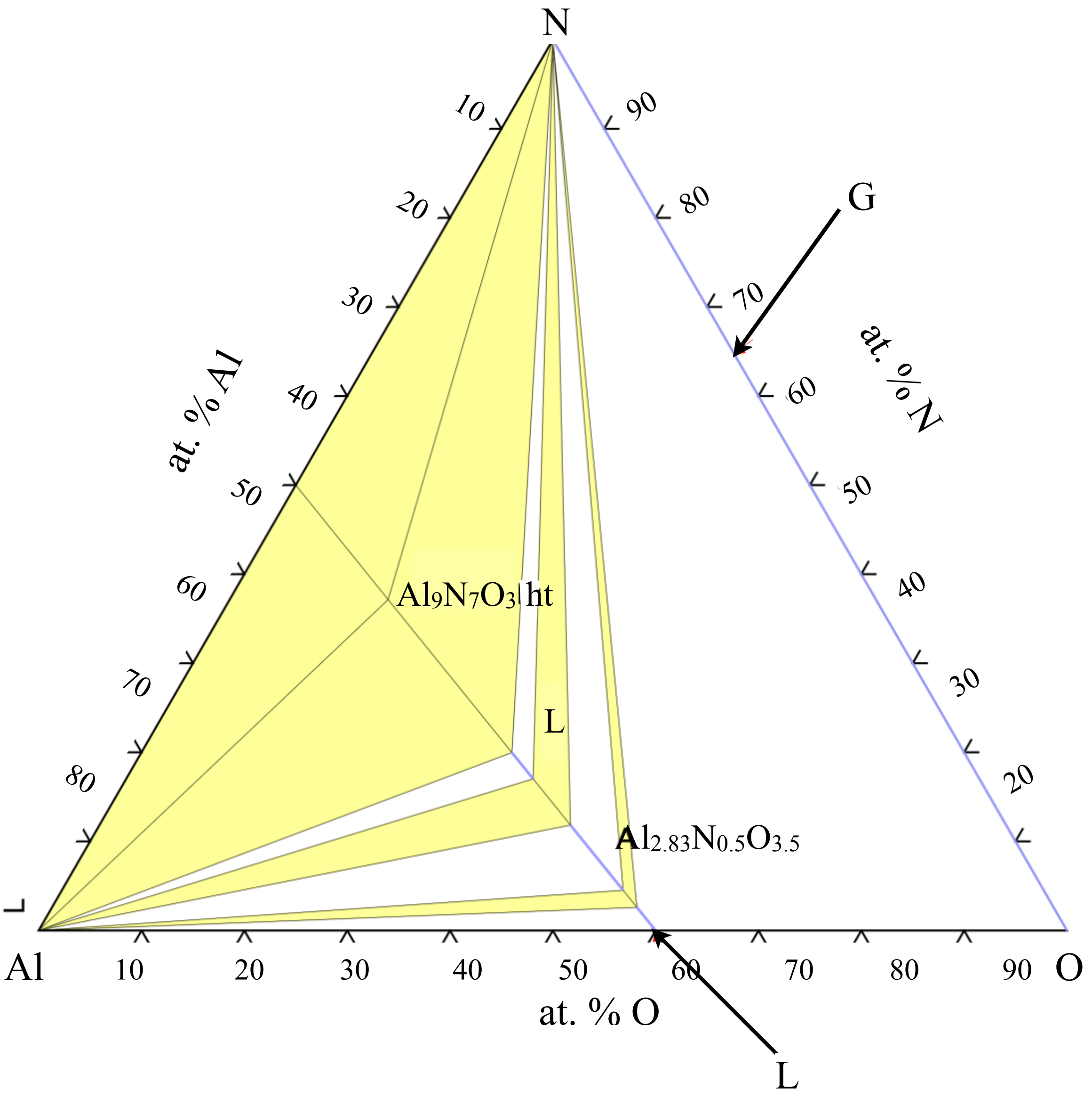

Figure 2.5. Ternary phase diagram for Al-N-O at 2100°C (2373 K).[172] Reprinted with permission of ASM International. All rights reserved. www.asminternational.org

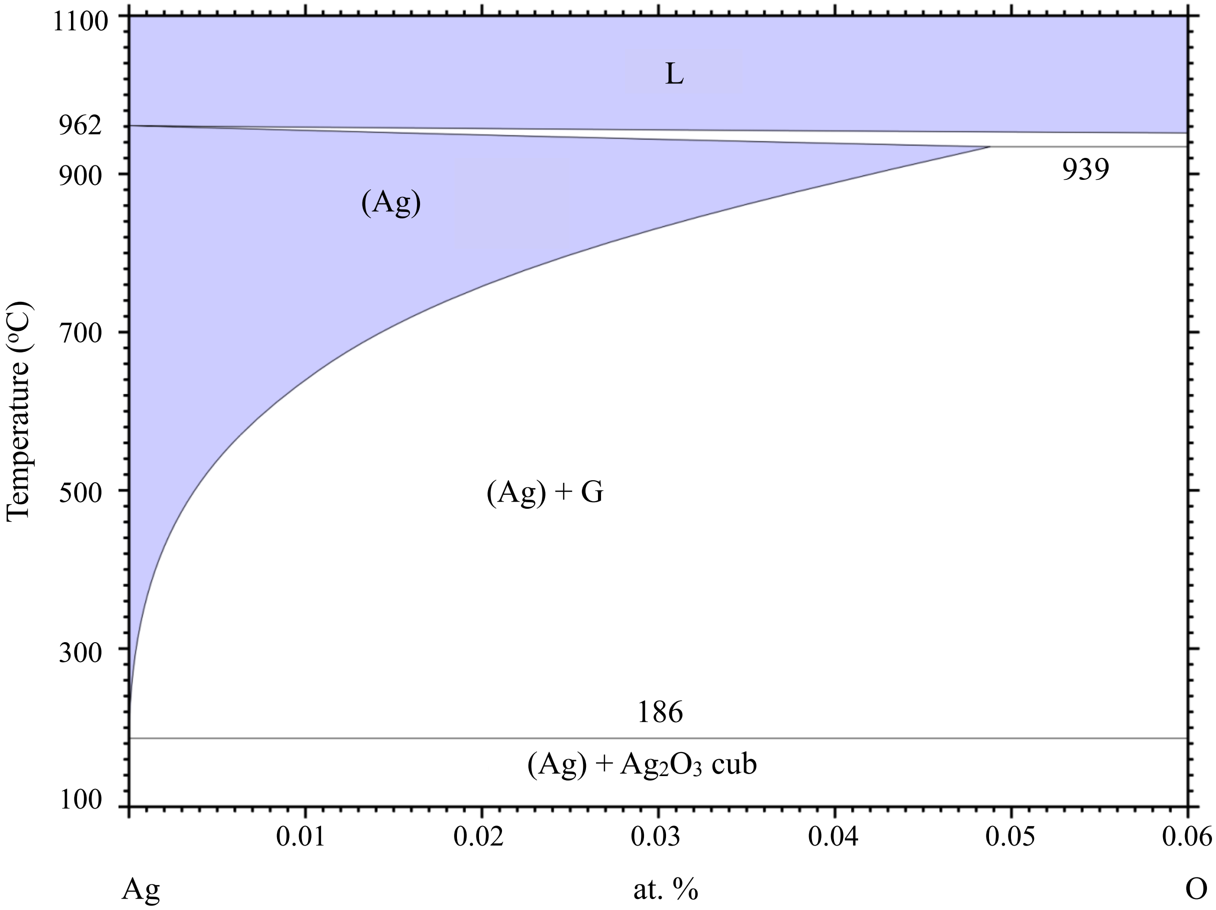

Figure 2.6. Binary phase diagram for Ag-O.[173] Reprinted with permission of ASM International. All rights reserved. www.asminternational.org

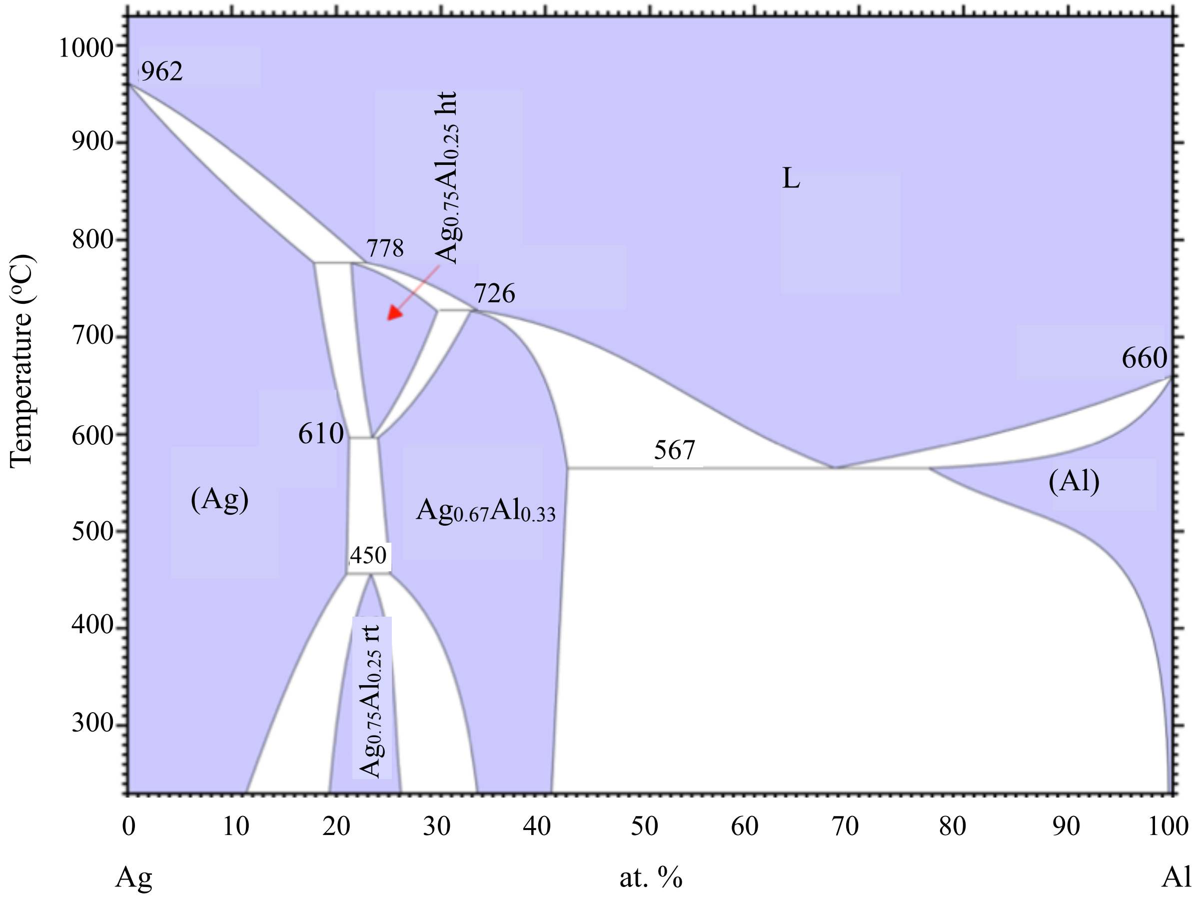

Figure 2.7. Binary phase diagram for Ag-Al.[174] Reprinted with permission of ASM International. All rights reserved. www.asminternational.org

CHAPTER 3. EXPERIMENTAL PROCEDURES

3.1 Sputtering of AlN Thin Films

For this research, *c*-axis oriented aluminum nitride (AlN) thin films were grown on Si substrates using alternating current (ac) reactive magnetron sputtering and characterized. Commercially available 0.525-µ thick Si (100) wafers (El Cat Inc.) were used as substrates. Prior to deposition, the substrates were pre-treated using the standard wafer cleaning process: Piranha solution immersion for 5 to 10 minutes, deionized water (DI) rinse for at least 1 minute, and diluted hydrofluoric acid (HF) dip for 5 to 15 seconds. The deposition process was performed using the Endeavor AT Radial Multi-chamber Dual Ring Sputtering System (OEM, formerly Tegal) housed in the Marvell Nanofabrication Laboratory at the University of California, Berkeley. The detailed process recipe is listed below:

I. Pre-deposition wafer treatment with a capacitively coupled planar rf plasma etch source at an etch rate range of 5 – 50 nm/min and rf power range of 30 – 600 W,
II. Ambient temperature of 300 – 350^{o}C, without any external heating
III. Maximum equilibrium wafer temperatures of 250^{o}C, and
IV. S-Gun magnetron powered with a cathode power of 5.5 kW at a rate of 60 nm/min.

This process yielded thin films with an AlN thickness of approximately 900 nm and a crystal orientation of (0001) normal to the wafer plane. Additional information on sputtering is provided in Appendix 1.

3.2 Ion Implantation of AlN by Ag^{2+}

The AlN/Si substrate samples were implanted, with the assistance of Dr. Andre Anders, using the 200 keV Metal Vapor Vacuum Arc (MEVVA) Implanter at the Lawrence Berkeley National Laboratory (LBNL). Two sample sets were implanted using the processes highlighted.

Sample Set A: Implantation energy of 100 keV.
Sample Set B: Initial implantation energy of 100 keV and final implantation energy of 30 keV.

Implantation energies were selected based on TRIM and TRIDYN simulations that illustrated that a 100 keV implantation of Ag in AlN is expected to result in a peak Ag concentration of 85 nm and 38 nm below the AlN surface, respectively. A dose of 1×10^{16} ions/cm^2 was selected because it would likely result in a high concentration of Ag precipitates near the surface.

The initial attempt at implantation, Sample Set A, resulted in a dose of 1×10^{16} ions/cm^2. Sample Set B resulted in a dose of 2.68×10^{16} ions/cm^2. All substrates were implanted at an angle 7^{o} normal to the substrate to prevent channeling. These implantation procedures will be referred to as Implantation 1 for the remainder of the text.

Based on preliminary data obtained from Implantation 1, an additional sample set was fabricated using a 400 keV Varian 350D Implanter at Cutting Edge Ions, Inc. Samples were implanted with an implantation energy of 100 keV at an angle of 7^{o} from the normal to prevent channeling. A dose of 1.0×10^{16} Ag^{++}/cm^2 was achieved. This implantation procedure will be referred to as Implantation 2 in the remainder of the text. Background information on ion implantation can be found in Appendix 1.

3.3 Computer Simulations of Ion Implantation

Computer simulation programs such as TRIM[47] and TRIDYN[49] were employed to predict the depth profile of Ag ions implanted in AlN. The input parameters utilized to model this behavior consisted of the following: Ag ion at an extraction voltage of 50 kV (due to an average charge state of 2.1 as reported by Yushkov, Anders, Oks and Brown[175]), AlN target layer consisting of 0.5:0.5 Al to N ratio with a layer width of 3×10^3 Å and density of 3.26 g/cm^3, and incidence angle of 7^o. It is important to note that the actual thickness of the AlN layer ranged from 800 – 900 nm and the layer width value utilized in the simulation was chosen because Ag was confined to the first ~150 nm. Simulations were performed using the static and "dynamic" simulation models. During this "dynamic" process the beam conditions were modified after a certain number of ion trajectories to account for the variations in beam energy: 50, 100, and 150 keV. Results acquired *via* TRIDYN were obtained under the following beam proportions: 20% Ag^+ beam at 50 keV, 60% Ag^{++} beam at 100 keV, and 20% Ag^{+++} beam at 150 keV. These findings, in addition to the experimental results, are presented in §4.

The AlN stoichiometry for Ag-implanted AlN substrates was confirmed using a simulation program called SIMNRA.[176,177] This program was utilized to simulate the backscattering spectra for ion beam analysis and employed under the following conditions: scattering angle of 168^o, incident angle of 55^o, incident ion of ^{4}He, energy of 3.044 MeV, energy per channel of 2.95 keV/ ch, calibration offset of –14 keV, particles * sr value of 3.82×10^{11} and target thickness of 8200×10^{15} atoms/cm^2. The target composition varied from 40 wt % Al to 70 wt % Al. A comparative analysis of these findings with respect to the experimental data is presented in §5 to test composition hypothesis. Details on TRIM and TRIDYN simulations can be found in Appendix 1.

3.4 Post-Implantation Annealing

Post-implantation thermal annealing was undertaken to induce precipitation and re-crystallization of the amorphized AlN, as a result of implantation. Annealing was conducted *via* a TyStar 4 Atmospheric Dry/Wet Oxidation furnace housed in the Marvell Nanofabrication Laboratory at the University of California, Berkeley. For Implantation 1 annealing was performed under different experimental conditions: 550^{o}C for 8 hours, 800^{o}C for 5 hours, and 1050^{o}C for 3 hours. The different annealing conditions were selected based on the material with the lowest melting temperature (T_m) and conditions necessary to promote re-crystallization of AlN and allow morphological equilibration of Ag precipitates/ Ag film in experimentally accessible times. Based on data obtained for Implantation 1, Implantation 2 was annealed at 800, 600 and 400^{o}C, all at times of 1, 5 and 10 hours. Samples were then characterized for chemical composition, structure, phase identification and orientation *via* RBS, x-ray diffraction, rocking curve, scanning electron microscopy and transmission electron microscopy.

3.5 Rutherford Backscattering Spectrometry (RBS)

The dose and depth distribution of Ag in AlN were characterized for all samples; implanted (no annealing), and implanted and annealed samples, *via* RBS. Rutherford Backscattering Spectrometry was conducted by Dr. Kin-Man-Yu using a 3 MeV alpha particle beam generated by a 5SDH Pelletron tandem accelerator (National Electrostatics Corporation (NEC)) with a terminal voltage of 1.7MV. The Silicon surface barrier detector was positioned at 168^o with respect to the incident beam. Measurements were carried out on implanted samples to evaluate any structural modifications as a result of treatment. Additional information on RBS can be found in Appendix 1.

3.6 X-ray Diffraction (XRD)

The crystalline structure was determined by using a Siemens D5000 X-Ray Diffractometer housed in the Marvell Nanofabrication Laboratory at the University of California, Berkeley. Measurements were conducted on untreated and treated samples to identify phases that developed during the implantation and annealing processes. Scans were carried out under the following conditions: generating voltage of 40 kV, tube current of 30 mA, 2θ range of 20 to 80^o, step size of 0.005^o and 0.1 s per step. The respective Si, Ag, and AlN peaks were indexed. The peak(s) of particular interest was the 0002 peak of AlN that has a 2θ value of 36.1^o.

Rocking curve measurements were achieved using a Siemens D5000 X-Ray Diffractometer housed in the Marvell Nanofabrication Laboratory at the University of California, Berkeley. Rocking curve measurements were collected at a voltage of 40 kV, tube current of 30 mA, and scanned through a θ range of 13 to 23^o, step size of 0.005^o and 0.2 s per step. The respective AlN peaks were indexed and the full-width half-maximum (FWHM) values were computed. The peak of particular interest was the 0002 peak of AlN, which has a θ value of 18.05^o. Additional information on XRD and Rocking Cruve are provided in Appendix 1.

3.7 Scanning Electron Microscopy

Scanning electron microscopy was conducted on pre-implantation samples using the ZEISS 1550 Scanning Electron Microscope (SEM) housed in the Marvell Nanofabrication Laboratory at the University of California, Berkeley. Images were collected at an energy of 5 keV. The AlN epilayer and Si substrate are labeled as marked.

3.8 Transmission Electron Microscopy

Transmission electron microscopy cross-sectional sample preparation was performed at the University of California, Berkeley. Cross-sectional electron transparent foils were prepared from unimplanted as well as both annealed and unannealed implanted samples. The process employed is an adapted version of the process highlighted by Sinclair and Bravmann in their 1984 publication.[178]

Prior to bonding, all slabs were cleaned and degreased by ultrasonically scrubbing in acetone. The implanted side of the substrate was bonded to the implanted side of a second substrate using M-bond 610 adhesive (Ted Pella®). The composite was placed in a vice and transferred to a hot plate, heated to a temperature of approximately 100^{o}C. The composite was allowed to set under pressure undisturbed for 2 hours and then allowed to cool. The two supporting Si substrates (El Cat, Inc.®), each 1 mm thick, were bonded, polished side facing the center, to both ends of the implanted substrates to prepare at least a 3-mm thick cross-section. The final composite was again placed in a vice and transferred to a hot plate, heated to 100^{o}C, for 2 hours. Figure 3.1 is an illustration of the composite.

The composite was then mounted in a vice and cut to 10 × 3 mm (L × W) rectangular slabs. Resultant slabs were then cut to achieve sample slices of approximately 250 – 300 μm (0.25 – 0.3 mm) in thickness. All cuts were performed perpendicular to the adhesive line using an Accutom® 50 high-speed saw with a diamond blade.

Each 300-μm thick slice was mounted on a metal slide using Crystalbond™ 509 mounting adhesive (Ted Pella®) and cut into a series of 3 mm discs using an Ultrasonic Disk Cutter (Fischione). Figure 3.2 is an illustration of the 3 mm discs. These discs were then manually removed from the metal slide, rinsed in acetone, and remounted on platens (again using Crystalbond™ 509). The discs were then polished using a specimen grinder (Fischione) and first 2400- and then 4000-grit sandpaper (Allied High Tech Products, Inc.). They were then turned over and remounted on the platen for thinning. Thinning was performed, with minimal pressure, in the direction parallel to the orientation of the individual slabs to a thickness of 100 μm using 800-grit sandpaper with the Fischione specimen grinder.

Once a 100-μm thickness was achieved, the top surface of each disk was bonded to a 3 mm circular copper-rhodium slip with a 600-μm hole in the center (#2507, Ernest F. Fullam, Inc®) using M-bond 610 adhesive (Ted Pella®). Then, the platen was transferred to a hotplate heated to 150^{o}C, a small piece of a KIMTECH® brand Kimwipe™ was placed over each disk, a 100 g weight was placed on a glass slide and this was placed over the disk, and the platen was left to cure for 1.5 hours. After curing, the weight was removed, and the disk (with the Kimwipe still on it), was placed in acetone. The Kimwipe was then manually separated from the disk using tweezers. Subsequently, the bottom side of the disks were polished using the method described above. Each disk was then remounted on a platen with a transparent center for dimple grinding.

Each sample was then dimpled and polished to a mirror finish using a Model 200 Dimpling Grinder (Fischione®). The sample was strategically placed so that the region of minimum thickness coincided with the faces of slabs 2 and 3, area of interest. A stainless steel dimple grinding wheel was employed to grind the sample using glycol-based polycrystalline diamond suspensions, in the following order: 6, 3 and 1 μm-grade, until a desired thickness of 10 μm was achieved. Thickness values were determined by using the Si reflectivity of light (at ~10 μm it appears red). The final, fine, polishing step was accomplished using a synthetic felt wheel and colloidal-SiO_2 polishing suspension (Buehler®) to attain a reflective surface with minimal sample removal. The final thickness of the specimen at the center of the dimple after polishing was approximately 10 μm.

After dimpling, the platen was rinsed with water and then with acetone. To release the sample, the platen was set in the fume hood in a glass beaker of acetone overnight to dissolve the

Crystalbond^{TM} adhesive. The sample was then carefully removed and rinsed successively with acetone and ethanol to remove residual slurry and adhesive and prepped for ion milling.

Ion milling was employed to thin samples to electron transparency. It was performed using a Model 1010 Ion Mill (Fischione®) operated at an initial potential of 3.5 kV with a beam current of 5 μA, an angle incidence of 8^o and a vacuum level of 5×10^{-5} Torr. The specimen was rotated at 2.5 rpm in single sector mode and rocked $\pm 60^o$ with respect to stage. The time to perforate foil varied from 2 – 10 hours, depending on the thickness of the film. Once perforation was achieved, the voltage and beam current were reduced to 1 kV and 1.5 μA, and the sample was milled for an additional 20 minutes. This final step was performed to remove specimen material on the surfaces of the foil that have been damaged during ion milling. The final product was similar to Figure 3.3 however with a nice reflective surface.

3.8.1 Conventional Transmission Electron Microscope Techniques

Conventional transmission electron microscopy imaging and diffraction was performed using a JEOL 2011 (0.23 nm resolution) transmission electron microscope (TEM) with a lanthanum hexaboride filament operated at 200 keV housed in the Hearst Mining Building at UC Berkeley. Orientation relationships of individual Ag precipitate with respect to the AlN matrix and/or confirmation of a thin film were evaluated *via* conventional two-beam and centered-beam-zone-axis bright-field (BF)/dark-field (DF) imaging and diffraction patterns from the AlN and Si in low-index zone axis orientations. Additional information on transmission electron microscopy can be found in Appendix 1.

3.8.2 TEM Data Analysis

Image J[179] was implemented to measure spacing and angular orientation of morphological features captured in conventional, bright-field images. *Web Electron Microscopy Application Software* (WebEMAPS), a free diffraction pattern indexing software application found at http://emaps.mrl.uiuc.edu, was employed to simulate diffraction patterns for comparison with experimentally captured patterns under a multitude of zone axis orientations.

3.9 Figures for Chapter 3

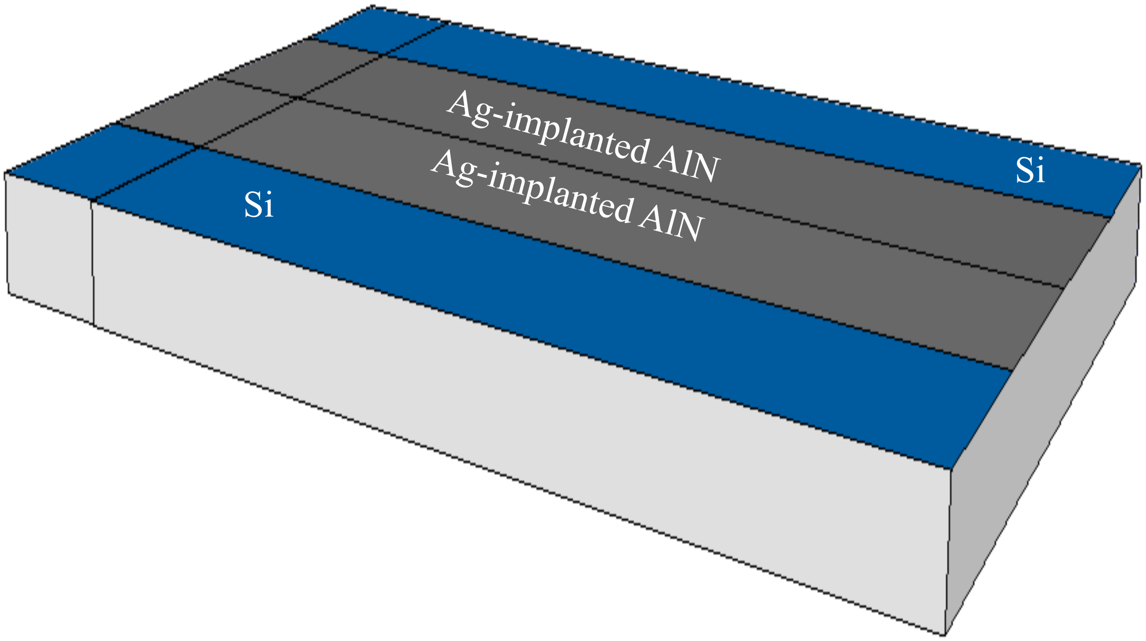

Figure 3.1. Schematic of Ag-implanted AlN and Si substrates sliced and glued into cross-sectional configuration in advance of thinning to produce TEM samples.

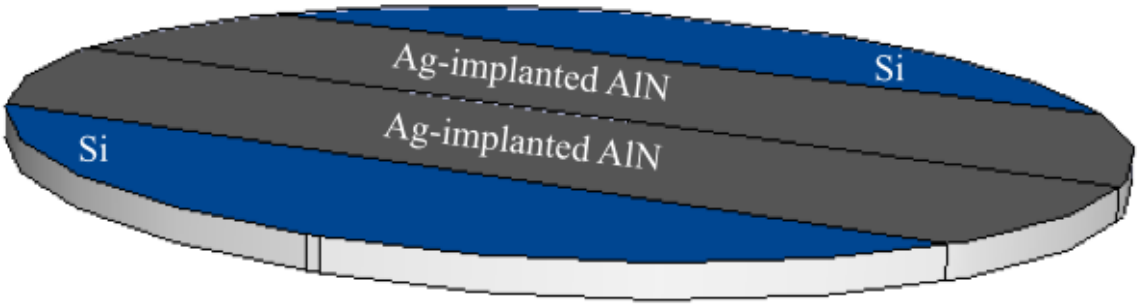

Figure 3.2. Schematic of reduced thickness cross-sectional disc cut in advance of thinning for TEM samples.

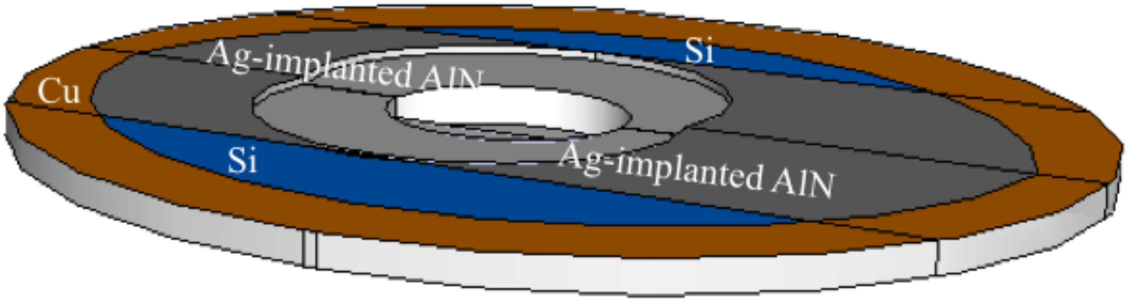

Figure 3.3. Schematic of thinned TEM sample generated by ion milling to obtain two regions of electron transparent AlN/Si interfaces in back-to-back orientations.

CHAPTER 4. RESULTS

4.1 Summary of Results

Figure 4.1 shows computer simulation results using Transport of Ions in Matter (TRIM) and TRIDYN for Ag ions implanted in AlN at RT. Calculations were performed at 100 keV and 50 keV, respectively, to determine the depth profile of Ag ions implanted at 100 keV to achieve a dose of 1.0×10^{16} cm^{-2}. For comparison, RBS data for AlN implanted with a dose of 100 keV Ag ions at room temperature to acquire a dose of 1.0×10^{16} $ions/cm^2$ are included. The results *via* TRIM and TRIDYN indicate that the peak concentration is attained at approximately 37 nm and 42 nm, respectively. Experimental RBS results indicated that a peak concentration is attained at approximately 45 nm from the surface.

The computer simulation models employed to estimate the depth profile of silver ions implanted in AlN at an energy of 100 keV and a dose of 1.0×10^{16} cm^{-2} compare well with the RBS data shown in Figure 4.1. The TRIM results indicate that the implantation of Ag into AlN at an energy of 100 keV yields a narrow implantation distribution range. The projected range, R_p, is positioned at 37 nm from the surface with a maximum silver atomic fraction of 0.043. Calculations conducted using TRIDYN were performed at 50 keV due to extended processing times required to simulate (with limited computing power and memory) at 100 keV. The results indicate that implantation at 50 keV yields a bell-shaped distribution curve ranging from 10 to 105 nm and an R_p value of 45 nm. A peak concentration of 0.018 is expected. Based on Figure 4.1, the simulation profiles conducted *via* TRIDYN at half the implantation energy,matched well with the experimental results obtained using RBS.

Figure 4.2 shows the RBS results for (0001) AlN implanted with a dose of 1.0×10^{16} Ag^{++}/cm^2. Simulations *via* SIMNRA were performed for AlN with a 1:1 and 0.6:0.4 AlN stoichiometry. For comparison, experimental results are included. Data indicate that the AlN stoichiometry matches well with the stoichiometry of 0.6:0.4 and not 1:1.

Shown in Figure 4.3 is the RBS data for (0001) AlN with a dose of 1.0×10^{16} Ag^{++}/cm^2. Data for the as-implanted and samples stored at room temperature (RT) are presented. The inset gives the Ag distribution as a function of depth from the surface of AlN. For both conditions, the peak concentration is attained at approximately 48 nm from the surface. A strong oxygen resonance peak can be observed at an energy of 1100 keV in both samples.

The concentration profiles are shown as functions of channel and energy in Figure 4.4 for (0001) AlN implanted with 1.0×10^{16} Ag^{++}/cm^2 followed by post-thermal annealing treatments at (a) 600, (b) 800 and (c) 1000^{o}C for 5 hours. Peaks are positioned at channel values of approximately 880, 570, 380, and 280. These peaks represent Ag, AlN, O_2 and Si, respectively. There is a significant increase in counts for the oxygen resonance peak with an increase in annealing temperature with respect to the as-implanted samples. A 26% increase in oxygen concentration is observed in samples annealed at 600 and 800^{o}C, while a significantly substantial increase of 75 % is observed in samples annealed at 1000^{o}C. The peak Ag concentration for samples as-implanted and annealed at 600 and 800^{o}C is located at 48 nm from the surface while a conspicuous shift in R_p to 40 and 60 nm from the surface can be observed in samples annealed at 1000^{o}C. There is also a noticeable decrease in silver concentration by approximately 16% in the latter samples.

The x-ray diffraction patterns in Figure 4.5 are for (0001) AlN implanted with 1.0×10^{16} Ag^{++}/cm^2 and followed by a post-thermal annealing treatment at (a) 400, (b) 600 and (c) 800^{o}C for 1, 5 and 10 hours. For brevity, XRD data for samples thermally annealed at 1000^{o}C for 1, 5 and 10 hours are not shown as no noticeable differences were identified. Prominent peaks for 0002 AlN and 004 Si are positioned at 2θ values of 36 and 69^{o} respectively. Additionally, a minor peak representing $\bar{1}01\bar{0}$ AlN is visible at approximately 33^{o}.

Figures 4.6 – 4.8 represent the rocking curve data in (a) full scan and (b) enlarged view modes for (0001) AlN implanted with 1.0×10^{16} Ag^{++}/cm^2 and post-thermally annealed at (a) 400, (b) 600 and (c) 800^{o}C for 1, 5 and 10 hours. A visible shift in the peak position closer to 18^{o}, which is half the Bragg angle of 0002 AlN, can be detected for all annealing temperatures. Additionally, changes in peak intensities can be observed in the samples annealed at higher temperatures and for longer times.

A scanning electron micrograph of (0001) AlN implanted with 1.0×10^{16} Ag^{++}/cm^2 is exhibited in Figure 4.9 under (a) low and (b) high magnification, collected at an accelerating voltage of 5 kV using a ZEISS 1550 Scanning Electron Microscope (SEM). Particular areas of interest include the mask, AlN and Si layers, as labeled in the figure. No noticeable precipitates were visible in the AlN matrix at any of the available magnifications.

Bright-field images and a diffraction pattern of (0001) AlN implanted with 1.0×10^{16} Ag^{++}/cm^2 at an energy of 100 keV are presented in Figure 4.10. The top figures, Figure 4.9 (a) and (b) show evidence of a columnar morphology, and again, there are no discernible precipitates visible in the micrograph. The respective diffraction pattern, as indexed, shows the dominant HCP AlN spots.

The same area shown in Figure 4.10 is presented at enhanced magnification in Figure 4.11 revealing additional detail but no precipitates. The diffraction pattern as indexed represents the $[2\bar{1}\bar{1}0]$ zone axis for AlN. Additional spots, not indicative of AlN, are also labeled.

Transmission electron micrographs, in bright-field mode, of (0001) AlN implanted with 1.0×10^{16} Ag^{++}/cm^2 at an energy of 100 keV and post-thermally annealed at 400^{o}C are presented in Figure 4.12 at (a) low magnification, and (b) high magnification. Mottled regions, indicative of damage, are visible at both magnifications.

A bright-field image and diffraction patterns from selected areas of the 400^{o}C thermally annealed samples are highlighted in Figure 4.13. Features of the diffraction patterns vary by location, confirming that there are structural variations across these regions of the sample.

A transmission electron micrograph and diffraction pattern of (0001) AlN implanted with 1.0×10^{16} Ag^{++}/cm^2 at an energy of 100 keV and post-thermally annealed at 550^{o}C are presented in Figure 4.14. The top figure (a) is a bright-field image taken at low magnification, and the bottom figure (b) is the respective diffraction pattern. The columnar morphology of the AlN is visible and the diffraction pattern highlights the dominant AlN matrix, as indexed.

Figure 4.15 is a higher magnification transmission electron micrograph and diffraction pattern of the same area presented in Figure 4.14. Variations in columnar width are evident. The respective diffraction pattern shows the same unexpected spots as seen in Figure 4.11.

Nanoprecipitates are found in the (0001) AlN sample implanted with 1.0 × 10^{16} Ag^{++}/cm^2 at a nominal energy of 100 keV and post-thermally annealed at 550°C, as revealed in Figure 4.16. The nanoprecipitates, varying in contrast, are randomly dispersed throughout the matrix.

A transmission electron micrograph and diffraction pattern for an isolated Ag nanoprecipitate are shown in Figure 4.17. This nanoprecipitate is located at approximately 40 nm from the surface. It is spherical in shape and approximately 70 nm in diameter.

Bright-field images and a selected area diffraction pattern of (0001) AlN implanted with 1.0 × 10^{16} Ag^{++}/cm^2 at an energy of 100 keV and subsequently annealed at 600°C are presented in Figure 4.18. Figure (a) and (b) were taken at low and high magnifications, respectively. Mottling is evident in both images. The respective diffraction pattern, presented in (c), reflects the dominant $[2\bar{1}\bar{1}0]$ zone axis of AlN.

Figure 4.19 is a higher magnification transmission electron micrograph, taken in bright-field mode, and a diffraction pattern of (0001) AlN implanted with 1.0 × 10^{16} Ag^{++}/cm^2 at an energy of 100 keV and post-thermally annealed at 600°C. No nanoprecipitates were found dispersed throughout the matrix; however, the columnar morphology of the AlN is evident.

Structural detail of the AlN/ Si interface in the samples annealed at 600°C is shown in Figure 4.20. The dark area indicates the presence of a second phase that may have developed during the AlN growth process. The respective diffraction patterns consist of additional spots, with respect to AlN, which may be consistent with this second phase. Possible origins include relrods, planar defects such as stacking faults, twinning, second-phase particles, and/or higher order Laue zone penetrations.

Figure 4.21 consists of dark-field images and a diffraction pattern from the *c*-axis oriented (0001) AlN implanted with 1.0 × 10^{16} Ag^{++}/cm^2 at an energy of 100 keV with no subsequent thermal annealing treatment. Selected reflections were used to capture the images presented. Moiré fringes from overlapping crystalline grains and contrast reversal from specifically chosen diffracted beams are visible in the patterns.

4.2 Figures for Chapter 4

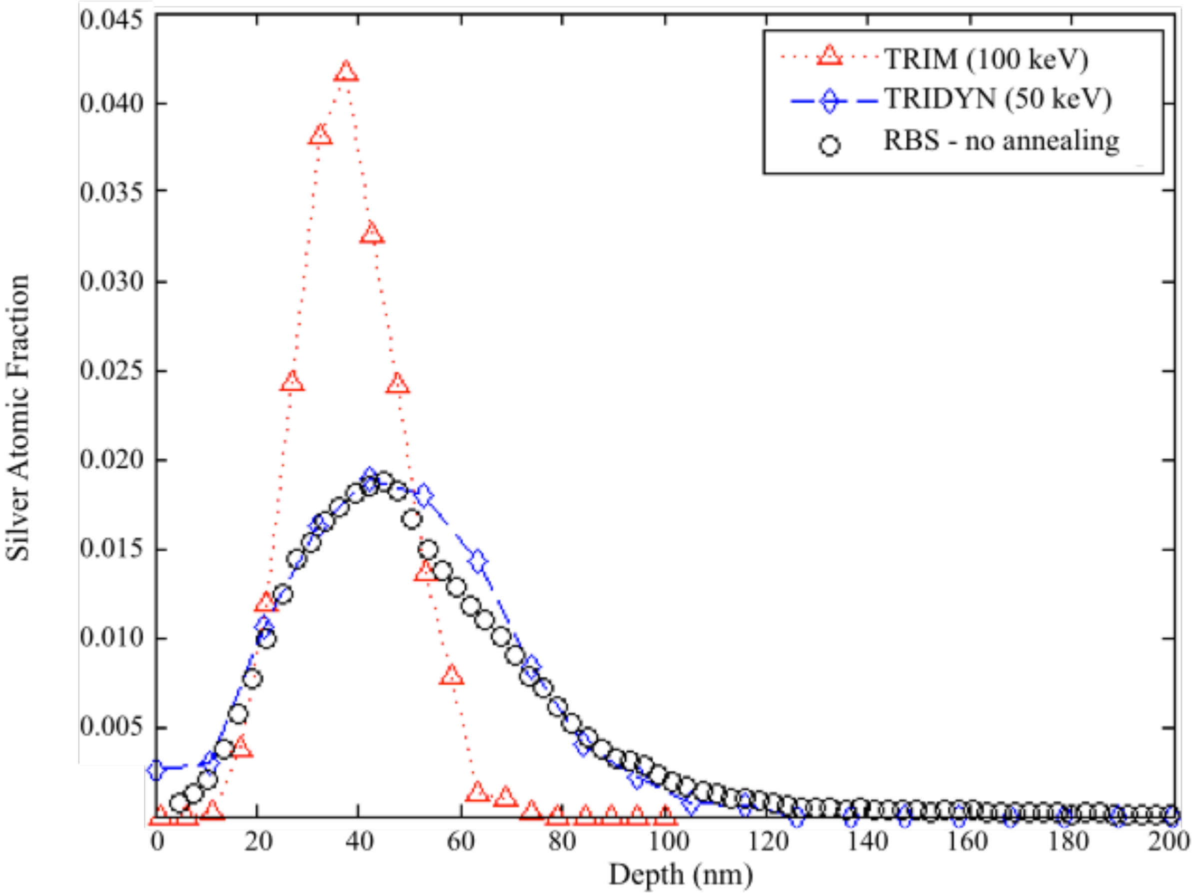

Figure 4.1. TRIM and TRIDYN simulations showing the depth profile for Ag^{++} implantation in AlN at 100 keV and 50 keV, respectively. RBS data for Ag ion implantation in (0001) AlN at a dose of 1×10^{16} cm^{-2} are also inserted for comparison.

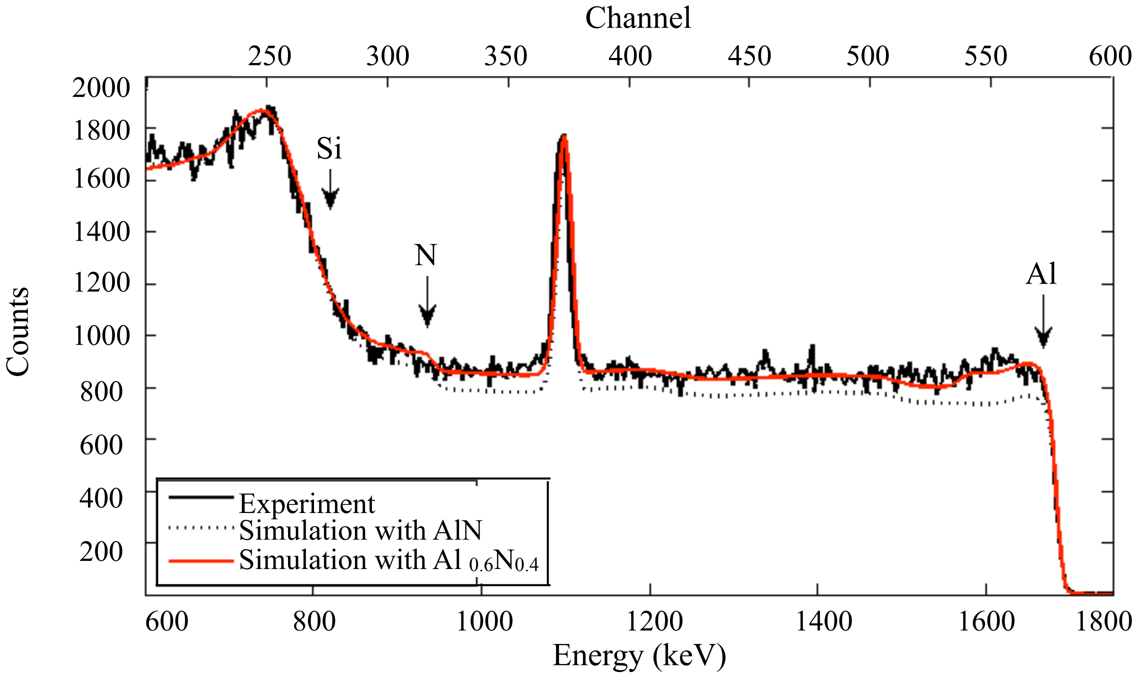

Figure 4.2. RBS results for (0001) AlN implanted with 1 × 10^{16} Ag^{++}/cm^2. SIMNRA simulations conducted at 100 keV for a 1:1 and 0.6:0.4 AlN stoichiometry are also presented.

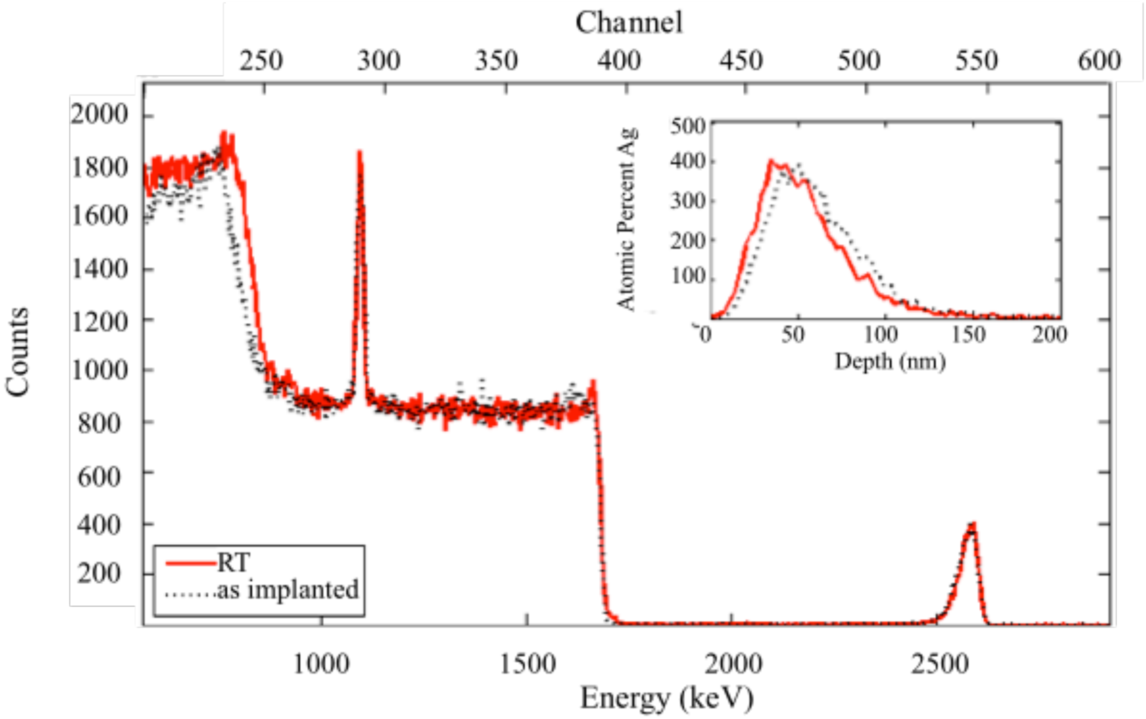

Figure 4.3. RBS for as-implanted AlN with a dose of 1 × 10^{16} Ag^{++}/cm^2. The inset gives the Ag distribution as a function of depth from the surface of AlN.

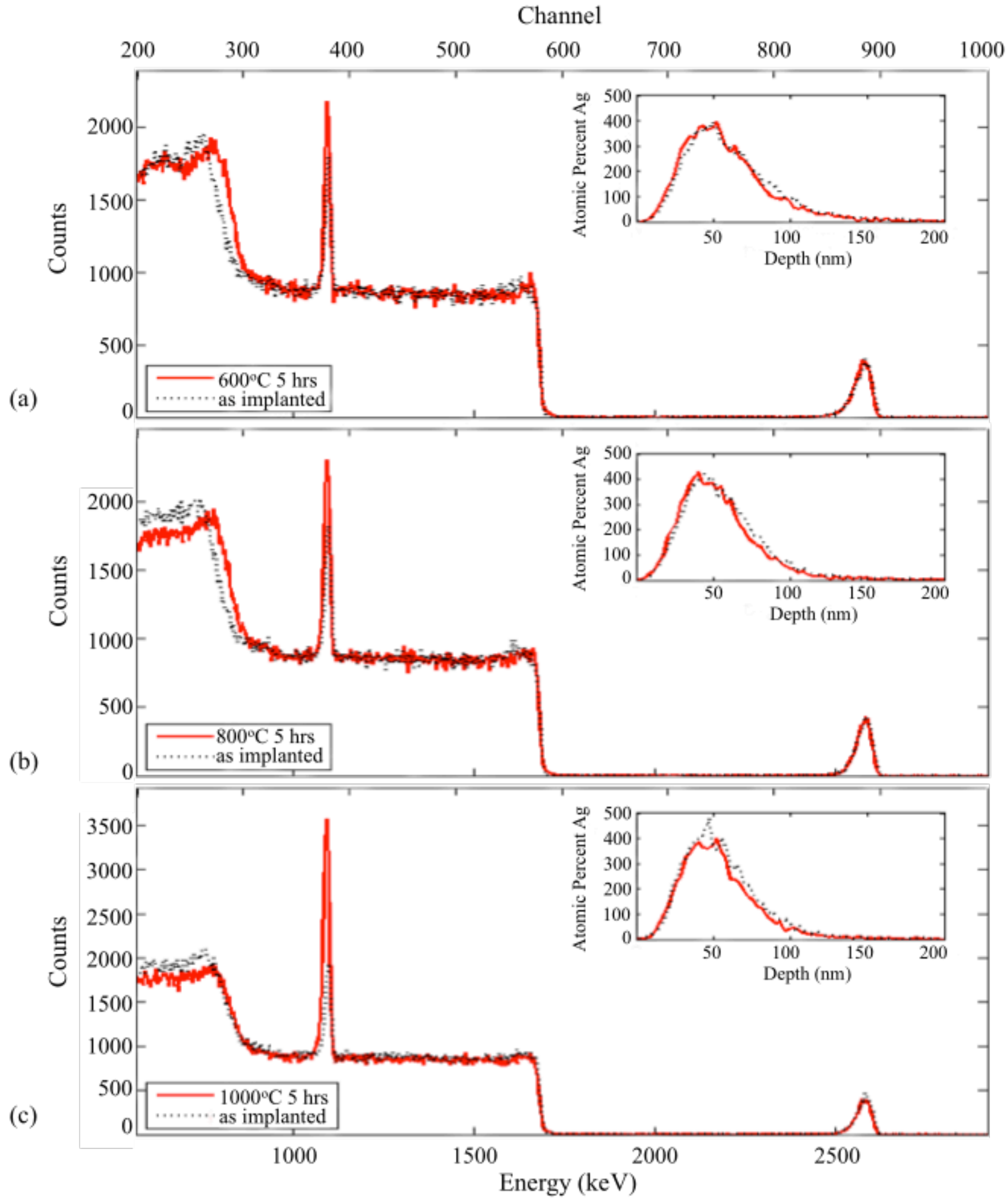

Figure 4.4. RBS spectra for (0001) AlN implanted with 1×10^{16} Ag^{++}/cm^2 followed by a post-annealing treatment at (a) 600, (b) 800, and (c) 1000^{o}C for 5 hours. The inset gives the Ag distribution as a function of depth.

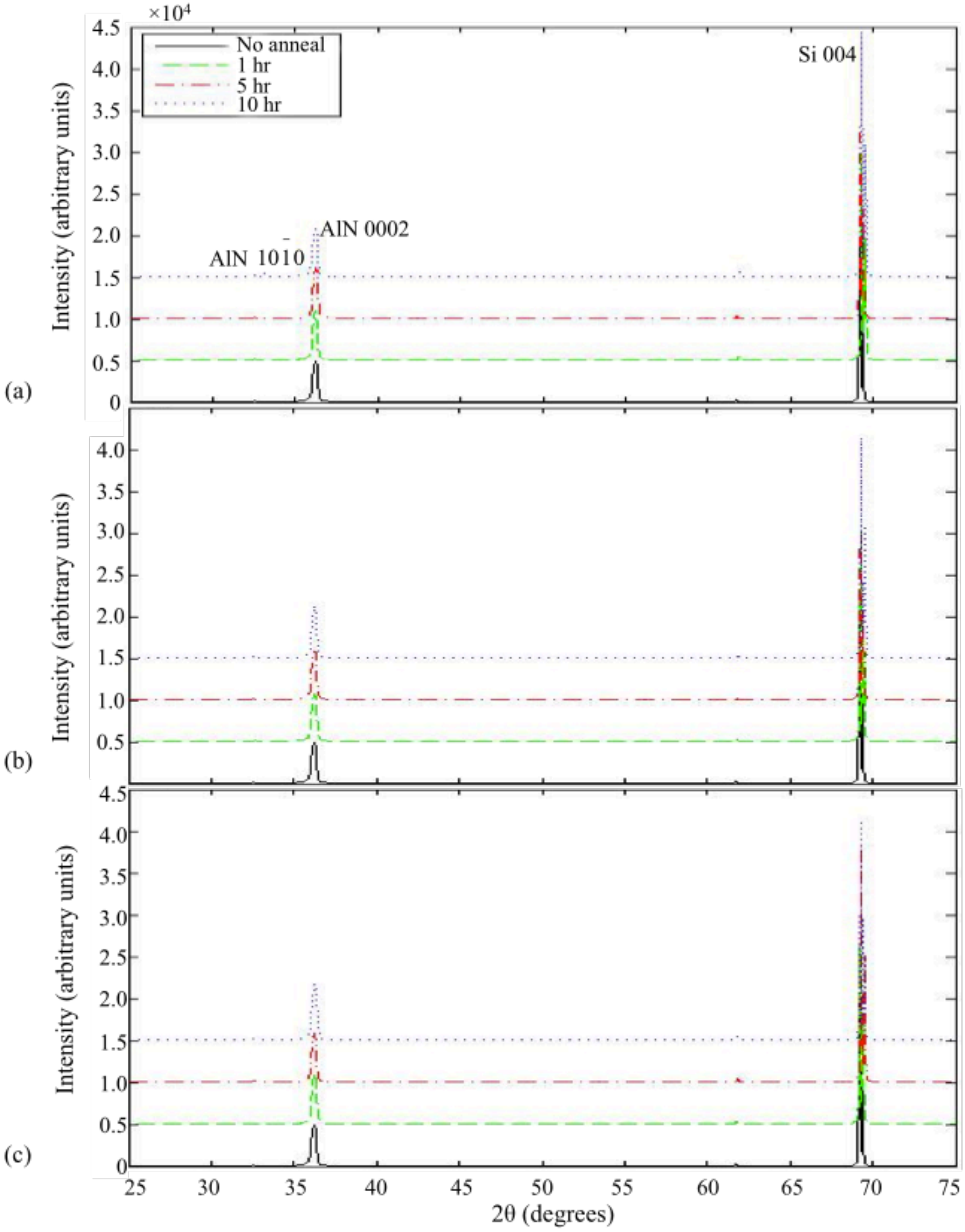

Figure 4.5. X-ray diffraction patterns of (0001) AlN ion implanted at 100 keV with a dose of 1 × 10^{16} Ag^{++}/cm^2 ions and subsequently annealed at (a) 400, (b) 600, and (c) 800^{o}C for 1, 5 and 10 hours. The as-implanted spectrum is included for comparison.

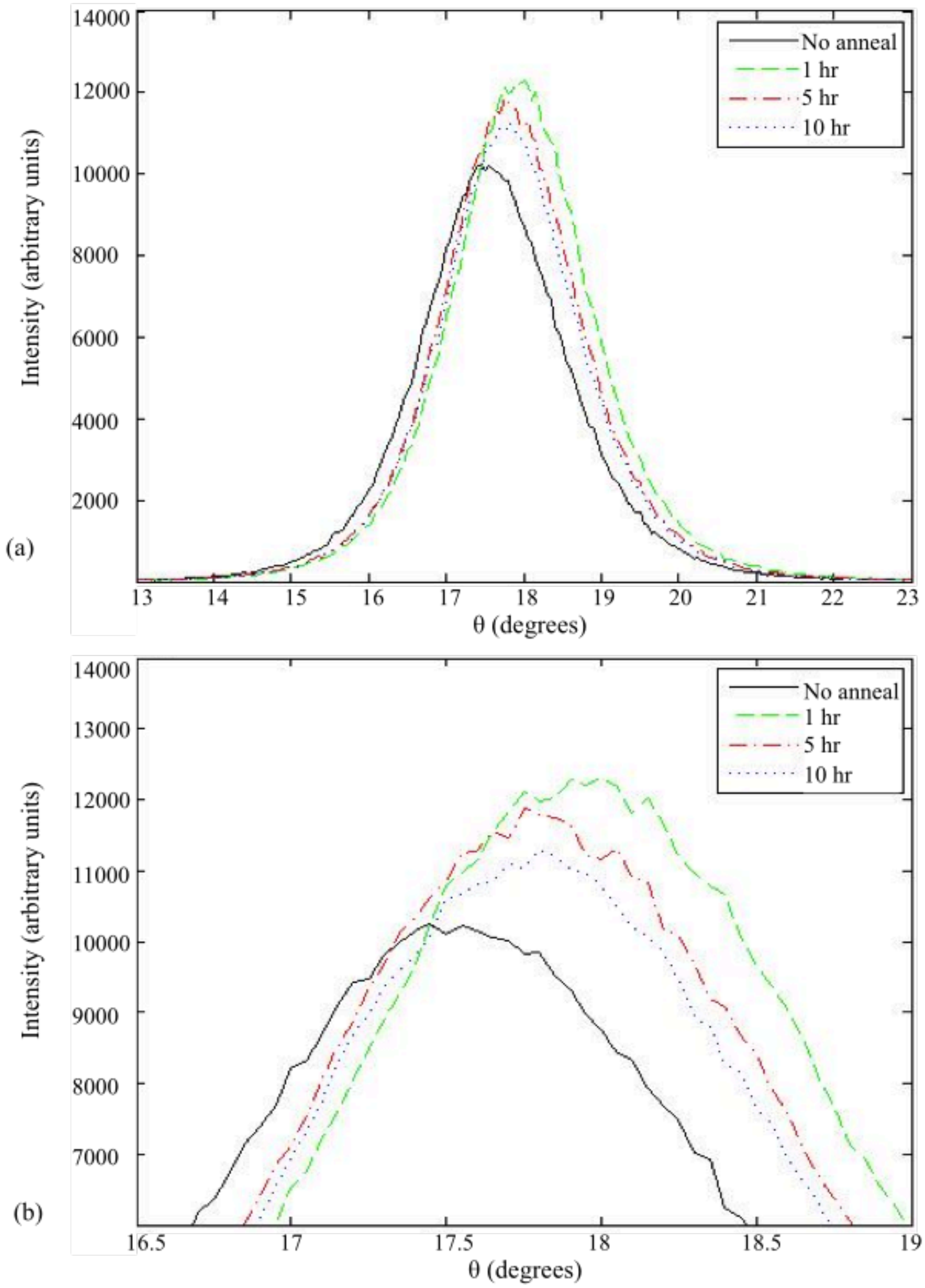

Figure 4.6. Rocking curve data of (0001) AlN implanted with a dose of 1 × 10^{16} Ag^{++}/cm^2 and annealed at 400°C for 1, 5 and 10 hours in (a) full scan and (b) enlarged views.

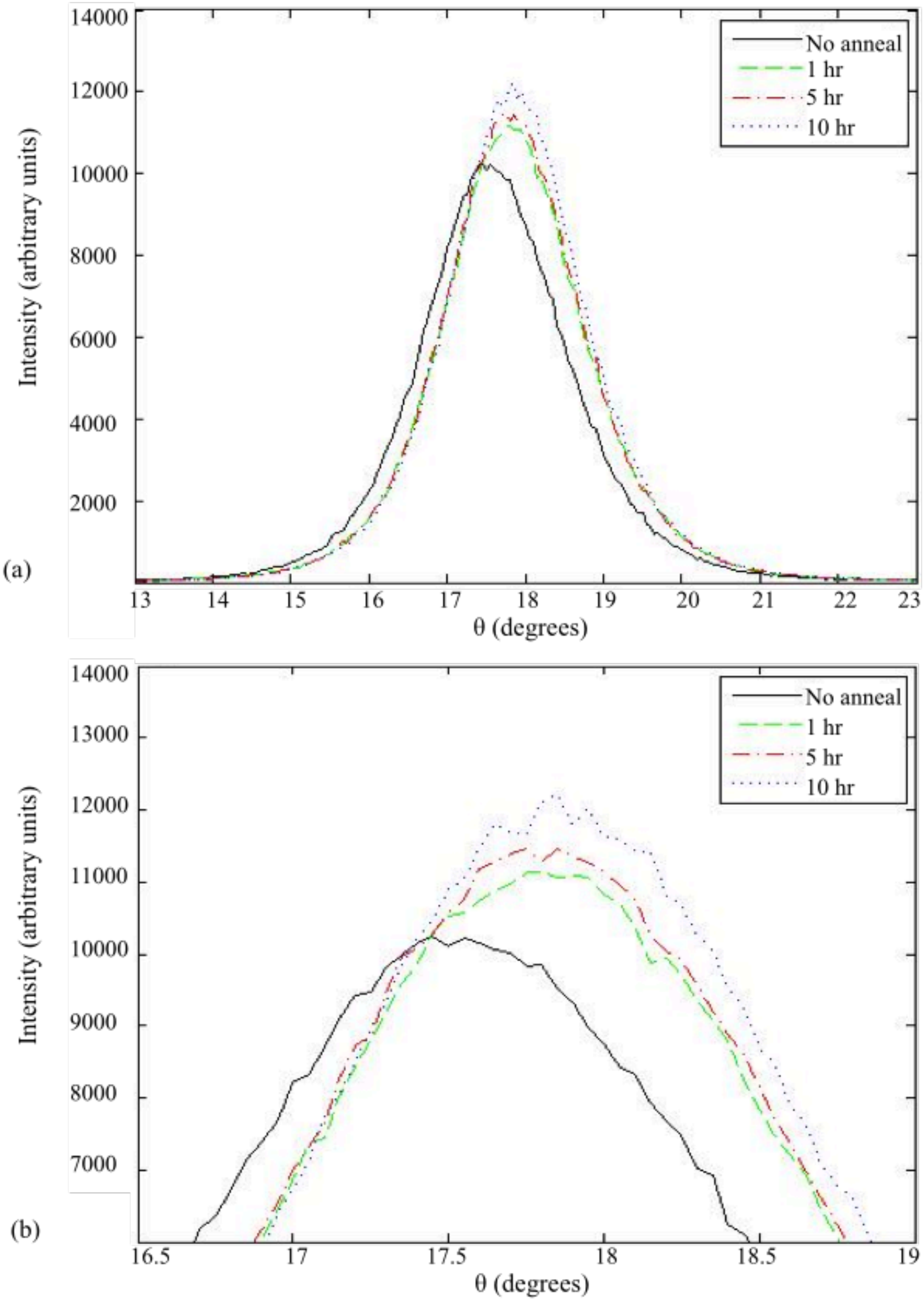

Figure 4.7. Rocking curve data of (0001) AlN implanted with a dose of 1 × 10^{16} Ag^{++}/cm^2 and annealed at 600°C for 1, 5 and 10 hours in (a) full scan and (b) enlarged views.

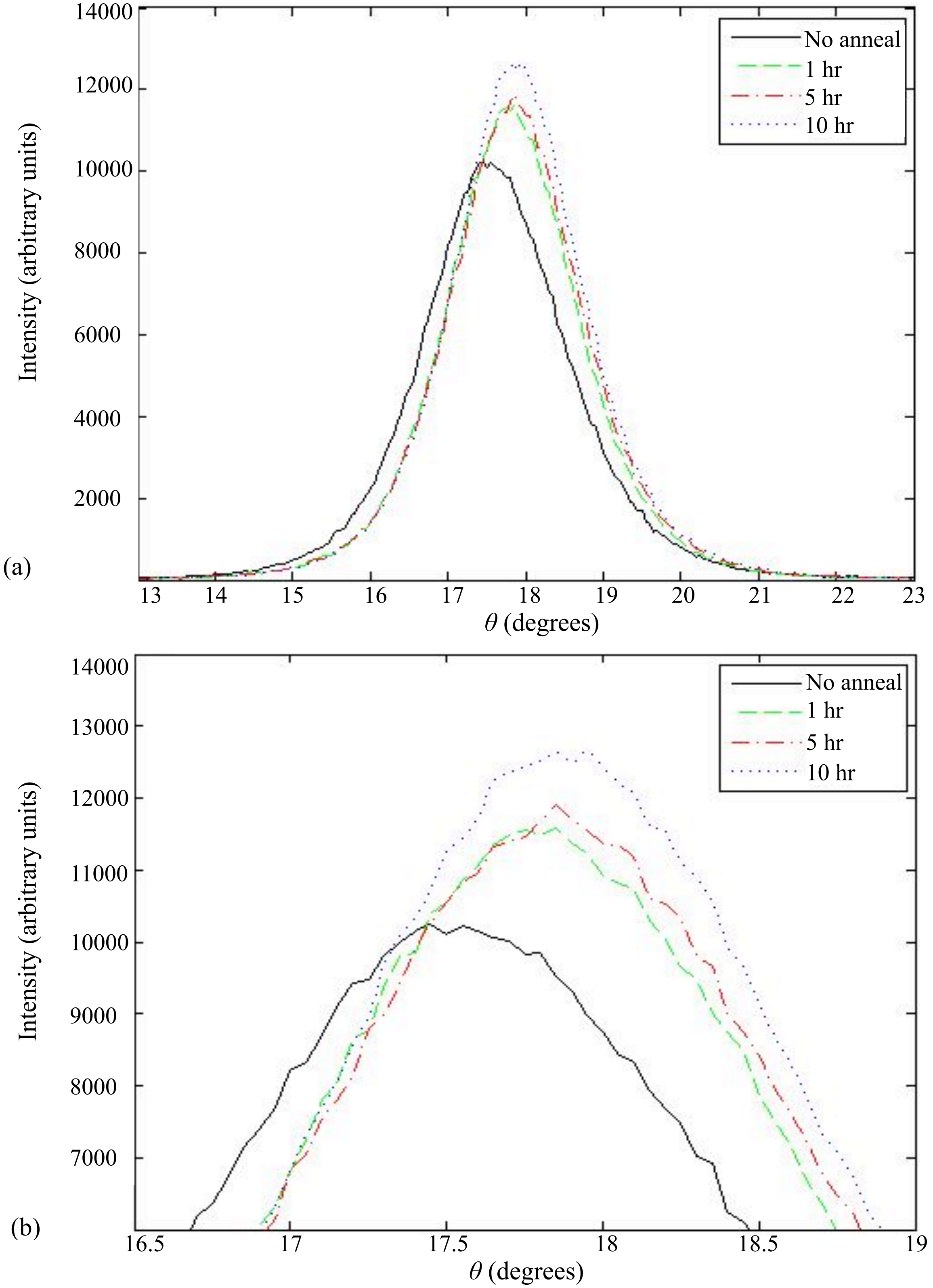

Figure 4.8. Rocking curve data of (0001) AlN implanted with a dose of 1 × 10^{16} Ag^{++}/cm^2 and annealed at 800°C for 1, 5 and 10 hours in (a) full scan and (b) enlarged views.

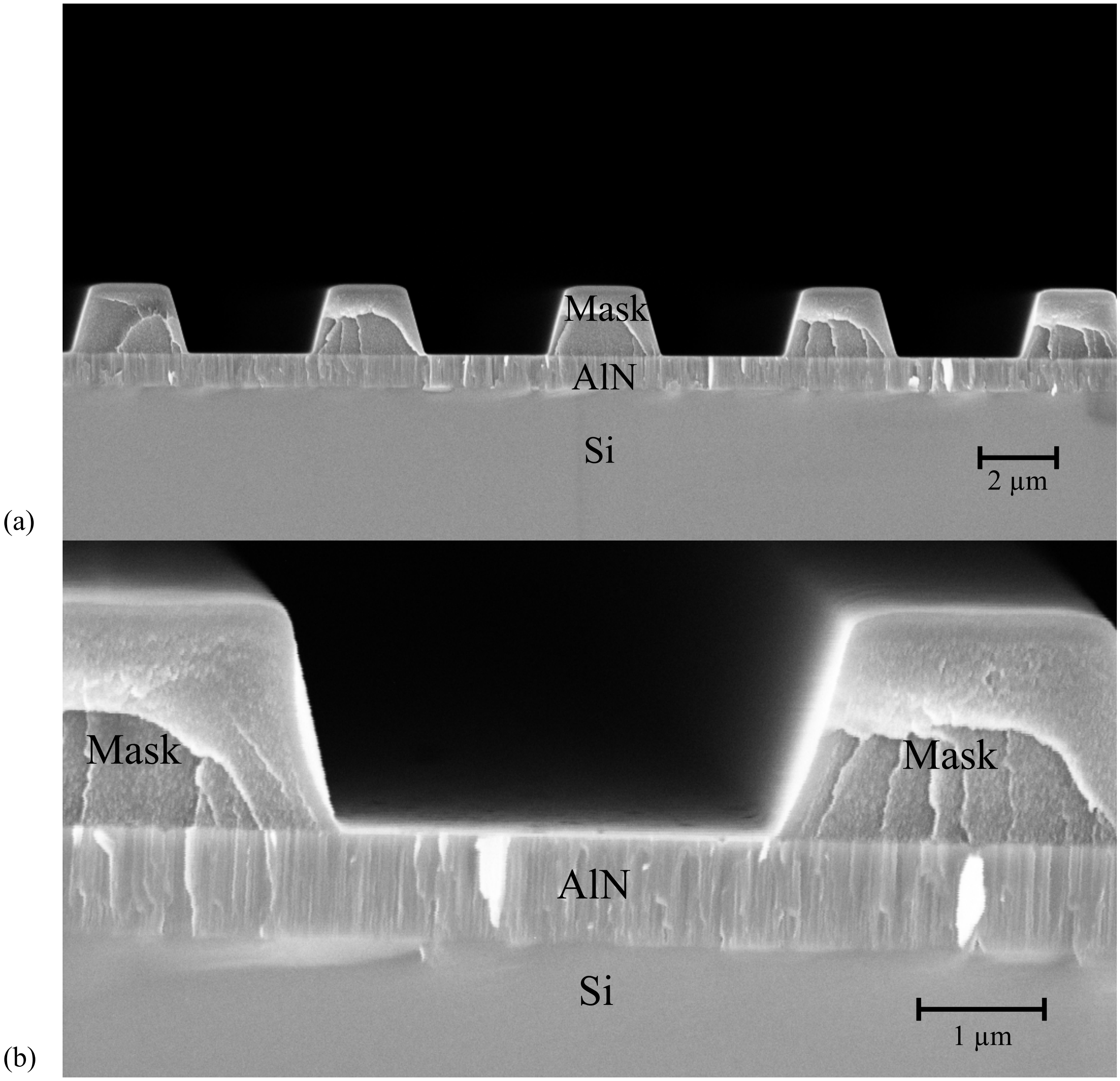

Figure 4.9. Scanning electron micrographs of (0001) AlN pre-implantation. The images were collected at (a) low and (b) high magnifications at an accelerating voltage of 5 kV using a ZEISS 1550 Scanning Electron Microscope.

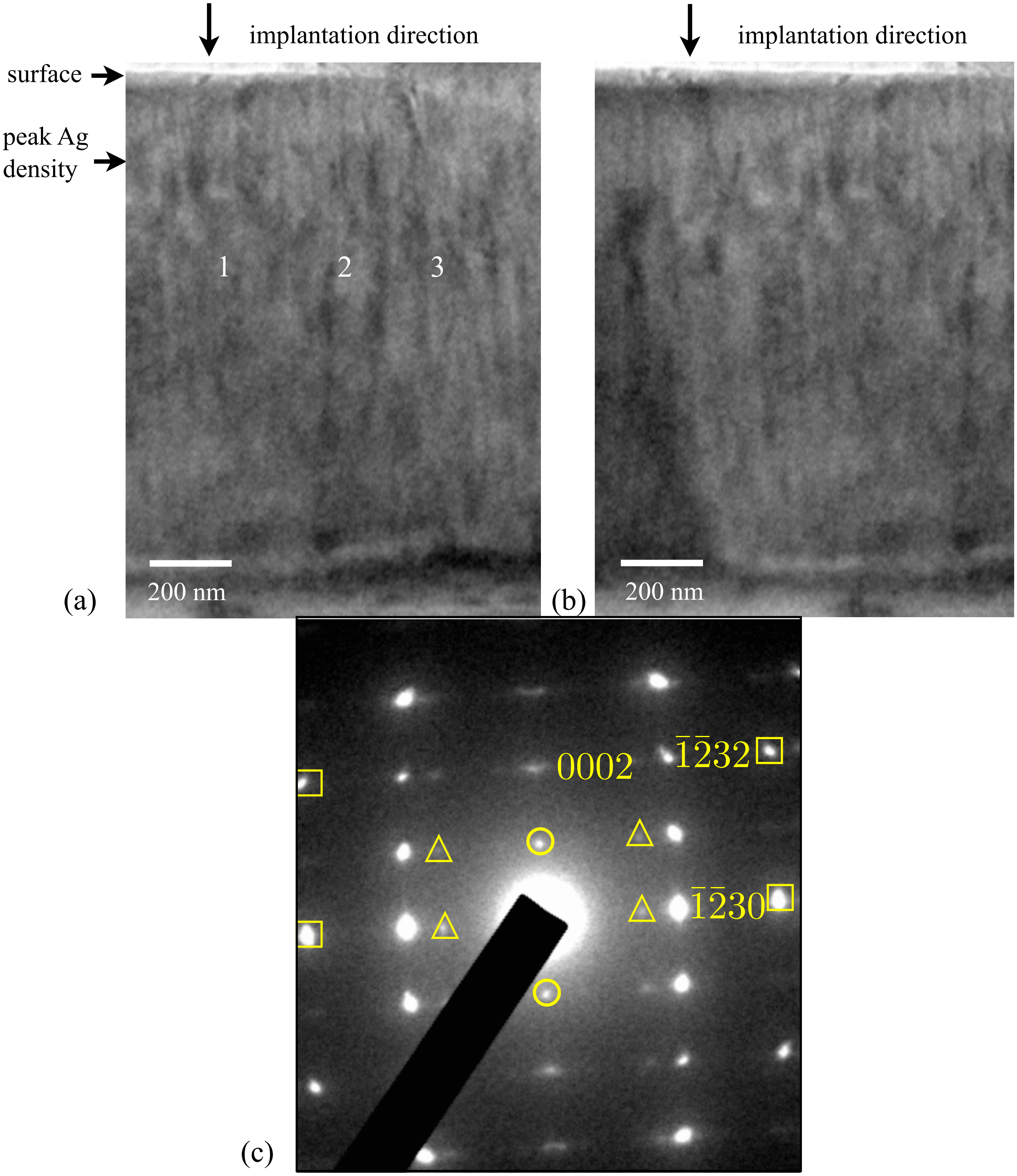

Figure 4.10. Bright-field images at low magnifications (a) – (b) and a selected area diffraction (SAD) pattern (c) of as-implanted AlN with a dose of 1×10^{16} Ag^{++}/cm^2 at a nominal energy of 100 keV. The squares and triangles represent "extra" reflections while the circles are the result of double diffraction. The columnar morphology of the AlN epilayer is visible beneath a thin damaged surface layer, while the diffraction pattern represents the dominant AlN layer.

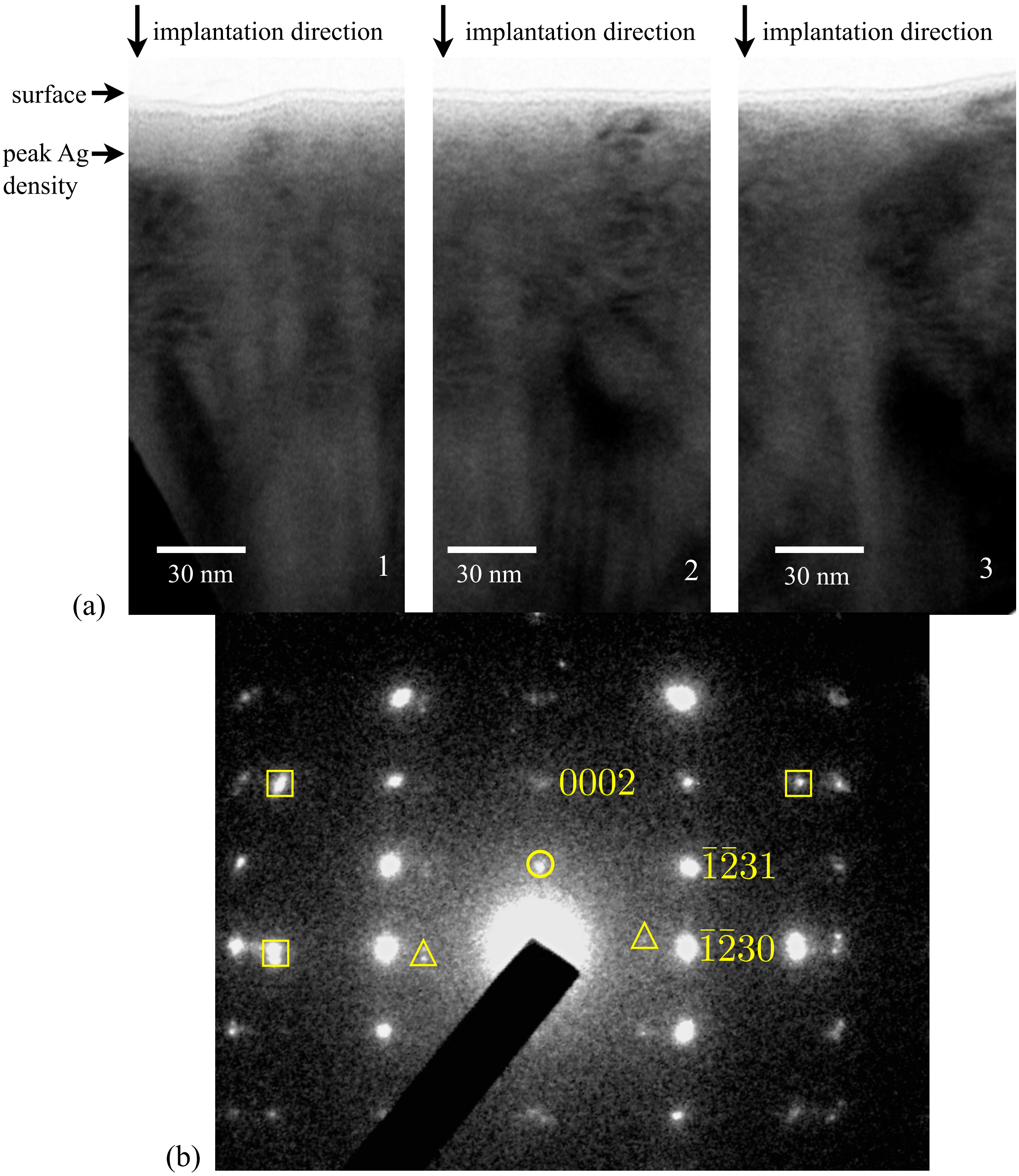

Figure 4.11. Bright field images (a) and selected area diffraction pattern (b) of as-implanted AlN The squares and triangles represent "extra" reflections while the circles are the result of double diffraction. Areas indicated in Figure 4.10 (1) – (3) are shown at higher magnification. The representative SAD pattern (b) for the regions presented in (1) – (3) confirms the dominant HCP structure of the AlN epilayer as well as conspicuous spots not indicative of HCP AlN.

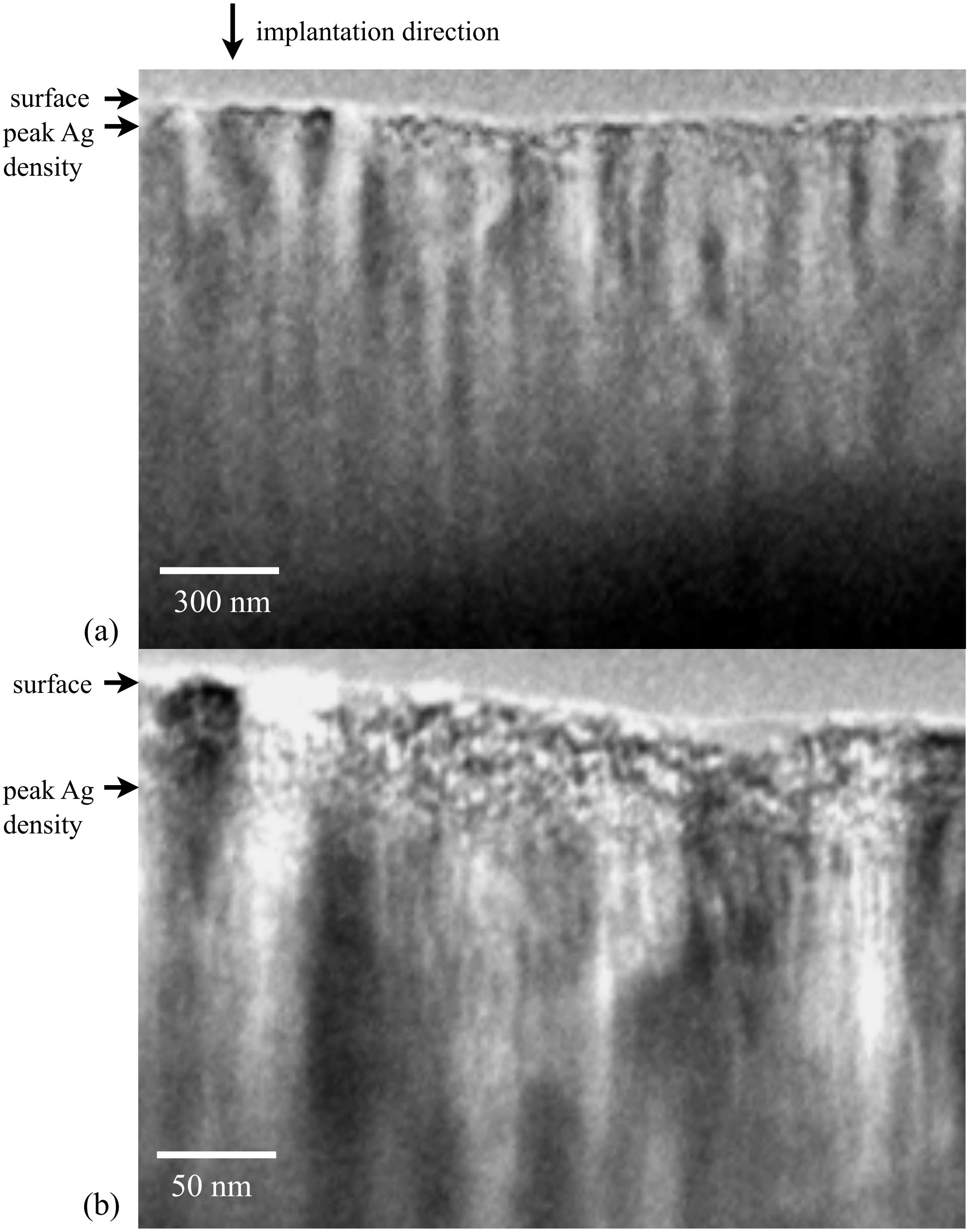

Figure 4.12. Cross-sectional transmission electron micrographs of a Ag-implanted AlN sample with a dose of 1.0 × 10^{16} cm^{-2} followed by a post-thermal annealing treatment at $400^{o}C$ for 1 hour. In the low magnification image (a), localized damage can be identified in some areas near the surface. One such region is shown at high magnification in (b).

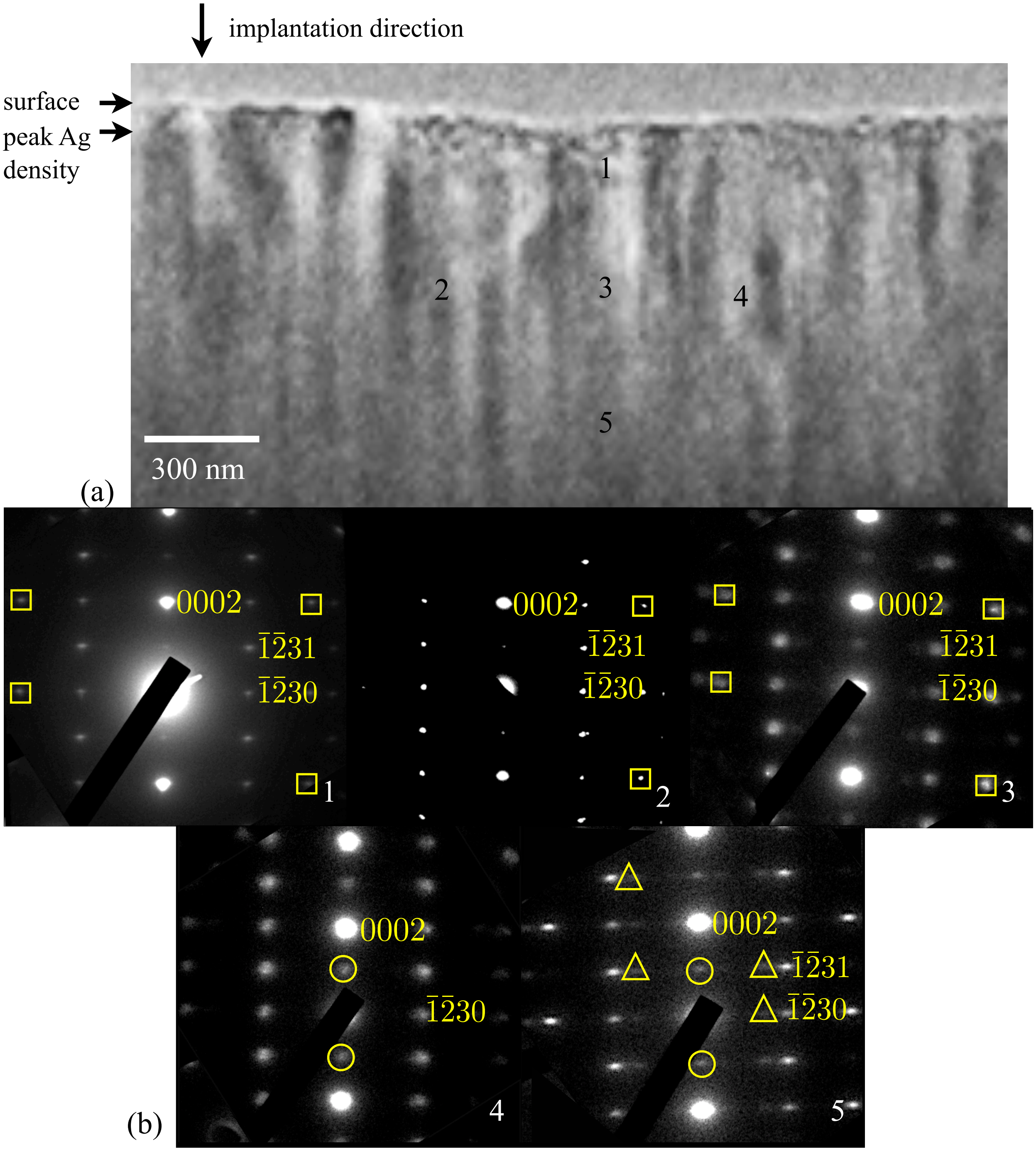

Figure 4.13. Bright-field image (a) and diffraction patterns (b) of *c*-axis oriented AlN post-implantation and thermal annealing at 400°C. Diffraction patterns were taken from areas perpendicular and parallel to the implantation direction. The zone axis for AlN is $2\bar{1}\bar{1}0$.The squares and triangles represent "extra" reflections while the circles are the result of double diffraction.

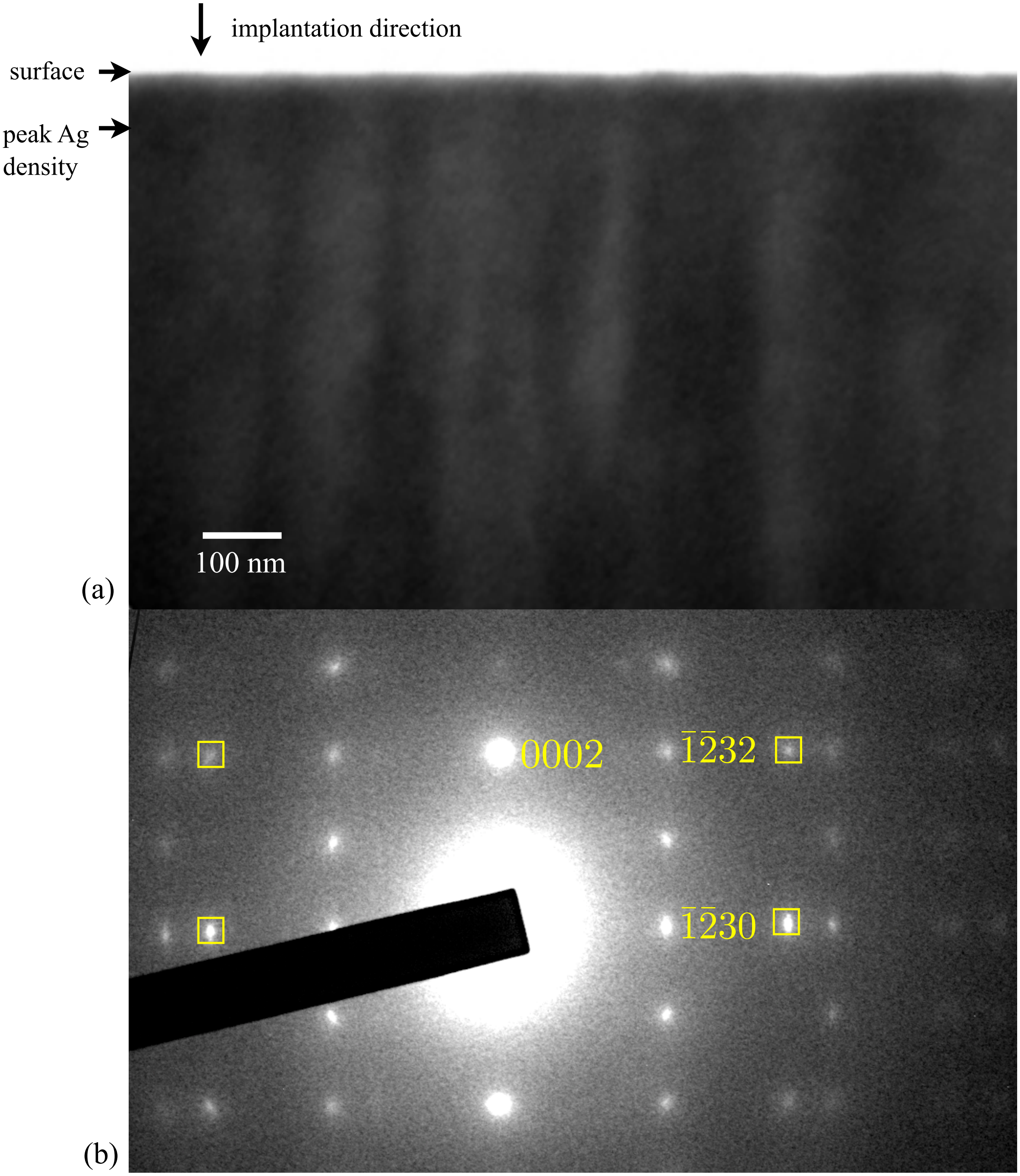

Figure 4.14. Bright-field image at (a) low magnification and the respective SAD pattern (b) of post-thermally annealed samples at 550^{o}C for 10 hours. The columnar structure of the AlN is visible even at this magnification. The SAD pattern consists of the dominant AlN spots as well spots indicative of an alternative structure (squares).

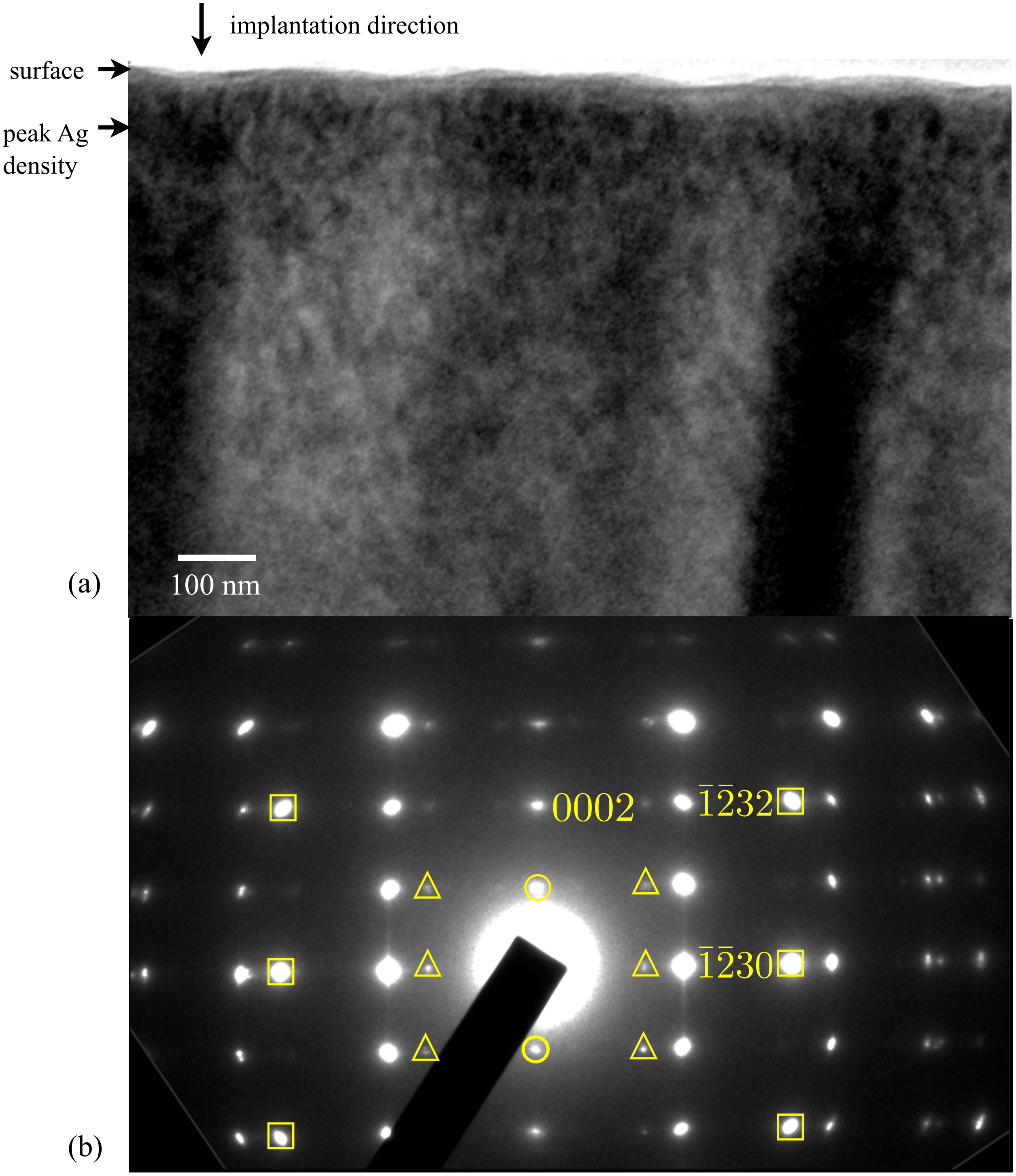

Figure 4.15. Bright-field image (a) at high magnification and selected area diffraction pattern (b) for Ag-implanted AlN post-thermal annealing at 550°C for 10 hours. The columnar morphology of the AlN epilayer is visible in the micrograph. The squares and triangles represent "extra" reflections while the circles are the result of double diffraction.

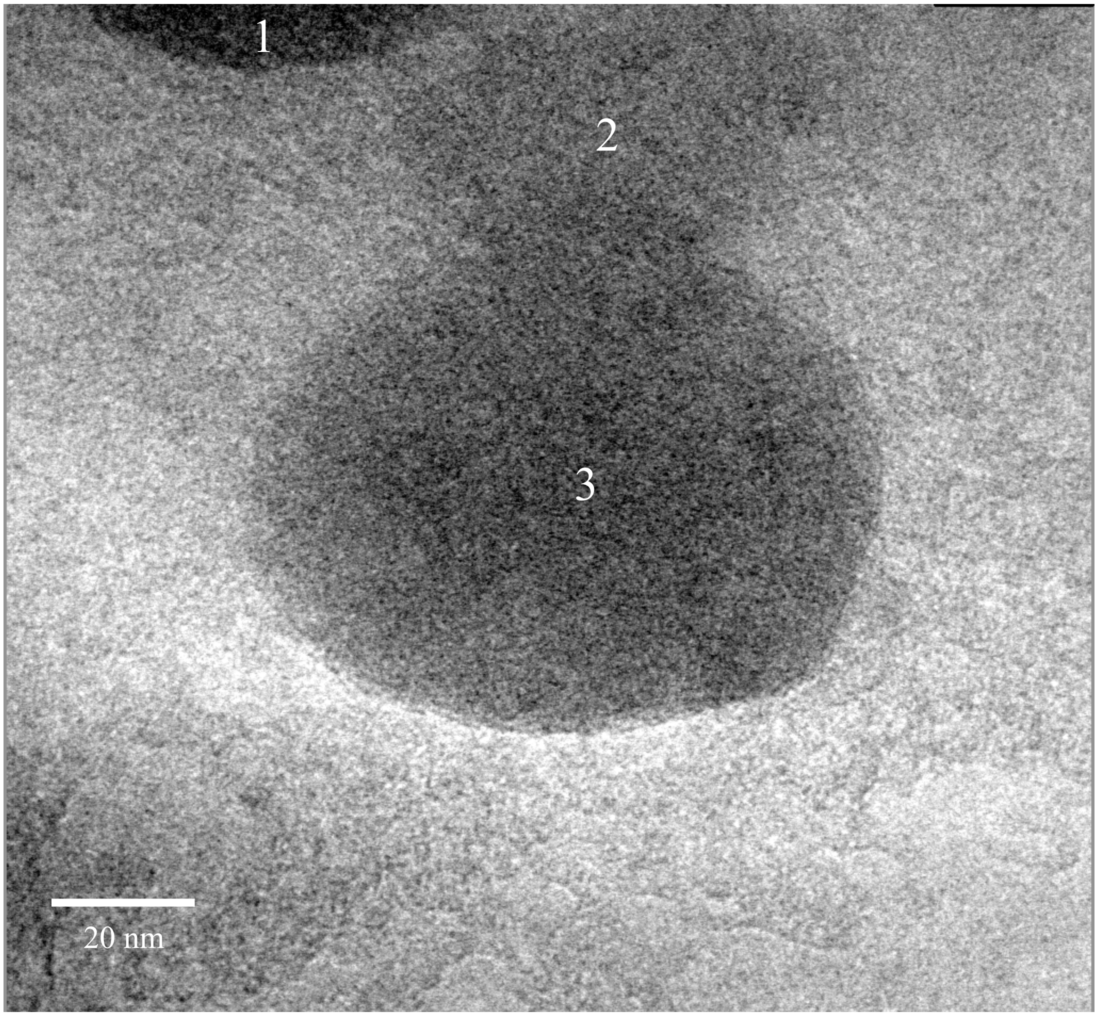

Figure 4.16. Bright-field image of Ag nanoprecipitates within the AlN matrix. Variations in contrast indicate that the nanoprecipitates vary with respect to their depth distribution in the sample or occupy different orientations.

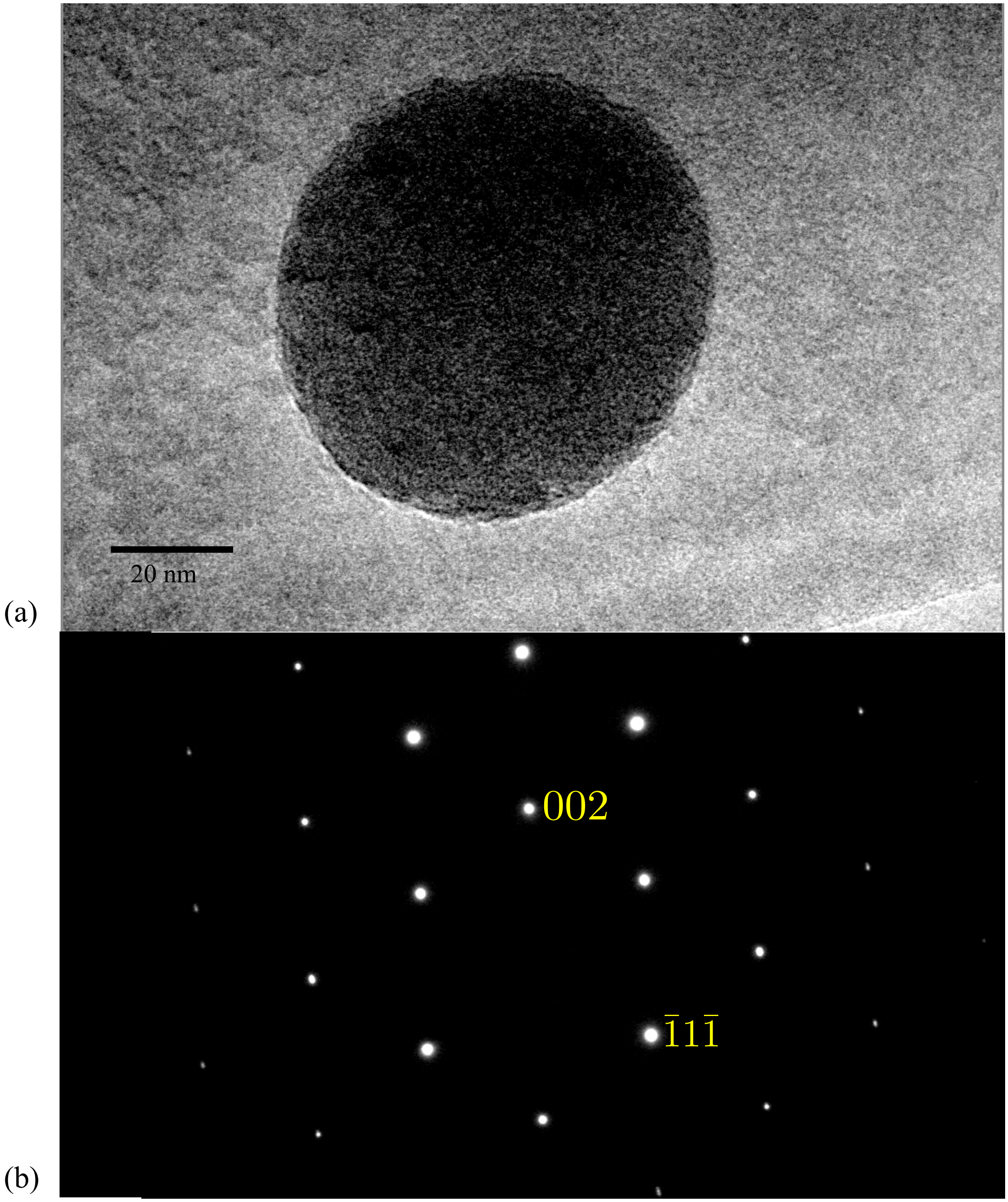

Figure 4.17. Bright-field image (a) and a selected area diffraction pattern (b) of an isolated Ag nanoprecipitate in the AlN matrix. A beam blocker obscures the 000 spot. The nanoprecipitate is spherical in shape with a [110] zone axis orientation.

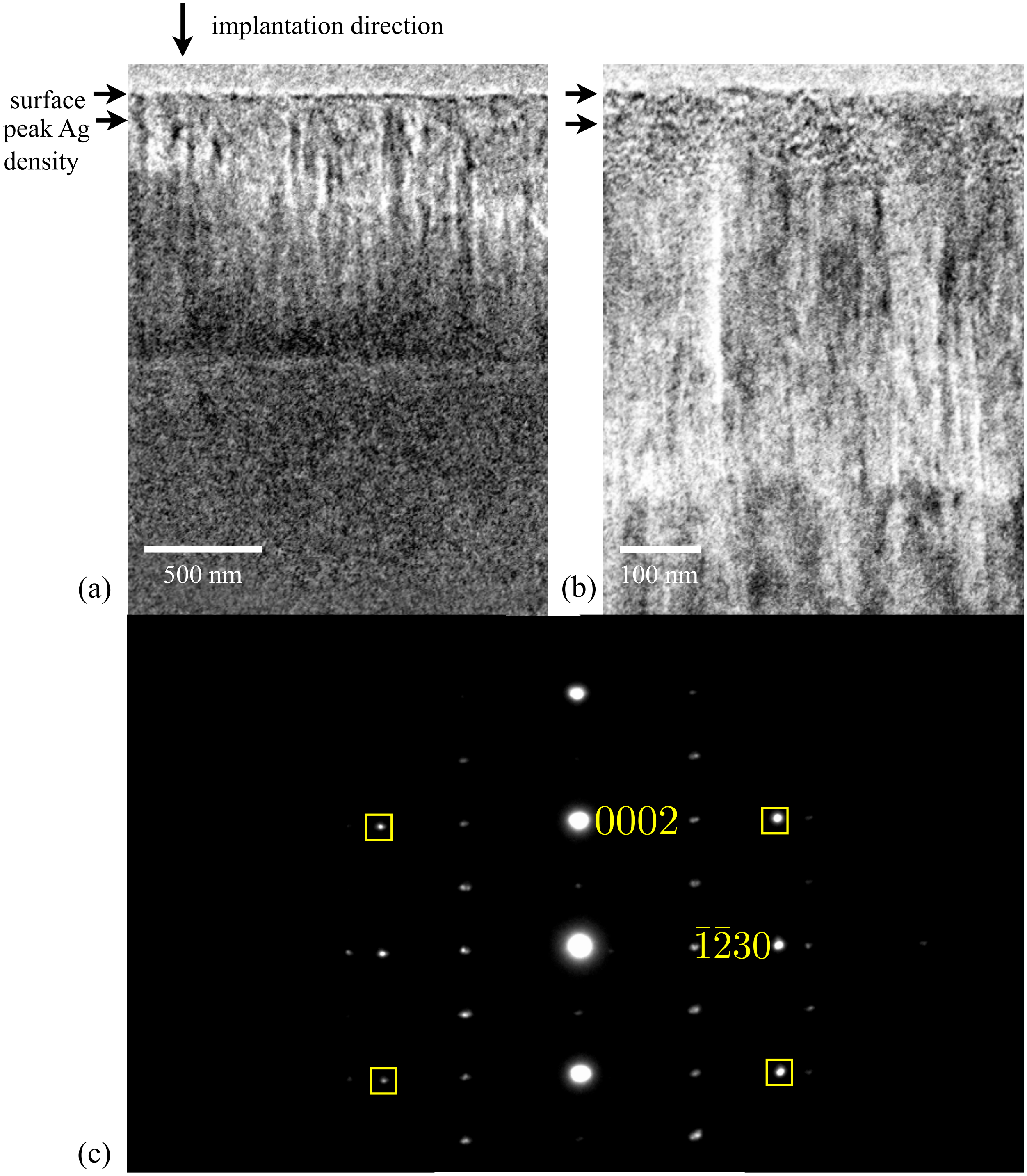

Figure 4.18. Bright-field images (a) at low and (b) higher magnifications and a selected area diffraction pattern (c) of a Ag-implanted sample post-thermally annealed at 600^{o}C for 5 hours. No nanoprecipitates are visible in the image but mottling is apparent for both images (a) and (b). The SAD pattern reflects the dominant AlN matrix with a [$2\bar{1}\bar{1}0$] zone axis.

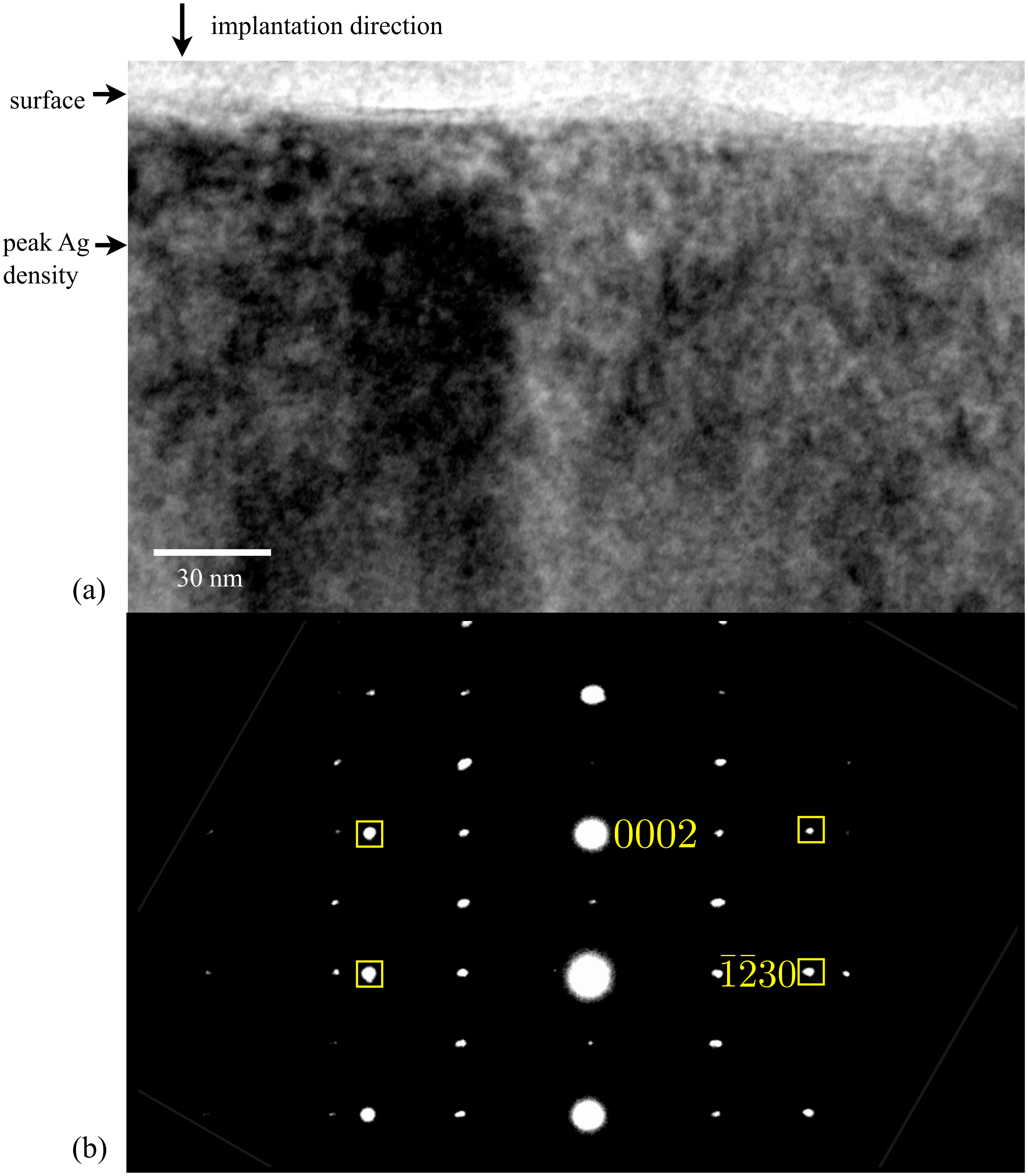

Figure 4.19. Bright-field image (a) at high magnifications and a selected area diffraction pattern (b) of a Ag-implanted sample post-thermally annealed at 600^{o}C for 5 hours.. No nanoprecipitates are visible in the image but the columnar morphology of crystalline AlN is visible.

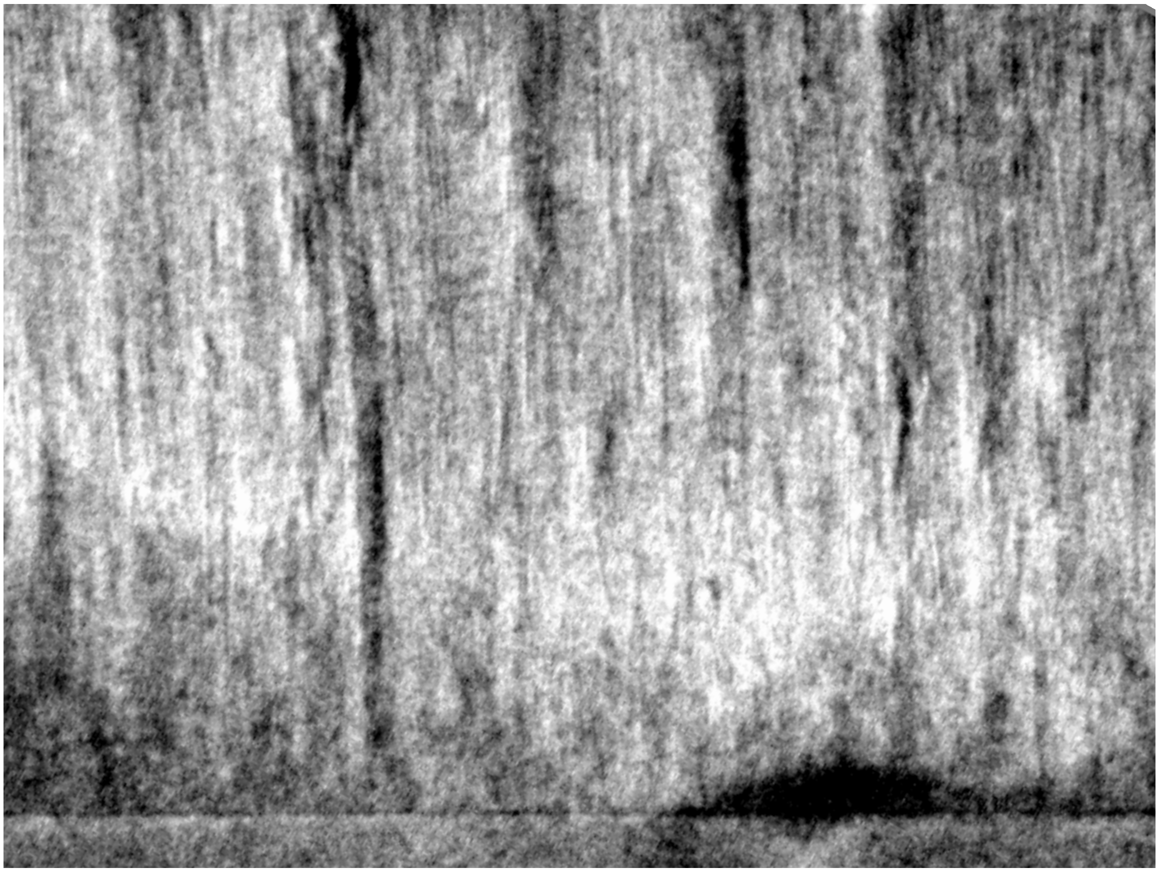

Figure 4.20. Bright-field image of Ag-implanted AlN sample post-thermally annealed at 600^{o}C for 5 hours. There is a singularity exhibiting stark strain contrast at the interface, the origins of which are unknown.

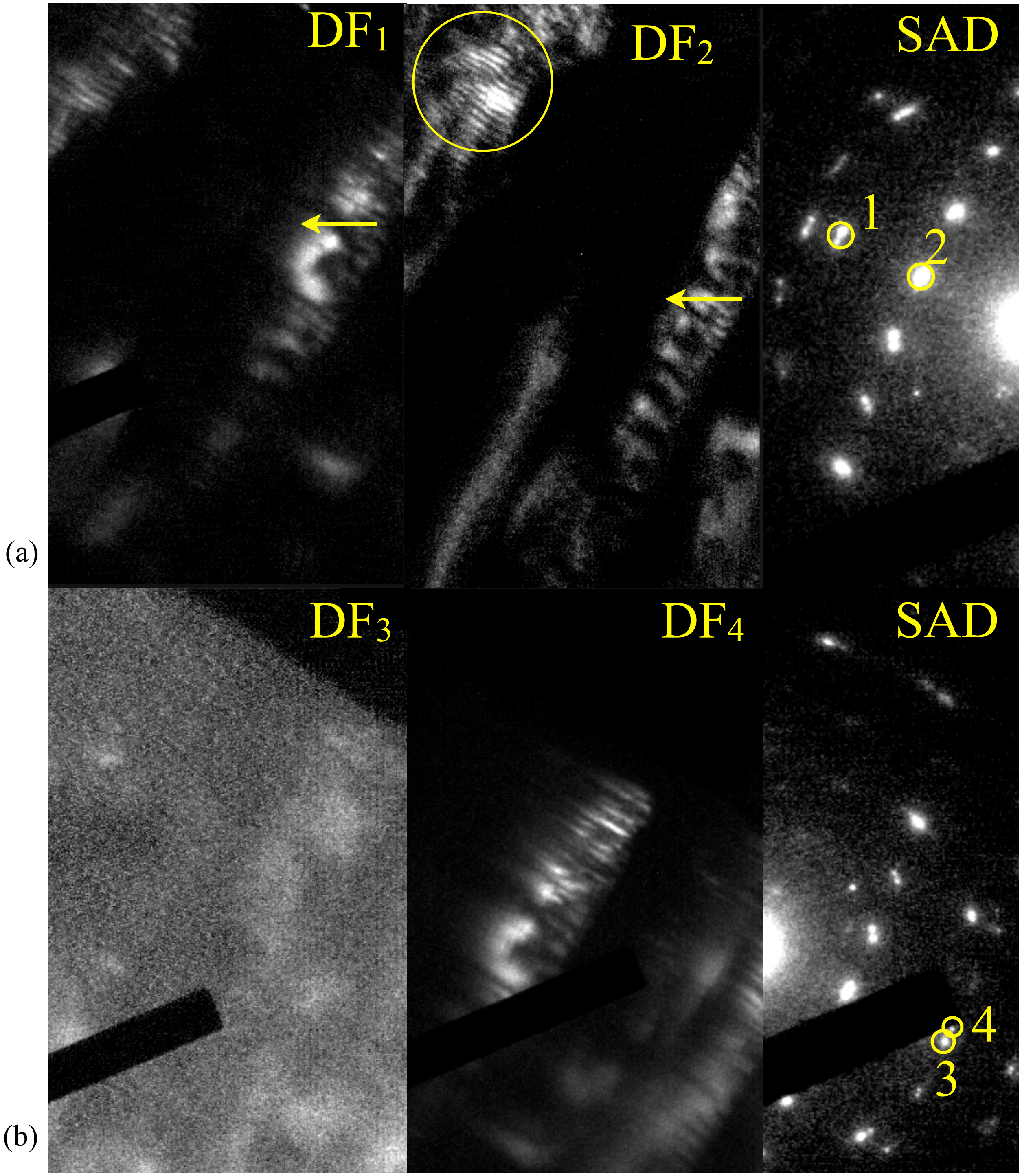

Figure 4.21. Dark-field images of Ag-implanted AlN sample with no subsequent thermal annealing treatment. The respective SAD pattern for the spots used to create the DF images are encircled in the SAD patterns. Moiré fringes and some reversal in contrast are visible in the various patterns.

4.3 Tables for Chapter 4

Annealing	FWHM
No anneal	2.0
400°C 1 hr	1.99
400°C 5 hr	1.97
400°C 10 hr	1.95
600°C 1 hr	2.0
600°C 5 hr	1.98
600°C 10 hr	1.92
800°C 1 hr	1.89
800°C 5 hr	1.9
800°C 10 hr	1.88

Table 4.1. A compilation of FWHM values for (0001) AlN implanted with a dose of 1 × 10^{16} Ag^{++}/cm^2 at 100 keV and post-thermally annealed at 400, 600, and 800°C for 1, 5 and 10 hours.

CHAPTER 5. DISCUSSION

5.1 Simulations

As expected, the computer simulation results acquired *via* TRIM deviated from the RBS data, as shown from the combined plots presented in Figure 4.1. The TRIM results indicate that implantation of Ag into AlN at an energy of 100 keV yields a narrow implantation distribution range with a maximum silver atomic fraction of 0.043 and a projected range, R_p,value of 37 nm from the surface. However, the RBS results indicate a Gaussian distribution with a maximum silver atomic fraction of 0.020 and R_p value of 45 nm. The slight deviation in $R_{p,}$ values obtained using TRIM in comparison to RBS can be attributed to several factors, such as static modeling of the target surface during the implantation process, simplification of the impact parameter and the assumption of a single component energy source. In previous investigations on Cu-implanted AlN, such deviations were attributed to static modeling of the AlN target during the implantation process.[127,147] However, it is speculated that all of these may be contributing factors to the data presented here.

Simulations conducted using TRIM were performed with a static target, which has been proven efficient in predicting depth profiles for experiments conducted at low implantation fluences.[180,181] Conversely, our experiments were conducted at high implantation fluences, and based on the results, a static modeling procedure has proven to be insufficient in predicting the implantation profile. Although there is a "dynamic component" available for TRIM, a precise silver profile was unattainable using the "PAUSE" feature of the program to conduct such dynamic simulations.

Additionally, calculation parameters employed in TRIM do not account for variations in beam energy and "weak" collisions experienced in the vicinity of the target area. The beam energy was computed using the average charge state of the implanted ion and extraction voltage; however, a more accurate prediction could result from taking into account the full range of charge distribution. With respect to "weak" collisions, the assumption is that one collision takes place per atomic volume such that the impact parameter, p, is governed by the following equation:[181]

$$p = p_{\max}\sqrt{r_p} \tag{5.1}$$

where $p_{\max}$ denotes the radius of target atom for each atomic collision and r_p is a random number. However, additional collisions may occur in the target with more distant atoms and thus can influence the pseudoparticle trajectory, where a pseudoparticle is defined as a simulated or incident projectile. When such collisions occur, they modify the energy loss and angular deflection. In fact results have shown that these collisions are dominant in certain classes of materials.[181] Therefore "weak" collisions and dynamic effects are important parameters to consider in understanding implantation effects in multi-component target systems.

Conversely, the results acquired using TRIDYN matched well with the experimental data presented in Figure 4.1. The simulations predicted that implantation of Ag in an AlN target at an energy of 50 keV and dose of 1.0×10^{16} ions/cm^2 yields a Gaussian curve with an R_p value of 45 nm and a Ag atomic fraction 0.020. Consistent with TRIDYN results, the experimental results indicate that implantation yields a Gaussian silver profile with a 0.020 atomic Ag fraction. There is a minor deviation in R_p value in comparison to TRIDYN results (42 nm) however this deviation is within reasonable experimental errors. It is important to note that the TRIDYN simulations in this study were performed at 50 keV, which is half the actual implantation energy, due to limited computing power and memory.

The inconsistencies observed in simulations conducted using TRIDYN in comparison to TRIM can be attributed to: inclusion of "weak" collisions and dynamic composition profile updates. Three "weak" collision conditions are accounted for in TRIDYN using the following equation:[181]

$$p = p_{\max}\sqrt{k + r_p} \tag{5.2}$$

which is a modification of Equation 5.1 with $k = 1, 2, 3$. Additionally, the dynamic composition profile is computed by updating the target layer to account for fluence-dependent ion deposition, atomic mixing and preferential sputtering.[180,181] Both of these factors *i.e.* "weak" collisions and dynamic composition profile updates, contributed to the more accurate profile generated by TRIDYN relative to TRIM. This engenders confidence that TRIDYN generates more reasonable results for the conditions employed in this study.

5.2 Rutherford Backscattering Spectrometry

As shown in Figure 4.2 the AlN stoichiometry for Ag-implanted AlN substrates was confirmed *via* SIMNRA. Based on the simulations performed with a 40 – 70 Al wt. % the experimental results, RBS data, matches well with the SIMNRA simulation for $Al_{0.6}N_{0.4}$. Thus it is concluded that the stoichiometry of the AlN substrate did not consist of the 0.5:0.5 Al to N ratio as initially predicted (and illustrated in Figure 4.2) but rather a 0.6:0.4 Al to N stoichiometry (also presented in Figure 4.2). This modified stoichiometry is not believed to be a result of the ion implantation process because the stoichiometry is retained at depths exceeding the experimental limits of implantation. However, it is believed that this is the original stoichiometry of the as-deposited AlN thin film obtained *via* sputtering.

The RBS data were also utilized to confirm the Ag implantation dose for pre-annealed samples immediately after implantation and after storage for 3 months in an effort to assess any modifications in the system with time. As evident in Figure 4.3, no significant changes are found in either sample as there are no significant shifts in the edge positions for Si, AlN, or Ag. However, an interesting feature is visible in both samples. There is a strong peak positioned at an energy value of approximately 1100 keV, consistent with the oxygen resonance peak. This peak indicates that an oxide layer formed. Similar results were obtained by Yamada *et. al.*[151] for Cu- implanted AlN in which AES results indicated that a 20 nm oxide layer formed. Based on these results it was speculated that an oxide film formed on the AlN surface such that the final sample profile consisted of $Al_xO_{1-x-y}N_y$ layer, AlN implanted with Ag, and Si. This conformation can have major implications in terms of the performance of this system in engineering applications because aluminum oxynitrides do not possess good piezoelectric properties.

In contrast to Figure 4.1, the atomic Ag percent in Figure 4.3 is 4 at. %, consistent with simulations performed using TRIM and significantly higher than the data calculated using TRIDYN. This inconsistency is speculated to result from sample area selection, which is also observed for the annealed samples presented in Figure 4.4, as well as processing limitations that resulted in TRIDYN simulations performed at half the implantation energy. Therefore, due to limited data, it cannot be deduced with certainty whether TRIM or TRIDYN provides a good approximation of the concentration profile with respect to experimental data.

The depth profile, as seen in inset of Figure 4.3, correlates well with the results acquired for the as-implanted samples and the simulations acquired *via* TRIDYN, as seen in Figure 4.1. However, there is a slight shift in R_p for the stored samples with respect to as-implanted samples to approximately 30 nm. No definitive explanation can be presented to elucidate this R_p shift given that oxidation was suppressed by storage under vacuum conditions until use and temperatures that promoted the diffusion of silver ions were not achieved. It was deemed essential that samples be placed under vacuum until because both Al[182] and Ag[173] are prone to oxidation. Samples were also stored at RT to limit the diffusion of the Ag atoms, which occurs at temperatures between (or above) ⅓ and ½ the melting temperature (T_m). At high temperatures the energy barriers for atomic motion can be overcome since the atoms possess higher vibrational energies and movement is significantly more feasible. Thus it was imperative for the samples to be stored under oxidation- and diffusion-limited conditions. Despite intense efforts, the data indicates that oxidation occurred before or after implantation and atomic motion occurred over time. The inconclusiveness of the results is significant with respect to the possible structural modifications that can develop in engineering devices over time and thus their actual shelf-life.

The profiles — full spectra and depth — for samples annealed at 600°C for 5 hours as seen in Figure 4.4 (a) correlates well with the as-implanted samples. There are no major peak shifts in the pre- and post-annealed samples for the Ag, Si, AlN, and O_2 peaks. However one difference worth noting is the increase in the peak representing the oxygen concentration by approximately 26% upon annealing at 600°C (Figure 4.4 (a)). This behavior is also observed in samples annealed at 800°C as shown in Figure 4.4 (b). While annealing was conducted in a nitrogen-rich environment, some residual oxygen was present, which resulted in the increase in oxygen concentration within the samples. An increase in oxygen concentration within the target system can lead to the following, a thicker $Al_xO_{1-x-y}N_y$, or the formation of an Al_xO_{1-x} or Ag_xO_{1-x} compound. Based on the enthalpy of formation for the compounds listed above it is more likely that an aluminum oxide formed. The formation and growth of these constituents can have major implications as these compounds are non-piezoelectric; thus these constituents can significantly retard the performance of such engineering devices as energy scavengers, sensors and actuators.

The depth profile, seen in Figure 4.4 (a) inset, is consistent with the profile observed in the as-implanted samples. Thus there are no detectable shifts in R_p or changes in silver concentration. Similar results are observed for samples annealed at 800°C as presented in Figure 4.4. (b). This confirms the stability of Ag atoms upon annealing. The conformation of the silver atoms, whether as a nanoprecipitate or thin film, is inconclusive based on the RBS data; however, transmission electron microscopy brought the needed resolution to distinguish the morphology, as presented in §5.5. The results presented in Figure 4.4 (a) and (b) are contradictory to those presented in Figure 4.3 where atom migration is visible in samples stored for 3 months in vacuum at RT. This is peculiar because one would expect atom migration to occur at higher temperatures for the same reasons explained in §5.2. Although definitive reasons for this behavior cannot be found based on these limited results, it is our hope that imaging analysis will provide additional clarity.

For samples annealed at 1000°C a similar full spectra profile (Figure 4.4 (c)) is observed however with a more significant increase in oxygen concentration. This behavior is consistent with results presented by Lee *el al.* for unimplanted AlN[152]; these authors reported that oxidation commenced at approximately 800 – 900°C. Additionally, the Ag profile for the as-implanted samples (that were later annealed at 1000°C) exhibits a higher Ag profile than the samples that were later annealed at 600 and 800°C. This is due to the selection of samples from different areas of the wafer. Although measures were implemented to ensure cross-sectional beam uniformity, the variations in Ag profile with respect to sample location could be the result of the shape and acceleration of the ion beam such that a non-uniform distribution of Ag in ion-implanted (0001) AlN is observed in the as-implanted samples.

An unexpected shift in R_p to a deeper *and* shallower depth, in addition to a 16% decrease in Ag concentration, is also found in the samples annealed at 1000°C, as shown in Figure 4.4 (c). The split R_p peak could be attributed to an enhanced oxidation rate and dominance of diffusion-assisted precipitation at higher temperatures. As the oxidation rate increased, the surface film became more oxygen-rich; consequently either a thicker oxide layer and/or a secondary phase, *e.g.,* a different aluminum oxynitride or aluminum oxide formed in the sample. If an alternate film formed, the diffusion rate of silver at the surface would differ significantly from that of AlN. During this process, silver ions diffused down the chemical potential gradient from a silver-rich to a silver-poor region such that silver precipitation was enhanced above and below the oxide/ AlN interface. As annealing progressed, it is the author's assumption that the concentration varied with time. The fundamental equation that governs nonsteady-state diffusion (concentration variations with time) is known as Fick's Second Law, as seen below.[183,184]

$$\frac{\partial C}{\partial t} = \frac{\partial}{\partial x}\left(D\frac{\partial C}{\partial x}\right) \tag{5.3}$$

where C represents concentration, t represents time, x represents distance or position and D represents the diffusion coefficient. Given that annealing was conducted at a temperature exceeding the solid stability limits of silver (T_m of 962°C) and when the oxidation rate was enhanced, the silver and oxygen concentration varied such that the diffusion of particles down the chemical potential gradient occurred until equilibrium was attained. It is the author's assumption that the system was able to reach an equilibrium state under the experimental conditions.

Additionally, under such conditions — annealing at 1000°C — diffusion-assisted precipitation dominates such that a thin film of Ag forms or Ag diffuses to the surface, causing a noticeable decrease in silver concentration observed in the inset of Figure 4.4 (c). This is due to the increase in the diffusion coefficient with an increase in temperature based on the following equation:[183,184]

$$D = D_o \exp\left(-\frac{Q_d}{RT}\right) \tag{5.4}$$

where D_o represents a temperature independent pre-exponential, Q_d is the activation energy for diffusion, R is the gas constant and T represents temperature. It is essential to note that the decrease in Ag concentration resulted in the same Ag concentration observed in samples annealed at 600 and 800°C for 5 hours, as shown in Figures 4.4 (a) and (b). As a result of annealing at a temperature slightly lower than $\frac{1}{2}T_m$ two distinct peaks and a 16% decrease in Ag concentration are visible in the RBS data shown in Figure 4.4 (c) for samples implanted with a Ag dose of 1.0×10^{16} cm^{-2} and annealed at 1000°C.

Based on the RBS results, it is concluded that silver concentration and depth are dependent on annealing temperature especially at temperatures greater than 800°C. The observed differences in the implanted species concentration for as-implanted (and pre-annealed) samples depend on location of sample selection. The slight deviation from the 0.5:0.5 AlN stoichiometry and the potential to form non-piezoelectric secondary phases upon annealing can be the contributing factors to the deviations observed in materials properties, with respect to theoretical calculations, and thus to device performance.

5.3 XRD

X-ray diffraction patterns were gathered from Ag-implanted AlN samples with a dose of 1.0×10^{16} cm^{-2}. Data for as-implanted and samples annealed at 400, 600 and 800°C for 1, 5 and 10 hours are presented. Peaks were identified using the crystal structure factor rule and Powder Diffraction Files [185] for Ag, AlN, Al and Si.

As expected, all the XRD data for samples annealed at 400°C in Figure 4.5. (a) show a prominent 0002 AlN peak and 004 Si peak at 2θ values of 36 and 69° respectively. These results are consistent with the experimental techniques highlighted in §3.1. Slight increases in intensity for the 0002 AlN peak are observed following annealing from 5 to 10 hours. In the as-implanted samples, there is an additional, yet minute, peak evident at 33° that is attributed to the $10\bar{1}0$ AlN peak. However, upon annealing, the $10\bar{1}0$ peak is no longer evident. This was expected because as the temperature increased the kinetic energy also increased such that atomic mobility was enhanced. This resulted in the development of growth texture in the AlN thin film, as indicated by the increase in intensity for the 0002 AlN peak and disappearance of the $10\bar{1}0$ AlN peak. Using the sputter deposition conditions highlighted in §3.1, Figure 4.5 indicates that the preferred orientation of the AlN film surface is the (0002) plane. Surprisingly, no observable Ag peak is identified in either the as-implanted or annealed samples. This is believed to be due to the low concentration, ~ 4.0 at. %, of Ag implanted in the sample, such that the Ag was undetectable *via* XRD. Similar results and conclusions were acquired for samples annealed at 600°C as seen in Figure 4.5 (b).

Analogous to Figures 4.5 (a) and (b), the XRD data for as-implanted samples and the samples annealed at 800°C show a prominent 0002 AlN peak and 004 Si peak at 2θ values of 36 and 69° respectively, for all annealing times. The dominant 0002 AlN peak is also consistent with the data reported for pulsed-laser deposited AlN on Al_2O_3 substrates.[139] Interestingly no $10\bar{1}0$ peak is visible in the as-implanted and samples annealed at 800°C for 1, 5 and 10 hours. Based on these results it is believed that the preferred orientation of AlN implanted with 1.0×10^{16} cm^{-2} and subsequently annealed at 800°C is (0002). Since the samples were cut from the same wafer this result indicates that there is a slight variation in AlN orientation across the wafer. This is consistent with sputter deposition because diffuse transport limits the feasibility of controlled deposition and thus the formation of a uniform film. Additionally, no visible Ag peaks are identified in the as-implanted or annealed samples. This is consistent with the results presented in Figures 4.5 (a) and (b). It is believed that this low concentration, ~ 4.0 at. %, of Ag implanted in the AlN matrix is too low for detection in the diffractometer.

Based on the XRD results for AlN deposited using the technique highlighted in §3.1 and ion implanted with a dose of 1.0×10^{16} cm^{-2} with a subsequent annealing at 400, 600, and 800°C the preferred AlN orientation is (0002). The results also indicate that no significant changes occur in peak position or intensity, even with annealing at higher temperatures and longer times, for the 0002 AlN and 004 Si peaks. Additionally, there is no evidence of Ag present in film or precipitate form. Therefore TEM was employed to elucidate the presence of Ag nanoprecipitates or film in ion-implanted AlN.

It is apparent from the rocking curve results obtained for Ag-implanted (0001) AlN samples annealed at 400°C, as presented in Figure 4.6. (a), that the peak intensity increased with annealing time. Upon closer inspection of Figure 4.6 (b), it is apparent that the full-width half-maximum (FWHM) values tend to decrease with increasing annealing time. As the annealing time was increased from 1 to 10 hours the FWHM values decreased from 1.99 to 1.95, which is indicative of an increase in crystalline order due to a decrease in strain (due to reduction in defect concentration) and/or grain size increase (due to grain growth). A FWHM value of 2.0 was also reported in the work of Iriarte *et al.*[63] for unimplanted *c*-axis oriented AlN thin films deposited on a Si substrate *via* reactive sputtering which, with a FWHM value of 2.0, were deemed highly oriented in the *c*-axis. This is also consistent with the XRD data, which indicates that an increase in annealing temperature results in an increase in preferred orientation, specifically an (0002) film plane texture, as a consequence of grain growth. Given that the thermal annealing treatment was conducted at low temperature significant growth is not anticipated. Therefore annealing at 400°C under increasing times yields an increase in crystal order in the implanted sample relative to the as-implanted *c*-axis oriented AlN samples.

Similar to the samples annealed at 400°C (Figure 4.6 (a)), the samples annealed at 600°C show an increase in peak intensity with increases in annealing time as shown in Figure 4.7 (a). Additional similarities are observed between Figure 4.7 (b) and Figure 4.6 (b). The values for FWHM decrease with increased annealing time from 1 to 10 hours. A compilation of these values is presented in Table 4.1. As the annealing time increased from 1 to 10 hours the FWHM decreases from 2.0 to 1.92, indicating a larger grain size. The higher temperature and longer annealing time favored diffusion in these samples, augmenting the approach to equilibrium.

Additionally, 600°C is closer to the value (⅓ – ½ T_m for AlN) required for crystalline recovery and removal of defects. These results are consistent with theoretical predictions that identify 600°C (~⅓ T_m) as the temperature most likely to result in full-scale crystallization and defect annihilation.

Results consistent with those obtained for the samples annealed at 400 and 600°C were found in samples annealed at 800°C, as seen in Figure 4.8. As evident in Figure 4.8 (a) the peak intensity increases with increasing annealing time while in Figure 4.8 (b) the FWHM values decrease with increasing annealing time. The FWHM values are also presented in Table 4.1 and indicate that the FWHM values decrease from 1.89 to 1.88 with increasing annealing time from 1 to 10 hours. These values ae the smallest obtained from all the samples, whether pre or post-annealing. This is due to higher diffusivity, which led to enhanced coarsening.

Based on the rocking curve results for samples implanted with a dose of 1.0 $\times 10^{16}$ ions/cm^2 and subsequently post-thermally annealed, an increase in peak intensity is observed. Additionally, annealing times of increasing duration yield an increase in crystal order with the lowest FWHM value observed in samples annealed at the highest temperature and time, *i.e.* 800°C for 10 hours. This is an anticipated result because higher temperatures and longer times induce more diffusion-assisted microstructural changes. Such changes yield a reduction in defect concentration and thus an overall reduction in strain energy, to ultimately render a material with enhanced crystalline order. Therefore it is concluded that annealing temperature and time play a significant role in producing a more strain-free sample with larger grain sizes. In addition, annealing provides a mechanism to reduce the defect concentration and coarsen the highly *c*-axis oriented AlN thin films generated by sputter deposition.

5.4 Scanning Electron Microscopy

Cross-sectional SEM analysis was performed on a patterned and implanted specimen prepared from Implantation 1. A cross section through a metallic mask was obtained and is presented in Figure 4.9. The actual thickness of the sputtered AlN was determined to be approximately 890 nm with no evidence of silver implantation. The limited resolution of the SEM prevented any determination of the Ag depth profile by EDS. Thus, in order to elucidate the depth profile for Ag-implanted AlN a technique with enhanced resolution, on the Angstrom scale, such as TEM, was employed.

5.5 Transmission Electron Microscopy

To understand the microstructural development of Ag in AlN as a result of thermal annealing treatments, one must understand the microstructure of the as-implanted thin film (all data presented in this section are from Implantation 2 unless otherwise noted). Figure 4.10 is a cross-sectional image of 1,100 nm thick AlN implanted with 1 × 10^{16} cm^{-2} at room temperature. The microstructure exhibits a columnar morphology associated with crystalline diffraction patterns, revealing that the AlN was not damaged to the point of amorphization by Ag^{2+} ion implantation.

The RBS data presented in Figures 4.2 – 4.4 suggest that oxygen is present within the first 40 nm of the surface; however, based on the images presented in Figures 4.10 (a) and (b), no conspicuous oxide film or other oxygenated constituent is evident. Based on this evidence it is suspected that oxygen may be dissolved in solid solution, perhaps the interstitial sites associated with the AlN matrix, and not as distinct second phase particles. Deeper in the sample, at the depth of maximum Ag density (referenced in §5.1 as the projected range, R_p), approximately 45 nm from the surface, no Ag precipitates are discernible as this dose appears to be too low to induce precipitation without further thermal annealing treatments.

Even at low magnifications (Figures 4.10 (a) and (b)), variations in contrast can be perceived. However, within the first 100 nm of the implantation region no such variations can be observed. This is the result of strain in a highly damaged *c*-axis oriented AlN due to the accommodation of the implanted species at high energies and the lack of thermal activation to recover from displaced defects that developed during implantation. The damage induced from ion implantation is evident up to 200 nm from the surface because the columnar structure, alternating in contrast, is visible at a depth of 200 nm from the AlN surface. Based on these results, damage to the AlN epilayer, as a result of the ion implantation treatment, extended beyond the Ag depth profile as predicted using TRIM and TRIDYN; however, enhanced imaging analysis must be conducted for confirmation.

The complex diffraction pattern for the as-implanted sample is presented in Figure 4.10 (c). The bright spots indexed are those of AlN. The presence of spots confirms that the AlN retains its crystalline morphology post-implantation. Based on the standard spot patterns the zone axis of the HCP AlN is $2\bar{1}\bar{1}0$. “Kinematically forbidden” reflections can also be observed in these samples, such as the 0001 spot, which is located half the distance between the 0002 reflection and the direct beam and represented by the circle, for HCP AlN. The faint spots (highlighted with triangles and squares) located near the indexed spots suggest the presence of planar defects, silver precipitates or relrods but cannot be uniquely identified using SAD alone. Identification of the “extra” reflections, labeled with squares and triangles, was attempted using the structure factor rules and WebEMAPS for the possible species including Al_2O_3, AlON, cubic AlN, and Ag, however; this approach yielded no conclusive answer. The most probable candidate was Al_2O_3, because the sputtering data collected *via* TRIM (not shown), which is also consistent with the linear collision cascade, predicts that the sputtering rate of N_2 is significantly higher than that of Al, consequently, excess Al is expected to be available near the surface. In addition, the heat of formation for α-Al_2O_3 is more negative than AlN (–399.09 vs. –57.7 kcal/mole) thus it is easier for Al to oxidize to form an Al_2O_3 than an AlN. However, this too could not be confirmed using the methods mentioned above. X-ray diffraction results provided no further clarity as no Ag peak was identified and planar defects and relrods cannot be resolved using this technique. However it is reasonable to interpret these spots as a result of planar defects or relrods due to the lack of Ag nanoprecipitates in the TEM image and Ag peak in XRD. Thus additional experiments, as discussed below, are essential to interpret the faint spots present in the diffraction pattern.

The subsequent figure, Figure 4.11, presents a cross-sectional bright-field image and diffraction pattern for as-implanted AlN taken at higher magnification. Even at higher magnification, no Ag nanoprecipitates are visible. Hence, these images confirm that a post-thermal annealing treatment is essential to induce precipitation effects in Ag embedded in an AlN matrix. In the darker areas to the left of the implantation region, labeled 1–3, dark streaks are present. At higher magnification, variations in contrast are present within the first 100 nm from the surface and are the result of structural variations of the AlN. However, this distinction in contrast is difficult to discern at lower magnifications. Within the first 30 nm of the surface, the columnar structure of AlN is non-existent; however, evidence of this morphology is evident within the 45 – 100 nm range. This result is interesting because significant damage was anticipated at the projected range site, 45 nm; however, storage at room temperature for months may have provided sufficient thermal activation to encourage migration of both Al and N atoms, where the latter is more probable, and thus an opportunity for the evolution of a crystalline state. Immediately below the 100 nm regime the structure is more consistent with the columnar morphology seen in as-grown aluminum nitride films.[186] This indicates that the damage is in fact confined to the top 100 nm regime within the AlN. Similar observations for the diffraction pattern shown in Figure 4.10 are observed in Figure 4.11 (b).

The next figures document the microstructural development of ion-implanted AlN and the morphology of Ag precipitates as a result of thermal annealing. Figure 4.12 shows Ag-implanted AlN annealed at 400°C. In contrast to the as-implanted sample, the columnar structure of AlN is visible at both low and high magnifications in the samples thermally annealed at 400°C for 1 hour. Close examination of the low magnification micrograph indicates that a non-uniform columnar structure evolved during this thermal annealing process. In some areas of the AlN epilayer the columnar morphology extends to the AlN surface, while in others it is visible at approximately 30 nm from the surface. Analysis of the implanted AlN sample at higher magnifications clarifies the structural characteristics of the implanted regime. Mottling, which is vacancy and interstitial clusters, is discernible within the first 50 nm of the surface. These results are consistent with those reported by Kucheyev *et al.*[148] in which a damaged, but not amorphous, AlN evolved as a result of Au^+ implantation in an AlN matrix.[8] The degree of damage below this area is indiscernible due to the lack of clarity in the image. Additionally, no evidence of an oxygen phase is present in the TEM micrograph thus confirming that no oxide film formed in our samples. Based on the RBS data, which indicates that oxygen is present in these samples, it is interpreted that oxygen occupies the interstitial sites and does not precipitate out to form a second phase, such as that demonstrated by Yamada *et al.*[151] Similar results on the lack of oxide film formation are obtained in samples thermally annealed at higher temperatures (Figures 4.14, 4.15, 4.18 and 4.19).

Selected area diffraction (SAD) was performed at multiple locations within the image to assess the uniformity of the AlN matrix (Figure 4.13 (b)). The squares and triangles represent diffraction spots from alternate constituents while the circles represent reflections as a result of double diffraction in HCP AlN. Areas scanned parallel to the surface (2 and 4) exhibited subtle distinctions — kinematically forbidden reflections (circles) are observed in (4) but no “extra” reflections (squares and triangles) are present; however, in z(2), conspicuous spots are present but no kinematically forbidden reflections. Additionally, the spots appear sharper in (2) with respect to (4) indicating enhanced Bragg diffraction. When the field-limiting aperture was placed over the dark band (2) the AlN spots due to double diffraction disappear but when the aperture was displaced to the area over the bright region (4), the “extra” spots disappear. This is interesting because the conspicuous spots observed in (2) may be the result of localized planar defects within the dark band of the columnar structure. If we look at the diffraction pattern closer to the surface, (1), higher order Laue spots representing the $[2\bar{1}\bar{1}0]$ HCP AlN pattern are invisible, while the distinctive spots are present. However, upon descending farther into the sample surface (3) and (5), double diffraction, "extra" spots and AlN spots are disclosed. These additional spots are similar to those observed in the sample prepared without annealing. It is speculated that the angle of diffraction from the higher order Laue zones was outside the radius of the aperture and thus did not participate in the pattern observed for (1). Since the diffraction pattern for (1) is close to the damaged region, it is speculated that the spots are a result of planar defects that remain as one transcends deeper into the AlN matrix. In (5), the spots appear sharper, indicating strong Bragg diffraction deeper into the AlN epilayer. Additionally, "extra" reflections (triangles) are visible which also seem to indicate the presence of planar defects. Since no consistent pattern can be mapped for these spots, the possibility of a second phase was discounted. Therefore an alternate mechanism is considered.

Atoms near the surface are bonded to fewer nearest neighbors than bulk atoms and therefore possess a higher energy state than interior atoms. At the surface, atomic mobility is more facile and thus atomic relaxation is possible. However, such relaxation is difficult to achieve in regions further from the surface because the number of neighbor atoms increases and mobility is restricted. Thus to reduce strain, which in this particular case has occurred as a result of ion implantation, the material adopts a mirror lattice symmetry with respect to the original close-packed lattice conformation, resulting in two-dimensional defects such as *twinning*, *small-angle grain boundary* or *stacking faults*. Two-dimensional defects cause multiple diffraction effects resulting in "extra" diffraction spots in the SAD pattern, such as those observed in Figures 4.13b for areas (1) – (3). Similar spots can be observed in the pattern collected from an area closer to the Si substrate (5); however they are missing in the pattern collected at an area closer to the surface (4).

While thermal annealing at 400°C is theoretically conducive for diffusion-assisted precipitation in Ag, which has a T_m of 962°C (however this value can change with changes in nanoparticle size), data from this study leads to the conclusion that 1 hour is an inadequate time for such precipitation effects to occur. Additionally, annealing at such low temperatures for a short period of time is inadequate to promote diffusion-assisted growth of AlN.

Low and high magnification transmission electron micrographs for samples thermally annealed at 550°C are presented in Figures 4.14 (a) and 4.15 (a). It is important to note that this particular data set was collected from Implantation 1, which varied with respect to film thickness (880 *vs*. 1100 nm as noted), dose (2.43×10^{16} cm^{-2} *vs*. 1.0×10^{16} cm^{-2}: note the decrease in concentration with respect to the as-implanted sample with a concentration of 2.68×10^{16} cm^{-2}) and ion implanter (MEVVA *vs*. Varian 350D). In contrast to the as-implanted sample, the columnar structure of AlN is visible at both low and high magnifications in samples thermally annealed at 550°C for 10 hours. Additionally, the widths of the columns observed in the 550°C annealed samples, approximately 136 nm, are significantly larger than that of the as-implanted and 400°C samples (29 and 30 nm, respectively). Although 550°C is significantly lower than the melting temperature of AlN (> 2000°C) and conditions in which diffusion assisted growth of AlN are limited, crystalline recovery is observed. This is the result of conducting the annealing treatment for an extended period of time to allow for diffusion-assisted growth, and thus recovery, of crystalline AlN. Representative SAD patterns are shown in Figure 4.14 (b) and 4.15 (b). With respect to the as-implanted sample, “extra” diffraction spots can be observed in the SAD pattern for the 550^{o}C thermally annealed sample, and the spots appear brighter and sharper, indicating strong Bragg diffraction and/or a higher volume fraction of the phase generating them. It is also anticipated that a highly oriented AlN structure developed as a result of the thermal annealing treatment employed in this study. The “extra” reflections observed in the diffraction patterns, appear to be due to the presence of planar defects, which occur to accommodate the localized strain as a result of the embedded Ag nanoparticles shown in Figures 4.16 and 4.17. However, this requires additional bright-field (BF) and dark-field (DF) imaging to confirm.

A TEM micrograph of the nanoprecipitates found in the 550^{o}C thermal annealed samples is presented in Figure 4.16. Clusters of Ag nanoprecipitates, with average diameters in the range of 40 – 90 nm, can be identified. The precipitates shown in this micrograph vary in contrast, which could be due to their depth distribution in the sample or to their different zone-axis orientations. Based on this evidence, it is reasonable to conclude that there is no preferred Ag orientation distribution within the AlN matrix.

The majority of the nanoprecipitates are located at approximately 40 nm from the surface, consistent with the TRIM and TRIDYN results simulated at 100 keV and 50 keV, respectively, and the RBS data presented above (Figure 4.1). Interestingly, these nanoprecipitates are dispersed throughout the matrix and not on preferential high-energy sites such as grain boundaries. It was anticipated that grain boundaries would be the preferential sites for the Ag nanoprecipitates. Additionally, the nanoparticles are observed to exhibit a circular, equiaxed morphology with no faceting evident at their interphase interfaces. This morphology suggests that the Ag precipitates have an isotropic interfacial energy with the AlN matrix, which could oppose the formation of a continuous buried conductive layer due to the lack of a suitable habit plane for high-aspect-ratio lateral growth.

An isolated Ag nanoparticle is visible in Figure 4.17. This nanoparticle is present at approximately 40 nm from the surface and appears circular in shape (Figure 4.17 (a)). The associated diffraction pattern, Figure 4.17 (b), indicates that the zone axis orientation of the Ag nanoprecipitate is [110]. The sharpness of the spots also indicates perfect crystallinity throughout the particle. Thus a thermal annealing treatment at 550^{o}C for 10 hours appears sufficient to encourage crystal growth of AlN as well as diffusion-assisted precipitation of crystalline Ag in the AlN matrix.

Close examination of Figure 4.18 and Figure 4.19 reveals that the microstructural development and precipitate morphology differ depending on the dose, crystalline quality of the AlN epilayer and the type of implanter utilized. While different implanters were used to prepare samples for Implantations 1 and 2, it was believed that similar characteristics would be observed in the samples under similar thermal annealing conditions. However, significant distinctions can be observed in Figures 4.18 and 4.19 with respect to Figures 4.14 and 4.15.

Although the annealing temperature for the samples exhibited in Figure 4.18 is slightly higher than that of Implantation 1 (600 *vs.* 550^{o}C), mottling is present within the first 100 nm from the surface, and no visible precipitates can be observed in these samples. At lower magnification (Figure 4.18 (a)), no structural modifications or damage are visible; however, at higher magnifications (Figure 4.18 (b) and Figure 4.19 (a)), significant distinctions become more apparent. First, damage (seen as mottling) resulting from ion implantation is apparent within the first 100 nm from the surface. Evidence of mottling is apparent within the projected range of 45 nm from the surface and extends throughout the implantation regime of 100 nm. Additional experiments must be conducted to confirm the type of mottling present. Additionally, the mottling observed follows the same columnar morphology of undamaged AlN. Because there are no barriers to the advancement of AlN growth, if adequate thermal activation is supplied, crystal growth of AlN should occur with ease. Below this area the customary AlN columnar morphology exists. The darker band visible at approximately 263 nm from the surface is the result of variations in thickness changes and not the result of compositional variations within the sample.

Although the annealing temperature is slightly higher (600 *vs.* 550^{o}C), no visible precipitates can be observed in these samples even at the depth of maximum Ag density (Figures 4.18 (a) – (b) and 4.19 (a)). This could be due to a slightly lower concentration of Ag present in these samples with respect to those presented in Figures 4.14 and 4.15 (1.0 *vs*. 2.43 × 10^{16} cm^{-2}) as indicated by the RBS data (not shown). Thus, to certify the presence of Ag within the AlN matrix, an energy-dispersive method for elemental analysis is required. Results from energy dispersive spectrometry were obtained using an SEM with EDS capabilities (not shown here), and they do confirm the presence of Ag in the sample, even when no nanoprecipitates were visible. These results suggest that the Ag ions occupy substitutional sites in the hexagonal close-packed structure of AlN. Since Ag has a $^{+}$2 charge, it is more likely to substitute for Al, which has a $^{+}$3 charge (in comparison to N, which has a $^{-}$3 charge). Charge compensation may come from the injection of O^{2-} ions, which is corroborated by the RBS data showing an oxygen signal, possibly on nitrogen sites. This is consistent with the results published by Li *et al.*,[145] in which Mn^{+2} occupied the Al substitutional sites and coalescence was not observed until the Mn^{+2} concentration reached the critical value for nanoprecipitate formation. Based on these results it is concluded that a dose of 1.0 × 10^{16} cm^{-2} is too low to induce precipitation even with a low-to-moderate temperature thermal annealing treatment for an extended period of time.

Subtle distinctions are observed in the diffraction patterns for the 600^{o}C thermally annealed samples (Figure 4.19 (b)) with respect to the data previously reported for the as-implanted and 550^{o}C annealed samples (Figures 4.11 (b) and 4.15 (b)). The sharpness of the indexed diffraction spots observed in the 600^{o}C annealed samples confirms the dominance of the AlN matrix as well as the presence of relrods or two-dimensional defects such as stacking faults or twins. Additionally no diffraction spots from pure Ag can be observed, and thus a chemical analysis method would need to be implemented to establish the location of Ag in these ion-implanted AlN samples.

Evaluation of the AlN-Si interface is also critical because this is where the integrity of the device lies. Figure 4.20 is a cross-sectional bright-field image collected at the interface of the

AlN thin film and the Si substrate for the thermally annealed sample. Ion implantation is believed to yield no effect in this region as it is beyond the implantation region, as confirmed in the TRIM, TRIDYN, RBS, and previously reported TEM data. It is speculated that the dark area located at the AlN-Si interface is associated with strain contrast due to the lattice mismatch of AlN thin film growth on a Si substrate (Si lattice constant is 5.43 in comparison to AlN, which has lattice constants of 4.98 and 3.10 Å,). Materials can accommodate this amount of strain during film growth *via* different mechanisms — second-phase formation or misfit-accommodation dislocations at the interface; however, both of these are deleterious effects that could cause device failure and delamination at the metal/ceramic interface.

Based on these data, it is reasonable to conclude that a thermal annealing treatment at 600°C for Ag-implanted AlN with a dose of 1 × 10^{16} cm^{-2} is inadequate to promote crystalline recovery of the AlN epilayer and diffusion-assisted precipitation of Ag in an AlN matrix. Since the melting temperature of AlN is in excess of 2000°C, it is essential that thermal annealing treatments be performed at temperatures approaching 1000°C. In this study, a thermal annealing treatment at 800°C was performed for 1 to 10 hours on samples implanted with a dose of 1 × 10^{16} cm^{-2}. No additional information was revealed from the 1-hour sample and additional experiments must be conducted for the other samples to draw concise conclusions from these annealing treatments.

To elucidate the origin of the "extra" reflections in the diffraction patterns, dark-field imaging was performed on the as-implanted samples (Figure 4.21). The reflections imaged in DF_1 – DF_4 are labeled in the SAD patterns (a) and (b). Although DF_1 and DF_2 are quite similar, DF_2 shows striking Moiré fringe contrast (encircled). These are rotational Moiré fringes coming from overlapping families of planes, generating the displaced diffraction spots labeled in the selected area diffraction patterns. There is also a reversal of contrast in the region indicated with the arrow. Distinct differences between DF_3 and DF_4 are difficult to discern because the image in DF_3 suffers from poor resolution. However, it is worth noting the alternating contrast (dark/bright regions) exhibited in all of the dark-field images (except for DF_3) which confirms the AlN columnar structure.

Transmission electron microscopy results reveal that some residual damage exists within the AlN epilayer even with post-thermal annealing treatments. Damage consistent with mottling is evident in all thermally annealed samples from Implantation 2 with some crystalline recovery observed in the samples thermally annealed up to a temperature of 600°C for 10 hours. Such damage is undetectable in the as-implanted samples, as well as those prepared from Implantation 1 (followed by a thermal annealing treatment at 550°C for 10 hours), thus revealing that a highly crystalline structure with little to no damage can be produced. The SAD patterns reveal that planar defects are non-uniformly present in the samples and are more dominant within the interior regions of the AlN matrix. Additionally, clusters of spherical Ag nanoprecipitates are identified throughout the matrix with average diameter sizes in the range of 40 – 90 nm. No preferential sites for Ag precipitation can be identified. Lastly no faceting can be detected in the nanoprecipitates thus providing an opportunity for facile diffusion, with the appropriate thermal activation energy.

5.6 Cross-Method Comparisons

The data presented in this manuscript disprove the original hypothesis that ion implantation of Ag in AlN at an energy of 100 keV to achieve a dose of 1×10^{16} ions/cm^2 followed by a thermal annealing treatment might be adequate to form a buried conductive layer. However, some helpful insights have been obtained. First, transmission electron microscopy confirms the depth of maximum Ag density to be approximately 45 nm from the AlN surface, consistent with TRIM and TRIDYN simulations conducted at 100 and 50 keV, respectively, as well as the RBS data. Additionally, electron microscopy analysis found no oxide phases to correlate with the oxygen signal in the RBS data, suggesting that oxygen ions must be incorporated in solid solution within the HCP AlN matrix, presumably to restore charge neutrality. High-resolution TEM with compositional analysis capabilities such as energy-dispersive spectrometry (EDS) would be needed to confirm the location of the oxygen within the AlN matrix.

Fine details indicative of structural damage is evident in the samples prepared from Implantation 2. The transition of this damaged/undamaged interface, with increases in temperature, is observed in TEM to indicate enhanced crystalline recovery with annealing. The sharper diffraction spots for samples annealed at 550 and 600°C indicate a larger grain size and strain-free thin film, consistent with the XRD and RBS results. It is however possible that, based on the minute changes in the FWHM values for thermally annealed samples (*via* Rocking Curve technique), enhanced crystalline quality is more localized. Additional TEM analyses of samples annealed at the same temperature and different times would be beneficial to assess the microstructural evolution of the AlN epilayer with respect to temperature and time. A more systematic approach to the thermal annealing treatment, with a broader range of temperatures and times, would provide additional insight into the crystalline quality and structural transformations induced in the AlN matrix.

Third, the orientation of the columnar morphology of the AlN matrix, as illustrated in the TEM image, corroborated well with the data obtained using XRD. With increases in annealing temperature, sharper rocking curves and decreases in the FWHM values were observed, which are indicative of larger grain sizes and lower defect concentrations. Similar observations are found in the TEM data (Figures 4.11, 4.12, 4.15 and 4.19), in which the width of the AlN columns increased with increasing annealing temperature. Based on these results, it can be concluded that the preferred orientation for multiple-reactive sputtered *c*-axis AlN on (001) Si substrates is (0002).

Finally, SEM and TEM imaging confirmed the presence of Ag within the AlN matrix. Chemical composition analysis performed using SEM with EDS capabilities (not shown here) validated the Gaussian profile of Ag as simulated *via* TRIM and TRIDYN and confirmed by RBS. The TEM data revealed the presence of spherical nanoparticles dispersed throughout the matrix; however, this observation was confirmed only in samples with a dose of 2.43×10^{16} Ag^{++}/cm^2. Thus, the implantation of Ag with a dose of 1.0×10^{16} Ag^{++}/cm^2 is inadequate to induce diffusion-assisted precipitation in AlN. As hypothesized, higher doses of Ag^{++} yield a higher concentration of Ag^{++} within the AlN matrix and thus provides a higher probability for the formation of a buried contact layer. Additionally, these results show that a critical concentration is necessary, *i.e., one* that lies between 1.0 × 10^{16} Ag^{++}/cm^2 and 2.68 × 10^{16} $Ag^{++}/cm^{2,}$ is necessary to induce the precipitation of Ag. If this higher concentration exceeds the solubility limits of Ag in AlN, the Ag will precipitate out of the matrix to form nanoprecipitates and, with sufficient thermal activation, a buried contact layer. It is highly probable that no evidence of Ag nanoprecipitates was found because the Ag atoms occupied the Al substitutional sites. Thus, based on these results a minimum concentration is essential to induce diffusion-assisted precipitation and thus a buried contact layer in AlN.

CHAPTER 6. CONCLUSIONS

Based on the research presented in this dissertation, the following conclusions can be drawn,

(1) Spherical Ag nanoprecipitates form, with average diameters in the range of 40 – 90 nm, in samples implanted with a dose of 2.68×10^{16} Ag^{++}/cm^2.

(2) Nanoprecipitate clusters are randomly dispersed throughout the matrix and not localized to preferential sites.

(3) No faceting is observed in the Ag precipitates within the AlN matrix; thus, they exhibit no preferred growth orientation.

(4) There is no evidence of Ag precipitates in samples implanted with a dose of 1×10^{16} $Ag^{++/}cm^2$ and post-thermally annealed at moderate temperatures.

(5) A critical concentration of Ag is essential to induce diffusion-assisted precipitation of nanoprecipitates and thus buried contact layers in ceramic materials.

(6) The primary objective was to assess the possibility of buried contact layers in the AlN system however under these conditions the data indicated that it could not be achieved. It is believed that under the appropriate conditions, higher Ag concentration and moderate thermal annealing temperatures, silver nanoprecipitates can form and coalesce to yield a buried contact layer.

(7) To develop a buried contact layer Ag concentrations exceeding 4 at. % are essential.

CHAPTER 7. FUTURE WORK

This work has demonstrated the feasibility of forming silver nanoprecipitates in aluminum nitride thin films for MEMS-based applications. Based on this work, there are various potential opportunities for further development and include the following:

(1) Determination of the implantation profile *via* TRIDYN at the actual ion implantation energy.

(2) Evaluation of film thickness of resultant conductive Ag film in aluminum nitride by annealing samples in a nitrogen-rich environment at temperature(s) above 962°C, the melting temperature of Ag, and subsequently quenching in LN_2.

(3) Determination of the orientation relationships of Ag nanoparticles that have coalesced after annealing at temperatures above 1000°C, the temperature at which the oxidation rate is accelerated. This would include samples implanted at room temperature and LN_2 conditions and quenched in water and LN_2.

(4) Comparative analysis of structural changes observed in samples that have been furnace and laser-thermal annealed.

(5) The experimental determination of the diffusivity of Ag in AlN at room temperature and elevated temperatures.

(6) Assessement of channeling effects in Ag-implanted AlN at low and high doses, in the range of $1 \times 10^{15} – 1 \times 10^{17}$ ions/cm^2, via RBS/channeling.

(7) Determination of depth profile, channeling effects and microstructural evolution of nanoprecipitates for Ag implanted in patterned AlN thin films grown on (100) silicon substrates.

REFERENCES

1. Ho, C., Itamura, M. T., Kelley, M. and Hughes, R. C., Review of chemical sensors for in-situ monitoring of volatile contaminants, Sandia National Laboratories, (2001).
2. Lewis, P. R. *et al.*, "Recent advancements in the gas-phase MicroChem Lab," *IEEE Sensors Journal* **6** (2006): 784–795.
3. Ho, C., Robinson, A., Miller, D. R. and Davis, M. J., "Overview of sensors and needs for environmental monitoring," *Sensors* **5** (2005): 4–37.
4. Sadik, O. A. and Mulchandani, A., "Chemical and biological sensors – Meeting the challenges of environmental monitoring," National Meeting of the American Chemical Society. Anaheim, CA, (1999).
5. Pfeifer, K. B., Hoyt, A. E., and Frye, G. C., *Acoustic-Wave Sensor for Ambient Monitoring of a Photoresist-Stripping Agent*. **5,795,993** (1998).
6. Andreescu, S. and Marty, J.-L., "Twenty years research in cholinesterase biosensors: From basic research to practical applications." *Biomolecular Engineering* **23** (2006): 1–15.
7. Sironi, S., Capelli, L., Centola, P., Del Rosso, R. and Grande, Il, M., "Continuous monitoring of odours from a composting plant using electronic noses," *Waste Management* **27** (2007): 389–397.
8. Murray, G. and Southard, G. E., "Sensors for chemical weapons detection," *IEEE Instrumentation and Measurement Magazine* **5** (2002): 12–21.
9. David, J., Simon, S., Zulfiqur, A. and William, O., "Chemical sensors for electronic nose systems,". *Mikrochimica acta* **149** (2005): 1–17 (2005).
10. Ponzoni, A. *et al.*, "Metal oxide nanowire and thin-film-based gas sensors for chemical warfare simulants detection," *IEEE Sensors Journal* **8** (2008): 735 – 742.
11. Janata, J., "Chemical sensors," *Analytical Chemistry* **64** (1992): 196-219.
12. Janata, J., "Potentiometric microsensors," *Chemical Reviews* **90** (1990): 691–703.
13. Hughes, R. C. *et al.*, "Integrated chemiresistor array for small sensor platforms," *Detection and Remediation Technologies for Mines and Minelike Targets V* **4038** (2000): 519-529.
14. Berger, T., Ziegler, H. and Krausa, M., "Development of electrochemical sensors for trace detection of explosives and for the detection of chemical warfare agents," *Detection and Remediation Technologies for Mines and Minelike Targets V* **4038** (2000) 452–461.
15. Ballantine, D. S. *et al.*, *Acoustic Wave Sensors: Theory, Design, and Physico-Chemical Applications*. San Diego: Academic Press (1997).
16. Portnoff, M. A., Grace, R. and Guzman, A. M., Measurement and analysis of adsistor and figaro gas sensors used for underground storage tank leak detection, United States Environmental Protection Agency (EPA), (1992).
17. Advanced Sciences, Inc., Chemometrics review for chemical sensor development, United States Department of Energy (DOE), (1994).
18. Wang, J., Ponton, C. B. and Marquis, P. M., "Silver-toughened alumina ceramics," *British ceramic transactions* **92** (1993): 67–74.

19. Chou, W. B. and Tuan, W. H., "Toughening and strengthening of alumina with silver inclusions," *Journal of the European Ceramic Society* **15** (1995): 291–295.
20. Backhaus-Ricoult, M., "A model of oxygen-activity-dependent adsorption (desorption) to metal–oxide interfaces," *Acta Materialia* **48** (2000): 4365–4374.
21. Ernst, F., Pirouz, P. and Heuer, A. H., "HRTEM study of a Cu/Al_2O_3 interface," *Philosophical Magazine A* **63** (1991): 259–277.
22. Backhaus-Ricoult, M., "Wetting anisotropy and oxygen activity dependency for oxides by liquid transition metals studied through shape changes of liquid Cu inclusions within MgO," *Acta Materialia* **49** (2001): 1747–1758.
23. Kondo, H. *et al.*, "Mechanical and magnetic properties of novel yttria-stabilized tetragonal zirconia/Ni nanocomposite prepared by the modified internal reduction method," *Journal of the American Ceramic Society* **88** (2005): 1468–1473.
24. Sugar, J. D., McKeown, J. T., Glaeser, A. M., Gronsky, R. and Radmilovic, V. "Spatially confined alloy single crystals for model studies of volumetrically constrained phase transformations," *Applied Physics Letters* **89** (2006): 173102–1–3.
25. Tran, H. T., Thermodynamic and Kinetic Observations of Embedded Metal Arrays in Sapphire. Master Thesis (M.S.), University of California, Berkeley (2004).
26. Wang, C. M. *et al.*, "Precipitation of Au nanoclusters in $SrTiO_3$ by ion implantation," *Journal of Applied Physics* **95** (2004): 5060–5068.
27. Gibbons, J. F., "Ion implantation in semiconductors — Part II: Damage production and annealing," *Proceedings of the IEEE* **60** (1972): 1062–1096.
28. Bucsa, I. G., Cochrane, R. W. and Roorda, S., "Segregation and formation of MnP particles during rapid thermal annealing of Mn-implanted InP and GaP," *Journal of Applied Physics* **106** (2009): 1–5.
29. Nakajima, A., Futatsugi, T., Horiguchi, N. and Yokoyama, N., "Formation of Sn nanocrystals in thin SiO_2 film using low-energy ion implantation," *Applied Physics Letters* **71** (1997): 3652–3654.
30. Zhou, S. *et al.*, "Crystallographically oriented Co and Ni nanocrystals inside ZnO formed by ion implantation and postannealing," *Physical Review B* **77** (2008): 1–12.
31. Ronning, C., "Ion implantation into gallium nitride," *Physics Reports* **351** (2001): 349–385.
32. Lee, J. *et al.*, "Magnetic properties of Co- and Mn-implanted $BaTiO_3$, $SrTiO_3$ and $KTaO_3$," *Solid-State Electronics* **47** (2003): 2225–2230.
33. Shang, D., Saito, Y., Kittaka, R., Taniguchi, S. and Kitahara, A., "Optical properties of $LiNbO_3$ implanted with Ag ions," *Journal of Applied Physics* **80** (1996): 6651–6654.
34. Takahiro, K. *et al.*, "Crystal structure and optical absorption of Au implanted MgO, $SrTiO_3$ and $LiNbO_3$ crystals," *Nuclear Instruments and Methods in Physics Research Section B: Beam Interactions with Materials and Atoms* **152** (1999): 314–318.
35. Tan, H. H. *et al.*, "Damage to epitaxial GaN layers by silicon implantation," *Applied Physics Letters* **69** (1996): 2364-2366.
36. Santala, M. K. *et al.*, "Precipitate orientation relationships in Pt-implanted sapphire," *Scripta Materialia* **62** (2010): 187–190.

37. Santala, M., Radmilovic, V., Giulian, R. and Ridgway, M., "The orientation and morphology of platinum precipitates in sapphire," *Acta Materialia* **59** (2011): 4761–4774.
38. Yin, W. *et al.*, "Modulation of the magnetism in ion implanted Mn_xGe_{1-x} thin films by rapid thermal anneal," *Journal of Applied Physics* **108** (2010): 1–6.
39. Kucheyev, S. *et al.*, "Ion-beam-produced structural defects in ZnO," *Physical Review B* **67** (2003): 1–11.
40. Dhara, S., "Formation, dynamics, and characterization of nanostructures by ion beam irradiation," *Critical Reviews in Solid State and Materials Sciences* **32** (2007): 1–50.
41. Wu, H. W., Tsai, C. J. and Chen, L. J., "Room temperature ferromagnetism in Mn^+-implanted Si nanowires," *Applied Physics Letters* **90** (2007): 043121–1–3.
42. Venkataraj, S. *et al.*, "Structural and magnetic properties of Mn-ion implanted ZnO films," *Journal of Applied Physics* **102** (2007): 1–7.
43. Kucheyev, S., "Effect of ion species on implantation-produced disorder in GaN at liquid nitrogen temperature," *Nuclear Instruments and Methods in Physics Research Section B: Beam Interactions with Materials and Atoms* **190** (2002): 782–786.
44. Jiang, W., Bae, I.-T. and Weber, W. J., "Disordering and dopant behaviour in Au^+-ion-irradiated AlN," *Journal of Physics: Condensed Matter* **19** (2007): 1–10.
45. Rimini, E. *Ion Implantation: Basics to Device Fabrication*. Boston: Kluwer Academic Publishers (1995).
46. Ziegler, J. F., Biersack, J. P. and Littmark, U., *The Stopping and Range of Ions in Solids*. New York: Pergamon (1985).
47. Ziegler, J. F., Transport of Ions in Matter (TRIM), http://srim.org, 2003.
48. Eckstein, W. and Möller, W., *TRIDYN, Binary Collision Simulation of Atomic Collisions*. Max-Planck-Institut für Plasmaphysik (1988).
49. Möller, W. and Posselt, M., TRIDYN_HZDR. <http://www.hzdr.de/db/Cms?pOid=21578&pNid=0> (20110.
50. Kholkin, A., Jadidian, B. and Safari, A.,"Ceramics, Piezoelectric and Electrostrictive," *Encyclopedia of Smart Materials, 2 Volume Set* (Schwartz, M.). New York: John Wiley and Sons, Inc. (2002).
51. Jaffe, B., Cook, W. R., Jr and Jaffe, H., *Piezoelectric Ceramics*. London: Academic Press (1971).
52. Cady, W. G., *Piezoelectricity: An Introduction to the Theory and Applications of Electromechanical Phenomena in Crystals*. New York**:** Dover Publications (1964).
53. Lippmann, G., "Principe de la conservation de l'électricité, ou second principe de la théorie des phénomènes électriques," *Annales de chimie et de physique* **24** (1881): 145–177.
54. Enlund, J., Fabrication of Electroacoustic Devices for Integrated Applications. Doctoral Thesis (Ph.D.), Uppsala University (2009).
55. Kochervinskii, V. V., "Piezoelectricity in crystallizing ferroelectric polymers: Poly(vinylidene fluoride) and its copolymers (A review)," *Crystallography Reports* **48** (2003): 649–675.
56. Tadigadapa, S. and Mateti, K., "Piezoelectric MEMS sensors: state-of-the-art and

perspectives," *Measurement Science and Technology* **20** (2009): 092001-1-30.

57. Kasap, S. O., *Principles of Electrical Engineering Materials and Devices*. Boston: McGraw-Hill (2000).
58. Haertling, G. H., "Ferroelectric ceramics: history and technology," *Journal of the American Ceramic Society* **82** (1999): 797–818.
59. Morgan, D., "Progagation Effects and Materials," *Surface Acoustic Wave Filters: with Applications to Electronic Communications and Signal Processing*. Oxford: Academic Press (2007).
60. Sommer, R. and Engeler, P., "Pressure Sensors," *Sensor Technology Handbook* (Wilson, J. S.). Burlington: Elsevier (2005).
61. Jaffe, B., Roth, R. S. and Marzullo, S., "Piezoelectric properties of lead zirconate-lead titanate solid-solution ceramics," *Journal of Applied Physics* **25** (1954): 809–810.
62. Cross, E, "Lead-free at last," *Nature* **432** (2004): 24–25.
63. Iriarte, G. F., Rodriguez, J. G. and Calle, F., "Effect of substrate–target distance and sputtering pressure in the synthesis of AlN thin films," *Microsystem Technologies* **17** (2011): 381–386.
64. Akiyama, M. *et al.*, "Flexible piezoelectric pressure sensors using oriented aluminum nitride thin films prepared on polyethylene terephthalate films," *Journal of Applied Physics* **100** (2006): 114318-1-5.
65. Ambacher, O., "Growth and applications of group III-nitrides," *Journal of Physics D: Applied Physics* **31** (1999): 2653–2710.
66. Gad-el-Hak, M., *MEMS: Introduction and Fundamentals*. Boca Raton: CRC Press (2010).
67. Li, T., "Challenge of III-V Materials Integration with Si Microelectronics," *III-V Semiconductors: Integration with Silicon-Based Microelectronics* (Li, T., Mastro, M. & Dadgar, A.). Boca Raton: CRC Press (2011).
68. Wang, X., Engel, J. and Liu, C., "Liquid crystal polymer (LCP) for MEMS: processes and applications," *Journal of Micromechanics and Microengineering* **13** (2003): 628–633.
69. Morgan, D., *Surface Acoustic Wave Filters: with Applications to Electronic Communications and Signal Processing*. Oxford: Academic Press (2007).
70. Kim, G.-B. *et al.*, "Development of biosensor using surface acoustic wave," *IECON 2004 – 30th Annual Conference of IEEE Industrial Electronics Society* **2** (2004): 1546–1549.
71. Gizeli, E. *et al.*, "Sensitivity of the acoustic waveguide biosensor to protein binding as a function of the waveguide properties," *Biosensors and Bioelectronics* **18** (2003): 1399–1406.
72. Datskos, P. *Electron/hole transport-based NEMS gyro and devices using the same*. **7,552,636** (2009).
73. Zhang, B. and Kahn, P. M., "Overview and improving fiber optic gyroscope based on MEMS/NEMS fabrication," *Journal of Physics: Conference Series* **34** (2006): 148–154.
74. Leondes, C. T., *MEMS/NEMS Handbook Techniques and Applications*. New York: Springer Science+Business Media (2006).

75. Janata, J., "Chemical sensors," *Analytical Chemistry* **64** (1992): 196–219.
76. Zhang, X., Wang, F.-Y. and Li, L., "Optimal selection of piezoelectric substrates and crystal cuts for SAW-based pressure and temperature sensors," *IEEE Transactions on Ultrasonics, Ferroelectrics, and Frequency Control* **54** (2007): 1207–1216.
77. Beeby, S. P., Tudor, M. J. and White, N. M., "Energy harvesting vibration sources for microsystems applications," *Measurement Science and Technology* **17** (2006): R175–R195.
78. Choi, W. J., Jeon, Y., Jeong, J. H., Sood, R. and Kim, S. G., "Energy harvesting MEMS device based on thin film piezoelectric cantilevers," *Journal of Electroceramics* **17** (2006): 543–548.
79. Cicco, G. D., Morten, B. and Prudenziati, M., "Elastic surface wave devices based on piezoelectric thin films," *IEEE Transactions on Ultrasonics, Ferroelectrics and Frequency Control* **43** (1996): 73–77.
80. Setter, N. *et al.*, "Ferroelectric thin films: Review of materials, properties, and applications," *Journal of Applied Physics* **100** (2006): 1–46.
81. Morgan, D., "Basic Survey," *Surface Acoustic Wave Filters: with Applications to Electronic Communications and Signal Processing*. Oxford: Academic Press (2007).
82. Brocato, R. W., A Zero-Power Radio Receiver, Sandia National Laboratories, (2004).
83. Brocato, R. W., Passive Microwave Tags, Sandia National Laboratories, (2004).
84. Brocato, R. W., Programmable SAW Development, Sandia National Laboratories, (2004).
85. Taylor, R. F. and Schultz, J., *Handbook of Chemical and Biological Sensors*. Bristol: Taylor and Francis (1996).
86. Tang, I. T. *et al.*, "Investigation of piezoelectric ZnO film deposited on diamond like carbon coated onto Si substrate under different sputtering conditions," *Journal of Crystal Growth* **252** (2003): 190–198.
87. Hassani, F. *et al.*, "ZnO based SAW delay line: thin film characteristics and IDT fabrication," *Materials Research Society Symposium Proceedings* **785** (2003): 101–106.
88. Hsaio, Y.-J., Fang, T.-H., Chang, Y.-H., Chang, Y.-S. and Wu, S., "Surface acoustic wave characteristics and electromechanical coupling coefficient of lead zirconate titanate thin film," *Materials Letters* **60** (2006): 1140–1143.
89. Muth, D. G., "Sputtering multilayered conductor films," *Journal of Vacuum Science and Technology* **8** (1971): 99–102.
90. Emanetoglu, N. W. *et al.*, "Analysis of SAW properties of epitaxial ZnO films grown on R-Al_2O_3 substrates," *IEEE Transactions on Ultrasonics, Ferroelectrics, and Frequency Control* **48** (2001): 1389–1394.
91. Rufer, L. *et al.*, "SAW chemical sensors based on AlGaN/GaN piezoelectric material system: acoustic design and packaging considerations," International Symposium on Electronics Materials and Packaging. Tokyo, Japan, (2005): 204-208.
92. Wohltjen, H. & Dessy, R., "Surface acoustic-wave probe for chemical-analysis .1. Introduction and instrument description," *Analytical Chemistry* **51** (1979): 1458–1464.
93. Yoo, B. K., Park, Y. W., Kang, C. Y., Yoon, S. J. and Kim, J. S., "Surface acoustic wave sensors to detect volatile gases by measuring output phase shift," *Journal of*

Electroceramics **17** (2006): 1013–1017.

94. Cernosek, R. W., Bigbie, J. R., Anderson, M. T., Small, J. H. and Sawyer, P. S., "High-temperature hydrocarbon gas sensing with mesoporous SiO_2 thin films on TSM resonators," Technical Digest. Solid-State Sensor and Actuator Workshop. Cleveland, OH, (1998): 375–378.
95. Grate, J. W., "Acoustic wave microsensor arrays for vapor sensing. *Chemical Reviews* **100** (2000): 2627–2647.
96. Sorensen, B., "Perspective," *Renewable Energy: Its Physics, Engineering, Environmental Impacts, Economics & Planning* (Sorensen, B.). San Diego, Academic Press (2000).
97. Sorensen, B., "Individual Renewable Energy Sources," *Renewable Energy: Its Physics, Engineering, Environmental Impacts, Economics & Planning* (Sorensen, B.). San Diego, Academic Press (2000).
98. Ng, T. H. & Liao, W. H., "Sensitivity Analysis and Energy Harvesting for a Self-Powered Piezoelectric Sensor," *Journal of Intelligent Material Systems and Structures* **16** (2005): 785–797.
99. Ziaei-Moayyed, M., Habermehl, S. D., Branch, D. W., Clews, P. J. and Olsson, R. H., "Silicon carbide lateral overtone bulk acoustic resonator with ultrahigh quality factor," Proceedings of the IEEE International Conference on Micro-electro-mechanical systems (MEMS). Cancun, Mexico (2011): 788–792.
100. Lin, C.-M., Chen, Y.-Y., Felmetsger, V. V., Senesky, D. G. and Pisano, A. P., "AlN/3C-SiC composite plate enabling high-frequency and high-Q micromechanical resonators," *Advanced Materials* **24** (2012): 2722–2727.
101. Lin, C.-M. *et al.*, "AIN thin films grown on epitaxial 3C-SiC (100) for piezoelectric resonant devices," *Applied Physics Letters* **97** (2010): 141907–1–3.
102. Lin, C.-M. *et al.*, "Quality factor enhancement in lamb wave resonators utilizing AlN plates with convex edges," Transducers 2011 – 16th International Solid-State Sensors, Actuators and Microsystems Conference. Beijing, China, (2011): 1512–1515.
103. Lin, C. M., Lai, Y. J., Hsu, J. C., Chen, Y. Y. and Senesky, D. G., "High-Q aluminum nitride Lamb wave resonators with biconvex edges," *Applied Physics Letters* **99** (2011): 143501–1–3.
104. Abdolvand, R., Lavasani, H. M., Ho, G. K. and Ayazi, F., "Thin-film piezoelectric-on-silicon resonators for high-frequency reference oscillator applications," *IEEE Transactions on Ultrasonics, Ferroelectrics and Frequency Control* **55** (2008): 2596–2606.
105. Yen, T.-T. *et al.*, "Characterization of aluminum nitride lamb wave resonators operating at 600°C for harsh environment RF applications," Proceedings of the IEEE International Conference on Micro-electro-mechanical systems (MEMS). Hong Kong, China (2010): 731–734.
106. Rao, Y. L. and Zhang, G. G., "Enhancing the sensitivity of SAW sensors with nanostructures," *Current Nanoscience* **2** (2006): 311–318.
107. Kim, G.-B. *et al.*, "Basic study to develop biosensors using surface acoustic waves," *Japanes. Journal of Applied Physics* **44** (2005): 2868–2873.

108. Avramov, I. D., Rapp, M., Kurosawa, S., Krawczak, P. and Radeva, E. I., "Gas sensitivity comparison of polymer coated SAW and STW resonators operating at the same acoustic wave length," *IEEE Sensors Journal* **2** (2002): 150–159.

109. Lam, C. S. and Holt, D. E., "Comparison of temperature performance of SAW filters made on ST- and LST-cut quartz," *Ultrasonics Symposium Proceedings* **1** (1988): 273–278.

110. Anisimkin, V. I., Kotelyanskii, I. M., Saggio, G., Verardi, P. and Verona, E., "A study on elastic energy distribution in layered structures for application to surface acoustic wave devices, Proceedings of the IEEE Ultrasonics Symposium. New York, New York, (1994): 453–456 (1994).

111. Yi-Chu, H. and Ngoc-Bich, L., "Coupling coefficient determination based on simulation and experiment for ST-cut quartz SAW delay-line response," *Microsystem Technologies* **1** (2008): 615–622.

112. Sung, C. C. and Huang, C. Y., "Properties of pseudomode surface acoustic waves on ST-cut quartz substrates and the effects of the thicknesses of metallic films," *Acoustical Physics* **52** (2006): 338–343.

113. Hsu, Y.-C., Le, N.-B. and Jang, L.-S., "Coupling coefficient determination based on simulation and experiment for ST-cut quartz saw delay-line response," *Proceedings of SPIE* **6589** (2007): 65891Q-1-11.

114. Belser, R. B. and Hicklin, W. H., "Comparison of aging performance of 5 MHz resonators plated with various electrode metals," Proceedings of the 23rd Annual Frequency Control Symposium. Washington, DC, (1999): 132–142.

115. Clarke, D. R. and Wolf, D., "Grain boundaries in ceramics and at ceramic-metal interfaces," *Materials Science And Engineering B: Solid State Materials For Advanced Technology* **83**, (1986): 197–204.

116. Dalgleish, B. J., Lu, M. C. and Evans, A. G., "The strength of ceramics bonded with metals," *Acta Metallurgica* **36** (1988): 2029–2035.

117. Hendrickson, M., Laffey, S. and Vig, J. R., "Investigations of gold films on quartz crystals," Proceedings of the IEEE International Frequency Control Symposium. Salt Lake City, Utah, (1993): 574–581.

118. Mattox, D. M., "Thin film metallization of oxides in microelectronics," *Thin Solid Films* **18** (1973): 173–186.

119. Shimizu, K., Kobayashi, K., Thompson, G. E. and Wood, G. C, "High resolution cross-sectional transmission electron microscopy of thermal oxide films on copper," *Corrosion Science* **36** (1994): 621–629.

120. Vig, J. R. and Meeker, T. R., "The aging of bulk acoustic wave resonators, filters and oscillators, Proceedings of the 45th Annual Symposium on Frequency Control. Los Angeles, California, (1991): 77–101.

121. Ronning, C. *et al.*, "Ion implanted dopants in GaN and AlN: Lattice sites, annealing behavior, and defect recovery," *Journal of Applied Physics* **87** (2000): 2149–2157.

122. Lorenz, K. and Vianden, R., "Defect recovery in AlN and InN after heavy ion implantation," *physica status solidi (c)* **0** (2002): 413–416.

123. Chernow, F., Borders, J. A., and Brice, D. K., *Ion Implantation in Semiconductors*. New

York: Plenum Press, (1976).

124. Williams, J., “Ion implantation of semiconductors,” *Materials Science & Engineering A* **253** (1998): 8–15.

125. Chappert, C. *et al.*, “Planar patterned magnetic media obtained by ion irradiation,” *Science* **280** (1998): 1919–1922.

126. Bhansali, S., Sood, D. K. and Zmood, R. B., “Selective electroless copper plating on silicon seeded by copper-ion implantation,” *Thin Solid Films* **253** (1994): 391–394.

127. Borowski, M. and Traverse, A., “High fluence implantation of Cu, Fe and Ti in AlN: Depth profiling by RBS and RNRA,” *Nuclear Instruments and Methods in Physics Research Section B: Beam Interactions with Materials and Atoms* **114** (1996): 269–275.

128. Frazier, R. M. *et al.*, “Properties of Co-, Cr-, or Mn-implanted AlN,” *Journal of Applied Physics* **94** (2003): 1592–1596.

129. Han, S. Y. *et al.*, “Effect of Gd implantation on the structural and magnetic properties of GaN and AlN,” *Applied Physics Letters* **88** (2006): 1–3.

130. Magruder, R. H. *et al.*, “Optical properties of gold nanocluster composites formed by deep ion implantation in silica,” *Applied Physics Letters* **62** (1993): 1730–1732.

131. Strite, S. and Morkoc, H., “GaN, AlN, and InN: A review,” *Journal of Vacuum Science and Technology B* **10** (1992): 1237–1266.

132. Dong, H. and Bell, T., “State-of-the-art overview: ion beam surface modification of polymers towards improving tribological properties,” *Surface and Coatings Technology* **111** (1999): 29–40.

133. Fassbender, J. and McCord, J., “Magnetic patterning by means of ion irradiation and implantation,” *Journal of Magnetism and Magnetic Materials* **320** (2008): 579–596.

134. Zhu, S., Wang, L. and Zu, X., “Optical and magnetic properties of Ni nanoparticles in rutile formed by Ni ion implantation,” *Applied Physics Letters* **88** (2006): 1–3.

135. Zhou, S. *et al.*, “Crystalline Ni nanoparticles as the origin of ferromagnetism in Ni implanted ZnO crystals,” *Journal of Applied Physics* **100** (2006): 114304-1-4..

136. Scarpulla, M. *et al.*, “Diluted magnetic semiconductors formed by ion implantation and pulsed-laser melting,” *Physica B: Condensed Matter* **340** (2003): 908–912.

137. Dasgupta, V., Litombe, N., Bailey, W. E. and Bakhru, H., “Ion implantation of rare-earth dopants in ferromagnetic thin films,” *Journal of Applied Physics* **99** (2006): 1–3.

138. Dolph, M. C. *et al.*, “Magnetic properties of ion implanted $Ge_{1-x}Mn_x$ thin films solidified through pulsed laser melting,” *Journal of Applied Physics* **109** (2011): 1–6.

139. Hullavarad, S. S. *et al.*, “Advances in pulsed-laser-deposited AIN thin films for high-temperature capping, device passivation, and piezoelectric-based RF MEMS/NEMS resonator applications,” *Journal of Electronic Materials* **35** (2006): 777–794.

140. Chattopadhyay, S., Ganguly, A., Chen, K.-H. and Chen, L.-C., “One-dimensional group III-nitrides: growth, properties, and applications in nanosensing and nano-optoelectronics,” *Critical Reviews in Solid State and Materials Sciences* **34** (2009): 224–279.

141. Henderson, D. *et al.*, “Optical response from the ultraviolet to the far infrared and atomic force microscopy of Au implanted in CaF_2,” *Journal of Vacuum Science and Technology A* **14** (1996): 1199–1204.

142. Ueda, A. *et al.*, "Interaction of F_n-centers with gold nanocrystals produced by gold ion implantation in MgO single crystals," *Nuclear Instruments and Methods in Physics Research Section B: Beam Interactions with Materials and Atoms* **141** (1998): 261–267.

143. Yang, G., Wang, W., Yang, C. and Chen, Z., "Enhanced nonlinear optical properties of laser deposited Ag/$BaTiO_3$ nanocomposite films," *Chinese Physics Letters* **20** (2003): 924–927.

144. Sun, K., Zhu, S., Fromknecht, R., Linker, G. and Wang, L., "Formation of single-layered Au nanoparticles in Au ion implanted TiO_2 and $SrTiO_3$," *Materials Letters* **58** (2004): 547–550.

145. Li, M. *et al.*, "Optical and magnetic measurements of Mn^+-implanted AlN," *Journal of Applied Physics* **95** (2004): 755–757.

146. Lorenz, K. *et al.*, "Optical doping of AlN by rare earth implantation," *Nuclear Instruments and Methods in Physics Research Section B: Beam Interactions with Materials and Atoms* **242** (2006): 307–310.

147. Traverse, A., Parent, P., Mimault, J., Hagege, S. and Du, J., "Copper clusters made by implantation in aluminum nitride," *Nuclear Instruments and Methods in Physics Research Section B: Beam Interactions with Materials and Atoms* **84** (1994): 204–207.

148. Kucheyev, S., Williams, J. and Zou, J., "Ion-beam-produced damage and its stability in AlN films," *Journal of Applied Physics* **92** (2002): 3554–3558.

149. Borowski, M., Traverse, A. and Eymery, J., "Phase formation after high fluence implantation of Fe in AlN: A Mossbauer study," *Nuclear Instruments and Methods in Physics Research Section B: Beam Interactions with Materials and Atoms* **122** (1997): 247–252.

150. Singh, R., Scholz, R., Christiansen, S. H. and Goesele, U., "Formation of nanovoids/microcracks in high dose hydrogen implanted AlN," *physica status solidi (a)* **205** (2008): 2683–2686.

151. Yamada, M. and Iwaki, M., "Surface-layer oxidation of copper-implanted aluminum nitride," *Journal of Materials Science Letters* **7** (1988): 1233–1234.

152. Lee, J. W., Radu, I. and Alexe, M., "Oxidation behavior of AlN substrate at low temperature," *Journal of Materials Science: Materials in Electronics* **13**, (2002): 131–137.

153. Lide, D. R. *CRC Handbook of Chemistry and Physics.* Boca Raton, CRC Press (2008).

154. Du, X., Design and Fabrication of a Prototype Aluminum Nitride-Based Pressure. Doctoral Thesis (Ph.D.), Wayne State University (2012).

155. Attaran, M. M., Erfanian, A. and Kian, P. G., "Production of NANO powder of aluminum nitride by pulsed power method," Proceedings of the 7th WSEAS Conference. Hangzhou, China, (2008): 75–77.

156. Vollstädt, H., Ito, E., Akaishi, M., Akimoto, S.-I. and Fukunaga, O., "High pressure synthesis of rocksalt type of AlN," *Proceedings of the Japan Academy Series B: Physical and Biological Sciences* **66** (1990): 7–9.

157. Van Camp P. E., Van Doren V. E. and Devreese, J., "High-pressure properties of wurtzite- and rocksalt-type aluminum nitride," *Physical Review B: Condensed Matter* **44** (1991): 9056–9059.

158. Srivastava, A. and Tyagi, N., "Pressure induced zinc-blende to rocksalt phase transition in AlN nanocrystal," *Journal of Physics: Conference Series* **377** (2012): 012066-1-5.

159. Levinshtein, M. E., Rumyantsev, S. L., and Shur, M. S. *Properties of Advanced Semiconductor Materials: GaN, AlN, InN, BN, SiC, SiGe*. New York: John Wiley and Sons, Inc. (2001).

160. Pierson, H. O. *Handbook of Refractory Carbides and Nitrides: Properties, Characteristics, Processing, and Applications*. Westwood: Noyes Publications, (1996).

161. Singh, A. V., Chandra, S. and Bose, G., "Deposition and characterization of *c*-axis oriented aluminum nitride films by radio frequency magnetron sputtering without external substrate heating," *Thin Solid Films* **519** (2011): 5846–5853.

162. Mortet, V. *et al.*, "Structural characterisations of AlN/diamond structures used for surface acoustic wave device applications," *Physica Status Solidi A*, **199** (2003): 145–150.

163. Blauert, J. and Xiang, N., *Acoustics for Engineers*. Berlin: Springer, (2009).

164. Lakin, K. M., Belsick, J., McDonald, J. F. and McCarron, K. T., "Improved bulk wave resonator coupling coefficient for wide bandwidth filters," *IEEE Ultrasonics Symposium* **1** (2001): 827–831.

165. Mishin, S. and Oshmyansky, Y., "Thin films deposition for BAW devices," *RF Bulk Acoustic Wave Filters for Communications* (Hashimoto, K.-Y.). Boston: Artech House Publishers (2009).

166. Tsubouchi, K., Sugai, K. and Mikoshiba, N., "AlN material constants evaluation and SAW properties on AlN/Al_2O_3 and AlN/Si., Ultrasonics Symposium Proceedings. New York, New York, (1981): 375–380.

167. Wong, B. P. *et al.*, *Nano-CMOS Design for Manufacturability*. Hoboken, John Wiley and Sons, Inc., (2009).

168. Morkoc, H., Özgür, Ü. and Morko, H., *Zinc Oxide: Fundamentals, Materials and Device Technology*. Weinham: Wiley-VCH (2009).

169. Eccleston, C., March, F. and Cohen, T., "Perspectives on energy efficiency and conservation," *Inside Energy: Developing and Managing an ISO 50001 Energy Management System*. Boca Raton: CRC Press, Taylor and Francis, LLC (2012).

170. Ayers, J., "Properties of Semiconductors," *Heteroepitaxy of Semiconductors: Theory, Growth, and Characterization*. Boca Raton: CRC Press, Taylor and Francis, LLC (2009).

171. Hillert, M. and Jonsson, S. *Al-N Phase Diagram*. Materials Park: Ohio: ASM International (2006).

172. Hillert, M. & Jonsson, S. *Al-N-O Phase Diagram*. Materials Park: Ohio: ASM International (2006).

173. Karakaya, I. & Thompson, W. T. *Ag-O Phase Diagram*. Materials Park: Ohio: ASM International (2006).

174. Taylor, J. R., Hillert, M. and Selleby, M. *Ag-Al Phase Diagram*. Materials Park: Ohio: ASM International (1987).

175. Yushkov, G. Y., Anders, A., Oks, E. M. and Brown, I. G., "Ion velocities in vacuum arc plasmas," *Journal of Applied Physics* **88** (2000): 5618–5622.

176. Mayer, M. *SIMNRA6.0*. <http://home.rzg.mpg.de/~mam/> (2011).

177. Mayer, M. *SIMNRA User's Guide*. , Max-Planck-Institut für Plasmaphysik, Garching, Germany (1997).

178. Bravman, J. C. and Sinclair, R., "The preparation of cross-section specimens for transmission electron microscopy," *Journal of Electron Microscopy Technique*, **1** (1984)53–61.

179. National Institute of Health (NIH), *Image J,* <rsweb.nih.gov>.

180. Möller, W. & Eckstein, W., "Tridyn — A TRIM simulation code including dynamic composition changes," *Nuclear Instruments and Methods in Physics Research Section B: Beam Interactions with Materials and Atoms* **2** (1984): 814–818.

181. Möller, W., Eckstein, W. & Biersack, J. P., "TRIDYN-binary collision simulation of atomic collisions and dynamic composition changes in solids," *Computer Physics Communications* **51** (1988): 355–368.

182. Hillert, M. & Jonsson, S. *Al-O Phase Diagram*. Materials Park: Ohio: ASM International (1992).

183. Porter, D. A. and Easterling, K. E., *Phase Transformations in Metals and Alloys*. London: Chapman and Hall (1992).

184. Callister, Jr., W. C., *Materials Science and Engineering: An Introduction*. New York: John Wiley and Sons (2003).

185. International Centre for Diffraction (ICDD) Data, <www.icdd.com/> (2011).

186. Ohuchi, F.S. and Russell, P.E., "AlN thin films with controlled crystallographic orientations and their microstructure," *Journal of Vacuum Science and Technology A* **5** (1987): 1630-1634.

187. Smith, D. L., *Thin Film Deposition: Principles and Practice*. Boston: McGraw Hill (1995).

188. Rossnagel, S., *Handbook of Thin Film Deposition Processes and Techniques, 2nd Edition* (Krisna Seshan). *Norwich:William Andrew Publishing/Noyes* (2001).

189. Townsend, P. D. Kelly, J. C. and Hartley, N. E. W., *Ion Implantation, Sputtering and their Applications*. New York, Academic Press (1976).

190. Rutherford, E. *Phil. Mag.* **21** 669 (1911): 669-688.

191. Geiger, H. and Marsden, E., *Phil. Mag.* **25** (1913) 606.

192. *Yu, Kin-Man*, Heavy ion Rutherford backscattering spectrometry (HIRBS) for near surface characterization of electronic materials. Master Thesis (M. S.), University of California, Berkeley (1984).

193. Cullity, B. D., *Elements of x-ray diffraction*. Reading: Addison-Wesley Publishing Co. (1978).

194. Goldstein, J., *et al.*, "The SEM and Its Modes of Operation," in *Scanning Electron Microscopy and X-Ray Microanalysis*. New York: Kluwer Academic (2003).

195. Goldstein, J., *et al.*, "*Introduction*," in *Scanning Electron Microscopy and X-Ray Microanalysis*. New York: Kluwer Academic (2003).

196. Joy, D. C., "Scanning Electron Microscopy for Materials Characterization," *Current Opinion in Solid State & Materials Science* **2** (1997): 465-468.

197. Bradke, M. von, Gitzhofer, F. and Henne, R.. "Porosity Determination of Ceramic

Materials by Digital Image Analysis - A Critical Evaluation," *Scanning* **27** (2005)**:** 132-135.

198. McDonald, Kent, Electron Microscope Lab, Available at <http://biology.berkeley.edu/EML/equipment.html>.

199. Dykstra, M. J. and Reuss, L. E., "Transmission Electron Microscopy," in *Biological Electron Microscopy: Theory, Techniques, and Troubleshooting*. New York: Kluwer Academic (2003).

APPENDIX: BACKGROUND ON TECHNIQUES

Sputtering

Sputtering is a physical vapor deposition method that consists of bombarding a target with energetic particles to eject these "target" atoms in a projectile motion toward the substrate to form a thin film. The momentum exchange that occurs as a result of this ion-atom interaction is the driving force for this process.

To accomplish this exchange, energetic particles are introduced into the vacuum chamber *via* an ion source, plasma, or an accelerator. These "ionized particles" are directed toward the target (*via* magnets), causing an ion-atom interaction that results in the ejection of "target" atoms. The number of atoms ejected from the target is dependent on the type of target atom, energy of the ion, mass of the ion, ion incident angle, and the binding energy of the ion and target. This number, per incident ion, is referred to as the sputter yield.

Once ejected, these "target" atoms are deposited on the substrate. The composition of the deposited film may be analogous to the target or react with other elements in the chamber to form a multi-component film. The entire process is conducted under high vacuum conditions to increase the ratio of mean free path to the target with respect to the substrate distance. The quality of the resulting film is dependent on the type of method employed, *e.g.*, direct current (dc), alternating current (ac), radiofrequency (rf), magnetron, reactive, ion-beam, and hybrid (combination of two or more of the previously mentioned techniques) sputtering.[187,188] The quality of the film is one determinate; however, other parameters play a vital role in the method of choice, including film composition and pre-cursor or target material available. For the purpose of this dissertation work, reactive magnetron sputtering was the preferred method for deposition.

Ion Implantation

Ion implantation is a method commonly utilized in the semiconductor industry to modify the chemical, electrical or physical properties near the surface of materials. It provides excellent control of the number and distribution of atoms that can be injected, localized doping, and the ability to implant single isotopes in shorter times.[189] Additionally, the process is conducted under non-thermodynamic conditions and thus enables ion injection at levels exceeding the solubility limits, which is a limitation of conventional treatments. Thus, this method has been widely implemented in the silicon industry to dope Si to enhance the performance for applications such as p-n junctions, integrated circuits, rectifiers, *etc.* More recently, ion implantation has been implemented in a host of materials including III-V materials, metals, alloys and polymers.

During ion implantation, several processes occur, including ion bombardment, displacement, and sputtering. Ions, which have energies in the keV - MeV range, undergo a series of energy-loss collisions with both target atoms and electrons, processes commonly referred to in the literature as nuclear and electronic collisions, respectively. Eventually, all of the ions come to rest hundreds of atomic layers below the surface; however, not all atoms reside at the same depth. Therefore, an ion distribution with an approximate Gaussian curve results, with the peak of the curve representing the projected ion range, R_p. As the dose of incident ions is increased, the concentration of implanted atoms also increases, resulting in near-surface modifications in the material (and higher probabilities of amorphization).

Collision cascades in the target cause lattice atom displacements (tens of hundreds of lattice atoms), which generate defects and, sometimes, an amorphous (disordered) structure. To recover such damage, annealing must often be employed. Simultaneously, incident ions can sputter away one or more lattice atoms, such that prolonged exposure to irradiation can yield surface erosion and the removal of already-implanted atoms. Computer simulation models, such as TRIM and TRIDYN, have been developed and implemented to quantify the expected number and distribution of such displaced atoms. Based on the results thus far, the structural damage that results from ion bombardment is significantly more complex and both models have limited applications.

Transport of Ions in Matter (TRIM)

Transport of Ions in Matter (TRIM) is one of the most comprehensive programs of Stopping and Range of Ions in Matter (SRIM). SRIM is a group of programs that can be used to calculate the stopping and range of ions into matter based on the quantum mechanics of ion-atom collisions.[46] It employs the Monte Carlo Binary Collision Approximation (BCA) simulation program, which is based on a two-component target system. Statistical algorithms are incorporated to account for ion jumps between calculated collisions, and then an average of the results is performed. Both long-range and short-range interactions are accounted for in the computation. It is useful in such applications as ion implantation, sputtering, ion transmission and ion beam therapy.[46]

In particular, TRIM provides information on multi-layered complex targets, with a layer limit of 8. The data attainable through TRIM include ion energy losses, such as target damage, sputtering, ionization, and phonon production, as well as a 3D ion distribution.[46] Previously, the disadvantage to SRIM/TRIM was its limitation to single energy sources, because calculations in the program are made with respect to the ion effective charge state. Additionally, variations in target composition are ignored. More recent models, such as SRIM 2010 and later, address this by the addition of a PAUSE feature that allows one to modify the parameters and resume modeling. This requires the user to predict how the target is modified during the implantation process. Therefore, reliable results are limited to low implantation fluences. Because the current investigation is interested in the ion implantation of a multi-component system at high implantation energies, it was essential to consider an alternative method that can account for modifications in the material during implantation.

TRIDYN

TRIDYN is a computer simulation program developed by Möller and Eckstein using the same Binary Collision Approximation model as TRIM developers.[180] The main distinction between

TRIM and TRIDYN is that TRIDYN simulates the dynamic change of composition and thickness of multi-component targets during ion implantation. TRIDYN can also be extended to a five-component system. The additional benefit is the analysis of homogeneous, inhomogeneous, and layered targets,[180] while inhomogeneous targets are inaccessible with TRIM. In contrast to TRIM, variations in the beam energy and angles of incidence can also be considered. As a result, TRIDYN has been employed in high fluence ion implantation applications, with the exception of energies above the MeV range, because TRIDYN does not contain a collision frequency reduction, such as that in TRIM.[180] Additional information on TRIDYN can be obtained in the publications of Möller and Eckstein.[181]

The results acquired from TRIM and TRIDYN simulations were compared with respect to the experimental results acquired *via* rutherford backscatter spectroscopy (RBS) and transmission electron microscopy.

Rutherford Backscattering Spectrometry (RBS)

Rutherford Backscattering Spectrometry (RBS) is a non-destructive surface characterization technique with depth profiles of 100 to 1000 Å. This technique was developed based on the investigations conducted by Hans Geiger and Ernest Marsden, under the supervision of Lord Ernest Rutherford, and thus the name. The original experimental design consisted of the acceleration of energetically charged alpha particles in the direction of a group of atoms and the analysis of the angle distribution of the particles after passing through the atoms.[190,191] As a result of these investigations, RBS has been considered an attractive method in the field of materials science because it provides structural and compositional information, such as the identification of elemental constituents, concentration profiles, and the depth and thickness of impurity layers.

The RBS experiment consists of three essential components, including an ion source, scattering chamber and detector. A collimated monoenergetic beam of charged particles is generated from the ion source and directed on a target. Alpha particles are then backscattered, with respect to the incident beam, by the atomic nuclei. A detector then collects the backscattered particles, and their respective energies are evaluated. The energies of these backscattered particles are the essence of RBS.[190,192] These energies are dependent on the identity of the atom from which the particle travels before scattering, the scattering angle, and the distance over which the particle traveled before scattering. Thus, RBS is a useful technique for acquiring the compositional and structural information of materials. Additional information on RBS can be obtained in the literature.[190,192]

X-Ray Diffraction (XRD)

X-ray diffraction (XRD) is a non-destructive characterization technique employed to determine crystal structure, chemical composition, stress values, particle size, and crystal(s) orientation. The fundamental principles of XRD are based on the 1912 investigations of Max von Laue in which he discovered that crystals diffract x-rays and the manner of the diffraction is based on crystal structure.[193]

X-rays are a type of electromagnetic radiation with wavelength values within the 0.5 – 2.5 Å regime. They are produced when electrons of sufficient energy are decelerated. In XRD, this is accomplished in a cathode tube, which consists of an electron source (typically tungsten filament) and two metal electrodes (cathode (negatively charged) and anode (positively charged)). The high voltage generated across the electrodes draws the electrons to the anode where they strike the target at a high velocity to generate X-rays, which then radiate in all directions (thus, a range of wavelengths is produced, yielding heterochromatic radiation conditions). The radiation is then filtered to produce monochromatic radiation and is directed toward the specimen stage where it is then diffracted by the specimen to form a convergent diffracted beam. It is important to note here that the interaction of the incident rays with crystals produces diffraction (and constructive interference) when the conditions of Bragg's Law are satisfied, $n\lambda = 2d\sin\theta_B$ (n = path difference in whole numbers, λ = wavelength, d= lattice spacing of crystal, and θ_B = angle between incident beam and diffracted beam where Bragg conditions are met). Scanning the sample through a range of 2θ values allows for the determination of all possible diffraction directions of the lattice. The diffracted beam is then passed through a filter to suppress background radiation originating from the specimen. The X-rays produced are then detected and converted into a pulsating electric current by the counter and output to a device (*e.g.*, monitor) to generate the XRD pattern shown in § 4.1. Additional information on Bragg's Law and diffraction can be found in Cullity.[193]

This technique has been widely used to study a myriad of materials, including metals, semiconductors, ceramics and polymers. However, it has limited application in the detection of elements (alloys, compounds) present in trace amounts and small crystalline structures. Thus this method is typically used to measure materials with large crystalline structures.

Rocking Curve

Rocking curve is a technique analogous to XRD but with a slight variation. In XRD, the counter is rotated about the diffractometer axis. Because the carriage supporting the counter and the specimen stage is mechanically coupled, a rotation of the counter through 2× degrees yields a rotation of the specimen stage (and thus, the specimen) through x degrees. This arrangement is necessary to ensure the angles incident on the specimen are always equal to and half the angle of diffraction (2θ). However, the experimental design for rocking curve measurements consists of rocking the specimen through the Bragg angle, θ_B, at a fixed 2θ (accomplished with a stationary counter). The width of the curve is inversely proportional to the defect density and thus provides information on the degree of crystal orientation. The resulting curve is intensity I *vs.* θ, as exhibited in §4.

Scanning Electron Microscopy

Scanning electron microscopy is a tool employed to characterize various materials on the nanometer to micrometer scale. In the scanning electron microscope (SEM), an electron beam source is heated such that a fine beam of electrons is produced. Accelerating voltages as high as 30kV can be reached.[194] Electromagnetic lenses focus the fine beam into a small spot on the sample's surface. The beam is rastered across the surface to produce backscattered and secondary electrons and characteristic x-rays. The electrons accumulate on the collector to produce an image, which can be viewed by the user on the viewing screen. The information provided by the image includes crystal orientation, topography, composition, magnetic field, and electrical field.[195,196] Some have even used SEM micrographs to measure porosity.[197]

The main advantage in utilizing an SEM is that it allows imaging of bulky or thin samples, has a high depth of field, and produces high-resolution three-dimensional images. For conventional SEMs, a lateral resolution of 10-50 nm and a depth resolution of 1-1000 nm can be attained, where the latter is contingent on the signal detected.[195] Additionally, most SEMs can reach magnifications of 10 to 800,000×.[195,198]

Transmission Electron Microscopy

Transmission electron microscopy is an imaging characterization technique used to obtain crystallographic and morphological information for various materials, including ceramics, metals, and polymers. This information is acquired with the use of an electron source, vacuum chamber, various lenses, and a fluorescent screen. The fundamental components of a transmission electron microscope (TEM) are the electron source and lenses. The beam of electrons "passes through" the specimen; therefore, the technique was given the name transmission electron microscopy.

In TEM, a stream of high-energy electrons is produced by an electron source. The electrons are then directed toward the sample in a high vacuum environment. As the electrons descend the column, electromagnetic lenses focus the electrons to a fine beam for illumination. Electrons strike the thin sample, at which point electron-sample interaction occurs. The image produced is then focused and magnified by the objective lens. The image descends the remainder of the TEM column, through the intermediate and projector lenses, where it is magnified. The image strikes the fluorescent screen yielding an image that is visible to the user.[199]

The key attributes of using TEM are that it operates at high accelerating voltages, ranging from 100-120 kV, and provides high-resolution, high-magnification images. Its resolution capabilities of 0.2 nm far exceed the characteristics of optical microscopes.[13] Most TEMs can reach magnifications exceeding 200,000×[199] where the average optical microscope provides a maximum of 2,500× magnification. While it is advantageous to use TEM, sample preparation to obtain extremely thin samples and potential beam damage, limit its use.